Ražnjević

High-resolution modelling of plume dispersion

High-resolution modelling of plume dispersion

Anja Ražnjević

Propositions

1. Plume measurements done with the goal of estimating source strength are useless if the wind data is not measured simultaneously.
   (this thesis)

2. Direct Numerical Simulation is more accurate than Large Eddy Simulation for simulating close-source plume dispersion.
   (this thesis)

3. To promote acceptance of peer reviews, the implementation of a compensation mechanism for reviewers is essential.

4. Large offices, despite individuals' efforts to be considerate of their colleagues, can unavoidably introduce distractions that impede students' ability to concentrate and focus effectively.

5. Procrastination increases efficiency.

6. Excessive activism is as harmful to a specific societal issue as inaction.

7. Educational institutions should focus on the development of skills that complement the use of Artificial Intelligence.

Propositions belonging to the thesis, entitled
High-resolution modelling of plume dispersion
Anja Ražnjević
Wageningen, 1. 9. 2023.

High-resolution modelling of plume dispersion

Anja Ražnjević

Thesis committee

Promotor:
Prof. Dr M. Krol
Professor of Air Quality and Atmospheric Chemistry
Wageningen University & Research

Co-promotors:
Dr C. C. van Heerwaarden
Assistant Professor, Meteorology and Air Quality
Wageningen University & Research

Other members:
Prof. Dr T. Hoitink, Wageningen University & Research, The Netherlands
Prof. Dr T. Röckmann, Utrecht University
Dr I. Pison, Laboratoire des Sciences du Climat et de l'Environnement, France
Dr M. Cassiani, Norsk Institutt for luftforskning, Norway

This research was conducted under the auspices of the Graduate School
for Socio-Economic and Natural Sciences of the Environment (SENSE)

High-resolution modelling of plume dispersion

Anja Ražnjević

Thesis
submitted in fulfilment of the requirements for the degree of doctor at
Wageningen University
by the authority of the Rector Magnificus
Prof. Dr A.P.J. Mol,
in the presence of the
Thesis Committee appointed by the Academic Board
to be defended in public
On Friday 1 September 2023
at 4 p.m. in the Omnia Auditorium.

Anja Ražnjević
High-resolution modelling of plume dispersion,
164 pages.

PhD thesis, Wageningen University, Wageningen, NL (2023)
With references, with summary in English

DOI: https://doi.org/10.18174/634327
ISBN: 978-94-6447-787-0

Summary

Climate change is one of the most important societal issues the world is currently facing. Since the warming of the atmosphere is driven by human actions, namely the surplus of greenhouse gases (such as carbon dioxide, methane, nitrous oxide, etc.) being emitted into the atmosphere. Therefore, the need to reduce emissions as soon as possible and get them to zero net, or even negative, emissions in order to minimize the impact of climate change is unquestionable. Greenhouse gases vary in their warming effect on the atmosphere due to differences in their ability to retain long wave radiation as well as their residence times. Carbon dioxide is the most important greenhouse gas due to its abundance in the atmosphere and its long residence time (about 100 years) creates a large hysteresis between emission reduction and change in the warming effect it has on the atmosphere. Currently the second most important in the greenhouse gas ranking is methane with a warming potential 28 that of carbon dioxide on a 100 years time scale. As with any other greenhouse gas, the atmospheric concentration has been steadily rising in the past century and is now more than 2 times above the pre-industrial levels. Unlike carbon dioxide, methane has relatively short residence time of about 10 years and immediate emissions mitigating efforts will have a quicker atmospheric response. However, methane has a large variety of sources, both natural and anthropogenic, as it is a by-product of organic decomposition and it can be found in underground reserves in form of the natural gas. Due to their versatility, methane sources are not well constrained in the emission inventories.

To tackle this issue, the Methane goes Mobile – Measurements and Modelling (MEMO^2, `https://h2020-memo2.eu/`) project was started. The goal of the project was to use various mobile measurement approaches to quantify European methane emissions and, in combination with modelling across different spatial and temporal scales, to update the European emission inventories. However, the mobile measurement methods the project focused on (i.e. measurement instrument placed in cars or on unmanned areal vehicles) are most often performed on distances very close to the source. There, the methane plumes are subject to turbulent processes that govern the motions in the atmospheric boundary layer. Inherently, this means the measured plumes are extremely variable, which makes it difficult to measure them and to quantify the emission rates from those plume measurements. This is where the research presented in this thesis falls in the scope of the MEMO^2

project. The work presented in this thesis focuses on high-resolution modelling of plume dispersion in different atmospheric conditions and in rural and urban environments. The goal of this research is twofold: (1) to evaluate mobile measurement techniques using simulations that realistically represent atmospheric conditions and plumes on very short downwind distances from the sources, and (2) to evaluate the ability of high-resolution models to reproduce a realistic measurement day but also to benchmark different modelling techniques against each other.

Chapter 3 focuses on the first of the two goals of this thesis. In this chapter large-eddy simulations (LES) have been used to evaluate two widely-used observational techniques: the use of car measurements perpendicular to the mean wind and the Other Test Method 33A (OTM33A). The LES study simulates a plume emitted from a point source into a neutrally stratified atmosphere over a flat terrain. This flow was chosen to benchmark the two methods in controlled conditions where they are expected to perform well as the sources of errors are minimized. We released three plumes with different source heights into the flow which were then sampled mimicking the car transects and the stationary OTM33A method. We have found that in order for the car transect method to estimate the source strength with 40% accuracy of accuracy, at least 15 transects through the plume have to be taken and averaged. For OTM33A, which focuses on plume measurements up to 200 m downwind from the source, we have found that very close to the source (48 m) the plume is not yet dispersed enough to use the method as all the source strength estimations yield similar results. We have also found the method consistently overestimates the source strength. This is due to the too large dispersion coefficients proposed for the OTM33A method (at least compared to our dispersion simulation). Lastly, we have found that the position of the time-averaged plume centerline differs from the plume emission height due to wind shear effects. This can be an added source of error if a Gaussian plume model (GPM) is used to interpret the measurements.

To step away from very simple plume models (i.e. GPM) used to model plume dispersion, in chapter 4 we used LES to reproduce the meteorological conditions and a plume dispersing in the atmosphere encountered in an actual field campaign. The goal of the chapter is to show how measurements taken in non-ideal conditions together with LES can be brought together to make source strength estimations from sparse measurements. Therefore, we focused on one measurement day during the ROMEO (ROmanian Methane Emissions from Oil and gas) campaign that was conducted in October of 2019 where measurements of methane leaking from an oil well were taken. We used ERA5 data to set up the meteorological boundary conditions for the LES and set-up the source in line with the configuration in the field. The weather conditions produced by the LES were in close agreement with ERA5, however the wind showed complex behavior due to the lack of large scale forcing. Therefore, to align the simulated plume direction with the field observations, we repeated the experiment with manipulated wind. Using the LES plume to infer the source strength of the measured plume was in line with the estimations

made using the tracer plume, with known source strength, that was emitted from the well location and measured simultaneously with the methane plume. To further utilize the LES, we also analyzed the higher order statistics of the simulated plume and found good agreement with previous modelling and laboratory experiments in channel flows. We have also derived a plume mixing length scale from the boundary layer height, the mean wind speed and convective velocity scale. We have found that this length scale coincides with the distance from the source at which the plume transfers from predominantly meandering dispersion to relative dispersion.

While LES has proven capable of correctly simulating plume dispersion, it still parametrizes the smallest eddies in a turbulent flow. A simulation method that resolves the full flow field is direct numerical simulations (DNS), however, highly turbulent flows are very computationally expensive. To test the ability of DNS to simulate plume dispersion we have performed a series of simulations in chapter 5. These simulations range from low to moderately turbulent conditions. In a next step, we compared these simulations with an LES and a wind-tunnel experiment. The study comprises of five DNS experiments with increasing Reynolds numbers and two LES experiments with high and low spatial resolution. Two plumes were released into a neutral flow over a flat terrain from point sources placed at 6% and 19% of the boundary layer height. Results for velocity statistics show very good agreement between all simulations and the experiment, with only cross-wind components of wind variances being slightly underestimated in both LES and DNS. For the plume statistics, the mean plume is well represented in all simulations. However, only the two most turbulent DNS experiments were able to reproduce the higher order plume statistics correctly performing better than LES at downwind distances very close to the source. Further downwind, LES experiments outperform DNS as DNS tends to overestimate higher order statistics and we speculate this is an effect of the low Reynolds number. Despite being more computationally expensive, the most turbulent DNS being around 3 times costlier than LES, DNS has proven to be a useful tool for dispersion studies, particularly very close to the source.

The last research chapter, chapter 6, focuses on plume measurement strategies in an urban setting. This chapter was inspired by a measurement campaign conducted in Hamburg, Germany in a suburban residential street. Based on the street layout, we built a mock urban set-up (MUST) into which we placed 11 ground sources in different positions regarding the buildings. Due to the lack of meteorological measurements from the campaign, we released the plumes into the neutrally stratified atmosphere. We sampled the plumes by taking virtual measurements along the street transects. We subsequently utilized the Weller method to infer the source strengths and estimate the source locations. We performed three DNS experiments with increasing Reynolds numbers, two of which had the same wind speed and in the third experiment the wind speed was doubled. The results show that all the runs have very similar mean vertical profiles of their first three statistical moments of velocity. There is also clear influence of the buildings on the flow

field as re-circulation is clearly visible behind the buildings. This re-circulation is caused by the pressure build-up on the windward side. There is also a clear influence of the buildings on the plumes, especially the ones placed in-between the buildings as the material from those plumes tends to stay trapped in the space between buildings. The application of the Weller method to estimate the source strength shows some clear drawbacks of the method. The method always places the source at a wrong location unless the transect was taken directly on top of the source. This is a direct consequence of the mean plume having a maximum concentration downwind from the source, irrespective of the wind speed. The method also wrongly estimates the source strength on almost all transects. The method, however, gives correct estimation on those transects where maximum concentration satisfies the equation the Weller method is based on. For a source of a certain strength, these transects are dependent on the wind speed, atmospheric stability and possible geometry affecting the plume spread.

Finally, in chapter 7, we give an overview of the most important findings and discuss the outlook for future research. We focus the discussion into two separate topics: measurements and modelling. We give some recommendations on measurement techniques based on our findings, mainly stressing the importance of measuring the wind. We also discuss our expectation for the Gaussian plume model to remain a go–to model for source estimation from measurements and give recommendations on how to further utilize DNS and LES in future studies.

Contents

Chapter 1

Introduction

1.1 Motivation

Climate change is taking the precedence as one of the most pressing societal issues. It directly impacts all aspects of life on Earth, from microbial to human. Many ecosystems can not adapt to the rapid change resulting in their disappearance, e.g. the decreasing amount of sea ice (IPCC, 2022) changes the polar ecosystems. Furthermore, global warming has direct impact on human health and economy. The climate predictions indicate higher occurrence of extreme weather events, such as heat waves or prolonged and intense hurricane seasons (IPCC, 2022). Climate change, or global warming, is a direct consequence of human actions. Since the industrial revolution in the late 1800s the human activity and increase in the global population has brought a drastic increase in the concentration of greenhouse gases (GHGs) in the atmosphere. The most notable anthropogenic GHG is carbon dioxide (CO_2), a by-product of burning processes, which has reached a global average concentration of 420 parts per million (ppm) (i.e. out of a million molecules of air 420 are $C0_2$ molecules) as of April 2022 (Dlugokencky, 2022), an ≈ 50 % increase since pre-industrial times.
While CO_2 has been in the focus of climate change mitigation efforts, due to its very long residence time in the atmosphere (order of hundreds of years) and comparatively high concentrations to other GHGs (Dlugokencky, 2022), other compounds have also experienced a sharp increase. The GHG which is the main motivation behind the research presented in this thesis is methane (CH_4).
Methane, on a 100 year timescale, has 28 times stronger warming potential than CO_2 (Saunois et al., 2020). Global mean concentrations of CH_4 in comparison to CO_2 are relatively small, averaging at 1908.9 parts per billion (ppb) (i.e. out of a billion molecules of air, 1908.9 are CH_4 molecules) in January 2022 (Fig. 1.1, Dlugokencky (2022)). And while CO_2 is mainly emitted as a by-product of burning processes, sources of CH_4 are many and diverse. Methane sources can be divided into two main origin subgroups: anthropogenic and natural. In natural circumstances, CH_4 is emitted as a by-product of decomposition processes such as rotting of organic matter or production in the animal digestive system. Methane is also naturally released in the form of leaks of natural gas from its underground reserves, such as thawing of permafrost or wetlands emissions (Christensen et al., 2004; Saunois et al., 2020). As it is true with other GHGs, the drastic rise in CH_4 is a direct consequence of human activity. While, for example, methane emitted by the decomposition of organic matter in wetlands by bacteria is responsible for approximately one third of total emissions, the emissions are considered constant over the years and do not contribute to the global CH_4 increase (Saunois et al., 2020). In contrast, agricultural and fossil fuel emissions are responsible for respectively 38 % and 19 % of total emissions, and are expected to increase with the rise in the global human population and its demands for food and energy (Montzka et al., 2011). The sources of methane vary greatly in size as well. The horizontal extent of the sources can span from the order of centimeters in pipe leaks (Maazallahi et al., 2020) to hundreds of meters

across (landfills, lakes, wetlands) (e.g. Hensen & Scharff (2001); Mønster et al. (2015); Łakomiec et al. (2021)). The largest part of methane is removed through oxidation by OH, and a smaller part through soil uptake (Saunois et al., 2020). The overview of methane budget is given in Fig. 1.2.

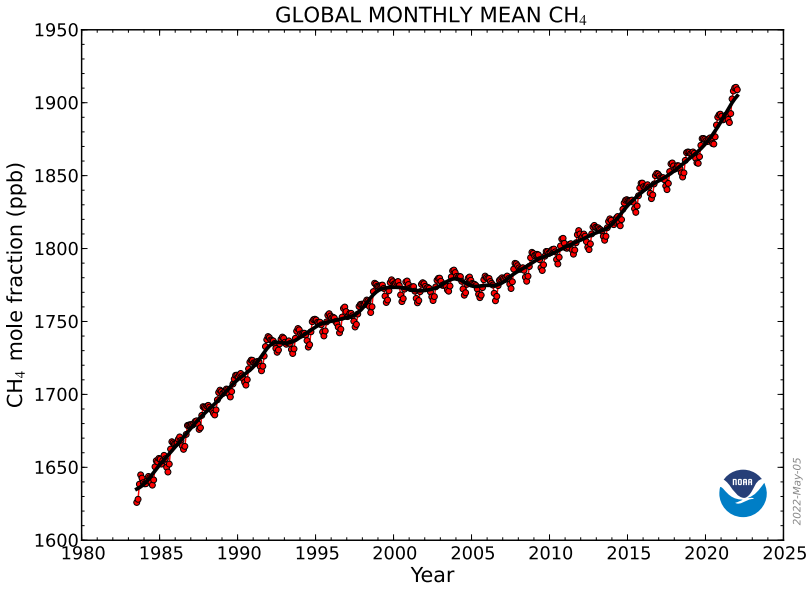

Figure 1.1: Globally-averaged, monthly mean atmospheric methane abundance from all NOAA marine methane monitoring stations for the time span 1983 – 2022. The red lines and circles indicate globally-averaged monthly means, while the black like indicates the long term trend (equivalent of a 12-month running average). Figure taken from Dlugokencky (2022).

Unlike CO_2, methane has a relatively short lifetime in the atmosphere of $\approx$ 9 years (Montzka et al., 2011). Consequently, immediate reduction in the total emissions can lead to a quick response in the abundance of atmospheric methane. To be able to cut the emissions, however, first the sources of methane should be identified and quantified. To help tackling this issue on the European scale, the MEthane goes MObile - MEasurements and MOdelling (MEMO^2) project started in 2017. The goal of the project was to combine measurement techniques used for fast identification and quantification of sources with state-of-art modelling techniques in order to help with the mitigation of methane emissions. The project comprised of over 20 academic and non-academic collaborators spread out over 7 countries. As also pointed out in Saunois et al. (2020), there are significant discrepancies in emission estimates from bottom-up techniques (measurements of local sources extrapolated to national scales), and top-down approach (atmospheric observations combined with inverse-modelling techniques). As the first goal, MEMO^2 aimed to tackle this problem by targeting local emissions from different

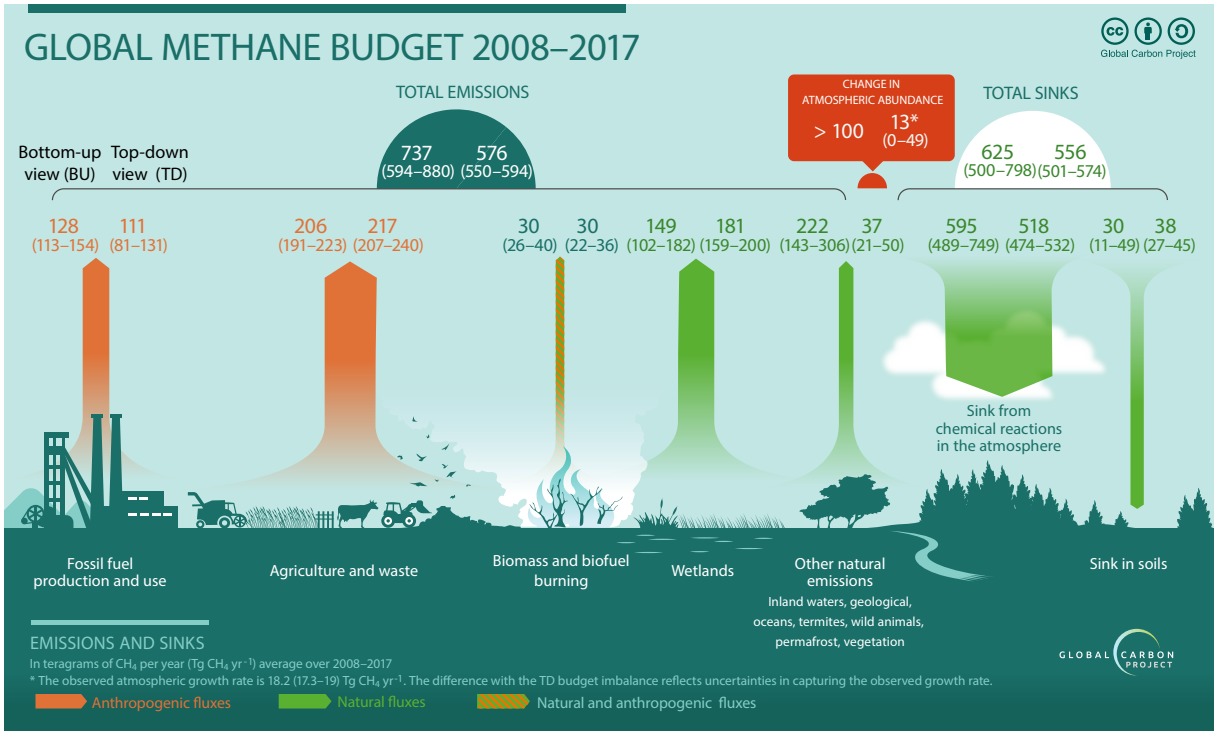

Figure 1.2: Global methane budget for the period 2008 – 2017. Figure taken from Saunois et al. (2020).

source types (fugitive urban emissions, wetlands, waste water facilities, oil and gas production, coal mining etc.) to improve bottom-up estimates. The second goal of the project was to combine dispersion modelling across scales and the measurements.

The aim of my research, and the work presented in this thesis, within MEMO^2 scope, is to use high resolution modelling techniques to identify sources of error in the local measurement techniques in order to help set-up future campaigns. Furthermore, this project aims to identify best practices in close-source high-resolution modelling, and set-up a framework for recreating realistic measurement simulations that can further the insight into measured plumes.

1.2 Identification and quantification of methane sources across scales

A large variety of measurement techniques has been developed and is currently in use for finding and quantifying methane emissions. These techniques vary greatly in the way they are deployed and on the timescales over which measurements are taken. A short overview is given here and some of the advantages and disadvantages are pointed out.

With the precision and resolution of instruments for measuring GHGs concentrations placed on satellites constantly increasing, satellite measurements of methane plumes are being frequently used to estimate emissions from large emitters (Irakulis-Loitxate et al., 2021). With the ability to take daily measurements over the whole globe satellite data are especially useful for identifying emissions in areas that are difficult to reach geographically. Furthermore, these satellite data are particularly useful in estimating cumulative emissions from cities as shown in Plant et al. (2022), who used TROPOMI satellite data to estimate urban methane emissions for several large cities across the globe. However, while advantages of using satellite images for emission estimations are clear, satellites are still constrained by their spatial and temporal resolutions. Furthermore, to estimate emissions it is of crucial importance to have wind information, as wind is the main driver of dispersion. The wind data is often unavailable, especially in remote areas, and has to be inferred from (re)analysis products provided by meteorological models (e.g. ERA5, Hersbach et al. (2020)), which can add to the estimation error.
Information from long-term atmospheric observatories, apart from information on background concentrations, also provide information about nearby emissions. The advantage of this approach is having a very long time series of concentrations, which give insight into global trends. However, using such data to infer emissions from a region depends on the resolution and meteorological information of the flux-inversion models (Wunch et al., 2019).
Measuring methane emissions using instruments placed on aircraft is particularly useful for determining basin-scale emissions. The aircraft can provide data down-wind and up-wind from an area of interest, thus making the emission estimation posible using the mass balance approach (Cui et al., 2019). However, as with the approaches above, it is difficult, if not impossible, to identify individual sources using the aircraft measurements.

Therefore, in order to pin-point specific sources of methane and to estimate emissions from only that source without interference from near-by sources, measurement methods that focus on close-source plumes need to be employed.
A method that allows for high mobility and measurements under favorable atmospheric conditions is with instruments placed on mobile platforms. For example, instruments placed in cars have been used to measure emissions from agriculture (Hensen et al., 2006), landfills (Hensen & Scharff, 2001; Mønster et al., 2015), wastewater treatment facilities (Bakkaloglu et al., 2022), oil and gas industry (Foster-Wittig et al., 2015; Robertson et al., 2017), urban pipeline leaks (Phillips et al., 2013; Maazallahi et al., 2020), etc. Instruments have also been placed on unmanned areal vehicles (UAVs) (Andersen et al., 2018, 2021; Vinković et al., 2022), but there is also carry-on equipment that enables the measurements being taken while walking or biking (Villa et al., 2020). It is clear mobile methods allow for a large variety of sources to be singled out and independently quantified. These methods

also allow for the measurement of multiple sources during a single day and for coverage of large areas in so-called screening drives, in which new plumes might be identified. There are, however, some notable drawbacks to these techniques. Firstly, the car measurements rely on accessible roads, which may not be favorable for measurements depending on the local wind direction. Also, traffic can influence the dispersion and the sources themselves might not always be reachable (e.g. being on a private property). Secondly, and most notably, these measurement techniques rely on taking downwind plume transects (mostly on one height) and are often paired with simple models, such as the Gaussian plume model (GPM) or mass balance approaches, to estimate the emission rate of the measured source. However, the GPM, or other empirical estimation models, are simplified and time-averaged approaches of plume dispersion. These models require many assumptions that are not necessarily fulfilled in relation to the turbulent nature of the atmosphere close to the ground. For example, the GPM assumes constant wind speed and a wind direction independent of height, an assumption that is generally not true in the surface layer, where most of the measurements are taken (e.g. Pope (2000); Wyngaard (2010)). Therefore, the influence of fluctuating motions in the atmosphere, which are not taken into account by simplified models, are contributing to the estimation error. How much the atmospheric variability is contributing to the estimation error is a still poorly researched subject and will be a main topic in this thesis.

1.3 Turbulent plume dispersion

It is clear from the large variety of methane sources described above that also a large variety of source sizes exist. The source size and source elevation play an important role in plume dispersion, as will be shown in this section. Here, turbulent plume dispersion will be introduced as intuitively as possible focusing on plumes from point sources. This is done for simplicity, but also because the research presented in the next chapters is focused on point source emissions. To be able to measure turbulent plumes and to interpret the measurements correctly, the underlying dispersion mechanisms should be thoroughly understood.
Plumes are very intuitive to visualize, as most people have seen them in the form of a chimney smoke, exhaust pipe or cigarette smoke. Even from purely visual observations, it is clear the plumes become turbulent in nature as soon as they leave their source (Fig. 1.3).

Figure 1.4 illustrates the plume as it progresses through different dispersion regimes. As the plume is released from the source it is constrained by the shape of the source itself, e.g. a pipe with a diameter d_ϕ will release a plume of the same size $L_\phi = d_\phi$. Immediately after release, a full range of turbulent eddies start to act on the plume, some of them larger than the plume, some the size of – or smaller than – the plume. The larger eddies

Figure 1.3: Chimney smoke. Picture taken from `https://www.freeimages.com/photo/smoke-coming-out-of-smokestack-1947381`

tend to carry the whole plume, displacing it from its centerline position (yellow dotted line in Fig. 1.4). This motion is generally known as meandering. Eddies smaller than the plume size entrain fresh air into the plume, thus making the plume slowly grow around its center of mass (solid yellow line in Fig. 1.4). This process is known as relative dispersion (e.g. Seinfeld (1986); Cassiani et al. (2020)). As a result, the total plume dispersion σ_{tot} at any given downwind distance x can be described by these two phenomena following a simple relation (Gifford, 1959):

$$\sigma_{tot}^2(x) = \sigma_{meand}^2(x) + \sigma_{relat}^2(x), \tag{1.1}$$

where σ_{meand} is the plume dispersion due to meandering, and σ_{relat} is the relative dispersion contribution to the total plume growth. The relative contribution of each of these processes depends on the size of the plume itself. Very close to the source, where the plume is still narrow, meandering will be the dominant process, while further downwind, as the plume diameter L_ϕ grows, the relative dispersion becomes dominant. The inset of Fig. 1.4 shows a turbulent energy spectra $S(k)$ in relation to an instantaneous plume width L_ϕ at some downwind location, highlighting the relationship of the plume size and

the two dispersion regimes: as the plume grows, the range of eddies that can entrain air becomes larger, while the range of eddies responsible for meandering gets smaller. The two blue semicircles in Fig. 1.4 represent eddies of the same size. The eddy closer to the source is larger than the plume, and hence will contribute to meandering. The eddy further downwind is of a size comparable to the size of the plume, and will therefore contribute to relative plume growth. It is also visible from the inset that a transient area exists in which both of the regimes are equally important.
Following this, it is clear that a large range of motions is responsible and equally important for turbulent plume dispersion.

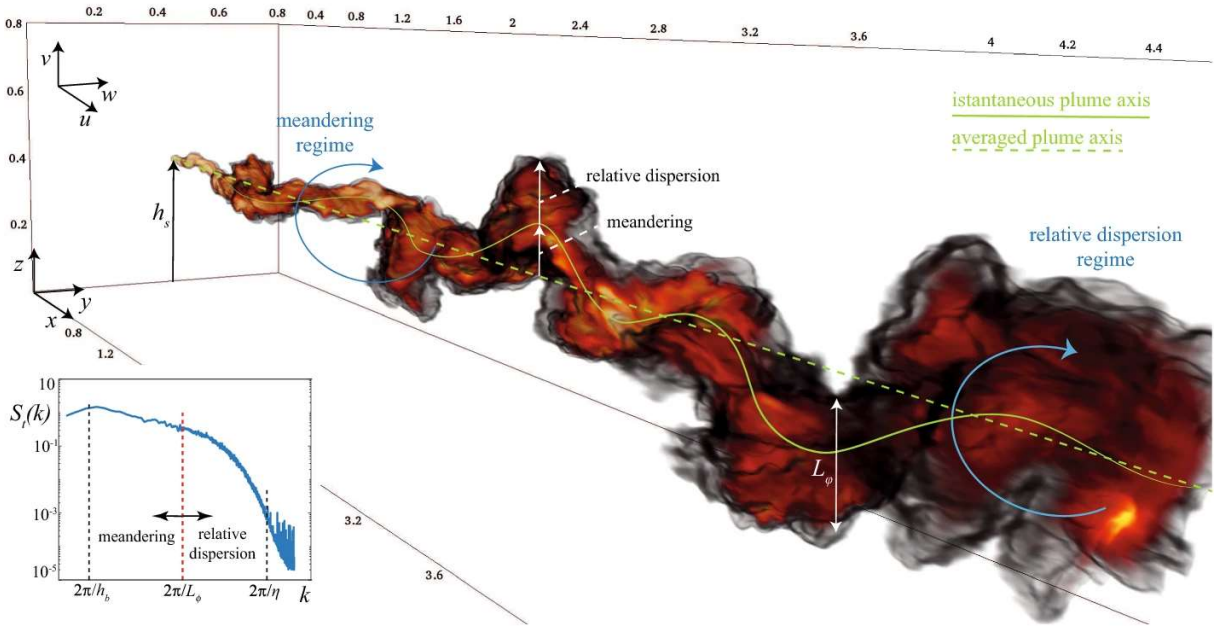

Figure 1.4: Volume rendering of a plume released from a point source in a large-eddy simulation. Figure taken from Cassiani et al. (2020).

1.4 Plume dispersion: experiments and modelling

Understanding mechanisms of plume dispersion is relevant for many fields of study, from work presented here concerning methane dispersion, to biology, civil protection in case of a military threats, etc. An overview of plume dispersion research up to this point in time has been given in Cassiani et al. (2020). In this work, large efforts have been employed in trying to explain dispersion in different settings, either urban or rural, and conditions, e.g. in stable or unstable atmospheres.

1.4.1 Experimental techniques

Experimental research can be split into two categories, each with its advantages and disadvantages: laboratory studies in wind tunnels or water tanks and open field release experiments. The experiments in the former group mainly focused on elevated or ground releases into neutral surface flows (e.g. Fackrell & Robins, (1982a,b); Nironi et al. (2015); Eisma et al. (2018)). The advantage of these experiments is their reproducibility and the controlled setting that allows for research of fundamental drivers behind dispersion. Every aspect of these experiments is controllable and full profiles (vertical and horizontal) of plumes can be captured. Furthermore, the experiments can be run for extended periods of time and statistically significant datasets can be acquired. Therefore, this makes these experiments suitable for benchmarking the performance of numerical models. However, the idealized setting of laboratory experiments and the scale of motions being restricted by the size of the experiment itself, makes that these flows are rarely found in nature.
In contrast, the open field experiments capture all relevant atmospheric processes in the measurements. These experiments are often used for establishing parametrizations for different numerical models (e.g. Barad (1958); Finn et al. (2018)). However, these experiments are very difficult to set-up as a large variety of instruments is necessary to sample the exact conditions in the atmosphere, not only at the ground but also in the vertical dimension (e.g. temperature, humidity, and wind speed profiles, surface heat fluxes). Since plume dispersion depends on the atmospheric conditions, especially the wind, these measurements are crucial for analysing the measured plume and ultimately correctly estimating the source strength. Furthermore, measuring the plumes themselves is a complicated endeavor, as, depending on the distance from the source and the release height, the profiles of the plumes might be beyond the reach of ground based instruments. This can be circumvented by the use of UAVs and aircrafts, but due to the limited time they can spend in flight, these datasets are usually not large. As with any other measurement or experiment set in the real atmosphere, plume dispersion suffers from lack of reproducibility. Lastly, the atmospheric conditions are constantly changing (daily cycle of surface fluxes, changing wind speed and/or direction etc.), therefore the duration of constant atmospheric conditions can be quite short and statistical robustness of the measurements might be difficult to reach.

1.4.2 Modelling

From the discussion above, it is clear that the proper description of plume dispersion, encompassing all relevant scales of motion, will be extremely challenging for any numerical model. There are many numerical models currently used that study dispersion from different approaches (see Cassiani et al. (2020)). The most fundamental way of categorizing these models is by the coordinate system they are in. The first category are models

that solve the motion from a perspective of a single particle that moves through space (Lagrangian) and the second category are models that look at the motion from a grid-point perspective (Eulerian). In the scope of this thesis, only the Eulerian framework will be discussed. Eulerian models can then be further categorized by how they deal with turbulence. Essentially, the exact concentration at any in-plume location can be known from the advection-diffusion equation which, in its non-parametrized and non-averaged form, describes the plume dispersion fully:

$$\frac{\partial c}{\partial t} + u_i \frac{\partial c}{\partial x_i} - D \frac{\partial^2 c}{\partial x_i^2} = 0. \tag{1.2}$$

Here, c is the instantaneous concentration at the location (x,y,z), u_i is the instantaneous turbulent wind in the direction i = [x,y,z], and D is the molecular diffusivity. Ideally, the turbulent wind would be known in each point and at each time instant, inferred from Navier-Stokes equations and solved simultaneously with the concentration field. This approach is known as direct numerical simulation (DNS). While DNS has been used for plume dispersion studies, it is generally disregarded for atmospheric dispersion research, since it is unfeasible for highly turbulent flows due to extremely large computational costs. In this thesis a non-dimensional number will be used as a measure for turbulence. This so-called Reynolds number is defined as $\mathrm{Re} = (L\,U)/\nu$ where is L is a characteristic length scale, U is a velocity scale and ν is kinematic viscosity. Therefore, atmospheric flows that are very turbulent have high Re, while laminar flows have very low Re. A characteristic of turbulent flows is that they become Reynolds number independent at a certain value of Re. This means that the higher-order statistics of the flow converge to certain profiles that do not improve by further increasing the Re. Whether or not DNS can produce flows that are turbulent enough and in which higher-order statistics of dispersing plumes become Reynolds number independent will be the topic of Chapter 5.
Large-eddy simulations (LES) also solve the velocity field simultaneously with the concentration field, but in LES only bigger eddies are resolved while small-scale turbulence is parametrized with subgrid-scale (SGS) models (e.g. Deardorff (1973); Pope (2000)). This way the LES can achieve very turbulent flows at reasonable computational costs. However, the parametrization is usually grid-size dependent. Therefore, when a very detailed resolution is required, as for example close to a plume source, the computational costs quickly increase.
There is also a subset of Eulerian models that are based on solving the Reynolds-averaged Navier-Stokes (RANS) equations. In these models, the turbulence is parametrized through one of the many turbulence closure models (Cassiani et al., 2020). Even though the research on RANS models dates back to Csanady (1967) and are still in use today, they fall out of the scope of this thesis. The simplest of Eulerian models is the Gaussian plume model (GPM) which assumes constant wind and diffusion and follows directly from eq. 1.2:

$$C(x,y,z) = \frac{Q}{2\pi\sigma_y(x)\sigma_z(x)\overline{u}} \exp\left(-\frac{(y-y_s)^2}{2\sigma_y^2(x)}\right)\left[\exp\left(-\frac{(z-z_s)^2}{2\sigma_z^2(x)}\right) + \exp\left(-\frac{(z+z_s)^2}{2\sigma_z^2(x)}\right)\right], \tag{1.3}$$

where C is the mean concentration field at location (x,y,z), Q is the emission rate located at (0,y_s,z_s), $\overline{u}$ is the mean wind directed along the x axis, and $\sigma_y(x)$ and $\sigma_z(x)$ are functions that describe the plume spread along the y and z axes. The equation 1.3 is shown with the extra exponential term that accounts for the reflection from the surface (Csanady, 1973). Fundamentally, the GPM (Fig. 1.5 (b)) is a result of averaging an infinite number of instantaneous turbulent plumes (Fig. 1.5 (a)). Figure 1.5 shows the stark difference between a fully turbulence resolving model and the simplest model that uses time-averaged fields. Since the GPM is often used in combination with mobile plume measurements to infer emission rates, and considering scope of the MEMO^2 project, it will be discussed in detail in the next chapter.

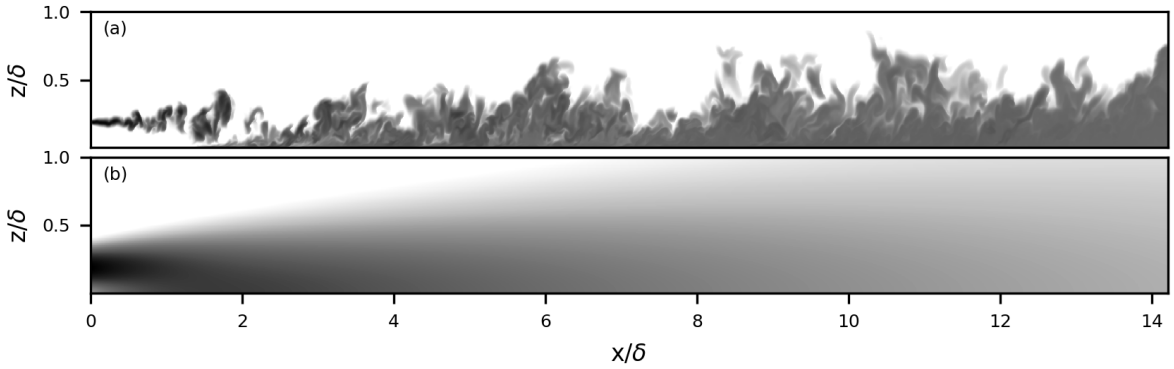

Figure 1.5: A comparison of the point-source plume in a (a) DNS and (b) GPM with arbitrary emission strengths but with the same wind speed at the source height and in neutral atmospheric conditions.

1.5 Thesis outline and main research questions

In this section a summary of the main research questions addressed in this thesis is given through a short description of topics in each chapter.

Chapter 2

In this chapter a short overview of the plume modelling techniques used in this thesis is given. This chapter is also used to give a more in-depth description of the main physical processes behind plume dispersion.

Chapter 3

This chapter focuses on the two commonly used measurement techniques, OTM33a and one-dimensional plume transects. The main research question of this chapter is: **What is the influence of atmospheric variability on the errors in estimated emission rates?** This question was addressed by conducting a LES of point-source plume dispersion in a neutral atmosphere over a flat terrain. This is the most canonical and well-studied case of atmospheric turbulence and can be used to benchmark future studies in more complicated settings.

Chapter 4

As part of the MEMO^2 project, many measurement campaigns were conducted with different sources of methane in focus. One such campaign, ROMEO, focused on methane emissions from Romanian oil and gas industry. Here, available measurements from the campaign in combination with ERA5 reanalysis data were used to simulate one measurement day. The questions addressed here was: **Is it possible with high-resolution LES to reproduce a measurement day. And what further plume information can be inferred from LES that would be unavailable from the measurements?**

Chapter 5

As previously mentioned, DNS is considered unsuitable for conducting plume dispersion research for its inability to achieve very high Re number flows usually encountered in the atmosphere. However, DNS has been shown in previous atmospheric studies to be turbulent enough for all the relevant statistics to be captured. The same idea is behind this chapter: **What is the limit at which higher-order statistics of turbulent plumes become Reynolds number independent and what is the computational cost of reaching this limit using DNS?**

Chapter 6

This final research chapter deals with a similar research topic as the first chapter. Since plume dispersion in the first chapter focuses on point-source plumes over flat terrain, point source emissions from cities cannot be addressed. However, cities are a large source of methane, and therefore many measurement campaigns are being conducted there. The presence of objects (such as houses) complicates turbulent dispersion. However, the models that are being used to estimate emissions are very simple and empirical. Therefore, the main question of this chapter is: **How sensitive is one of the commonly used city source estimation models to atmospheric turbulence and what are the main contributors to estimation errors?**

1.5.1 Chapter 7

The last chapter gives the overview of the most relevant findings presented in this thesis and puts them in the broader perspective on research of dispersion on small scales. It also gives context and recommendations for further research on the topics presented in the thesis.

Chapter 2

Background on plume dispersion modelling

2.1 Introduction

Some of the main concepts behind plume dispersion and plume dispersion modelling have been mentioned in the previous chapter. However, considering the scope of this thesis, we find a more detailed description of the modelling techniques used is needed. As previously mentioned, there is a plethora of models developed for studying plume dispersion on various scales. We focus here on the models that can be characterized as Eulerian and model plumes very close to the source, i.e. up to a few kilometers. Therefore, in this chapter we give the background on the three main models used in this thesis: the Gaussian plume model (GPM), direct numerical simulations (DNS) and large-eddy simulations (LES). The latter two will be given through the prism of MicroHH model (van Heerwaarden et al., 2017) that has been used to perform the simulations.

2.2 Gaussian plume model

One of the simplest models describing plume dispersion is the Gaussian plume model (GPM). It is the solution of the advection-diffusion equation (eq. 1.2) when the assumptions of stationarity, constant wind with height and constant diffusivity are made. Since the GPM is widely used in combination with plume measurements for estimation of source strengths, which will be thoroughly discussed in chapter 3, we here demonstrate in short how the model is derived from eq. 1.2 as it benefits the reader in understanding the model. To this end, we repeat the advection-diffusion equation (e.g. Seinfeld (1986)) in its non-parametrized and non-averaged form:

$$\frac{\partial c}{\partial t} + u_i \frac{\partial c}{\partial x_i} - D_i \frac{\partial^2 c}{\partial x_i^2} = 0. \tag{2.1}$$

Where c is the concentration at (x,y,z,t), u_i is the instantaneous wind in three principal directions $i = [x, y, z]$ and D_i is the turbulent diffusivity. As for any other turbulent process, eq. 2.1 is subject to Reynolds decomposition, i.e. all variables in the equation can be written as the sum of their mean and variable parts:

$$\phi = \overline{\phi} + \phi' \tag{2.2}$$

where ϕ is an arbitrary variable. After decomposition, eq. 2.1 takes the form

$$\frac{\partial(\overline{c} + c')}{\partial t} + (\overline{u_i} + u_i') \frac{\partial(\overline{c} + c')}{\partial x_i} - D_i \frac{\partial^2(\overline{c} + c')}{\partial x_i^2} = 0. \tag{2.3}$$

The main two assumptions behind the Gaussian plume model are stationarity of the flow and x-aligned wind, constant in time and with height. This annihilates all time dependent terms and terms containing v and w components from eq. 2.3. A further assumption of

the GPM is that diffusivity in the wind (x) direction is negligible compared to diffusivity in the y and z directions. As a result, eq. 2.3 shortens to:

$$\overline{u}\,\frac{\partial \overline{c}}{\partial x} = D_y\,\frac{\partial^2 \overline{c}}{\partial y^2} + D_z\,\frac{\partial^2 \overline{c}}{\partial z^2}. \tag{2.4}$$

A further assumption is that the diffusion processes are independent in the two cross-wind directions, therefore the concentration at a certain location (x, y, z) can be regarded as a superposition of the two dispersion processes and written as $\overline{c(x,y,z)} = \overline{c_1(x,z)}\,\overline{c_2(x,y)}$. After substitution of the expressions for concentration and some rearrangement, eq. 2.4 takes the form:

$$\overline{c_1}\left(\overline{u}\,\frac{\partial \overline{c_2}}{\partial x} - D_y\,\frac{\partial^2 \overline{c_2}}{\partial y^2}\right) + \overline{c_2}\left(\overline{u}\,\frac{\partial \overline{c_1}}{\partial x} - D_z\,\frac{\partial^2 \overline{c_1}}{\partial y^2}\right) = 0. \tag{2.5}$$

For the right side of eq. 2.5 to be satisfied, the both expressions in parenthesis on the left side of the equation must equal zero. Therefore, we have a second-order partial differential equation for each of the orthogonal dispersion directions.
Their solutions can be found by substituting the expressions for concentrations with their Fourier transforms

$$\overline{c_1(\omega,x)} = \frac{1}{2\pi}\int_{-\infty}^{\infty} \overline{c_1(x,z)}\,\exp\left(-i\omega\,z\right) dz \tag{2.6}$$

Therefore the equation for determining i.e. $\overline{c_1(x,z)}$ takes the shape

$$\frac{\partial}{\partial x}\left(\frac{1}{\sqrt{2\pi}}\int_{-\infty}^{\infty} \overline{c_1(x,z)}\,\exp(-i\omega z)\,dz\right) = \frac{D_z}{\overline{u}}\frac{\partial^2}{\partial z^2}\left(\frac{1}{\sqrt{2\pi}}\int_{-\infty}^{\infty} \overline{c_1(x,z)}\,\exp(-i\omega z)\,dz\right). \tag{2.7}$$

With some rearrangement of eq. 2.7, a partial differential equation for $\overline{c_1(\omega,x)}$ can be written as

$$\frac{\partial}{\partial x}\overline{c_1(\omega,x)} = -\omega^2\frac{D_z}{\overline{u}}\overline{c_1(\omega,x)}, \tag{2.8}$$

which has the solution

$$\overline{c_1(\omega,x)} = \alpha\,\exp\left(-\omega^2\frac{D_z}{\overline{u}}x\right), \tag{2.9}$$

where α is an integration constant. From the inverse Fourier transform

$$\overline{c_1(x,z)} = \frac{\alpha}{\sqrt{2\pi}}\int_{-\infty}^{\infty} \overline{c_1(\omega,z)}\,\exp(i\omega z)\,d\omega = \frac{\alpha}{\sqrt{2\pi}}\int_{-\infty}^{\infty} -\exp\left(\omega^2\frac{D_z}{\overline{u}}x - i\omega z\right) d\omega \tag{2.10}$$

it is trivial to show that the solution for $\overline{c_1(x,z)}$ is:

$$\overline{c_1(x,z)} = \alpha\sqrt{\frac{\overline{u}}{2D_z\,x}}\,\exp\left(-\frac{\overline{u}\,z^2}{4D_z\,x}\right). \tag{2.11}$$

Similarly, the solution for $\overline{c_2(x,y)}$ is found

$$\overline{c_2(x,y)} = \beta\sqrt{\frac{\overline{u}}{2D_y\,x}}\,\exp\left(-\frac{\overline{u}\,y^2}{4D_y\,x}\right) \tag{2.12}$$

where β is an integration constant. Therefore, the solution for $\overline{c(x,y,z)}$ can be written as

$$\overline{c(x,y,z)} = \gamma \sqrt{\frac{\overline{u}}{2D_y\,x}} \sqrt{\frac{\overline{u}}{2D_z\,x}} \exp\left(-\frac{\overline{u}\,z^2}{4D_z\,x}\right) \exp\left(-\frac{\overline{u}\,y^2}{4D_y\,x}\right) \tag{2.13}$$

with $\gamma = \alpha \cdot \beta$. Finally, the general form of the Gaussian plume model is obtained from the initial condition $\int_{-\infty}^{\infty}\int_{-\infty}^{\infty} \overline{c}\,dy\,dz = Q$ where Q is the source strength, and defining the dispersion coefficient as $\sigma_i^2 = \frac{2\,D_i\,x}{\overline{u}}$:

$$\overline{c(x,y,z)} = \frac{Q}{2\pi\overline{u}\sigma_y\sigma_z} \exp\left(-\frac{z^2}{2\sigma_z^2}\right) \exp\left(-\frac{y^2}{2\sigma_y^2}\right). \tag{2.14}$$

Equation 2.14 is the solution placed in the infinite space and with the source located in the origin. However, for practical purposes of plume dispersion in the atmosphere, the physical space has boundaries (i.e. the ground) with sources that are placed relative to these boundaries. This means that the plume may be subjected to reflection of concentration from the boundaries. In this case, the solution is found as a superposition of the main plume and another plume of the same emission strength with a position mirrored on the boundary (Csanady, 1973). As a result, a plume emitted from a point source with strength Q and at height H above the ground can be described with the expression:

$$\overline{c}(x,y,z) = \frac{Q}{2\pi\sigma_y(x)\sigma_z(x)\overline{u}} \exp\left(-\frac{(y-y_s)^2}{2\sigma_y^2(x)}\right) \left[\exp\left(-\frac{(z-H)^2}{2\sigma_z^2(x)}\right) + \exp\left(-\frac{(z+H)^2}{2\sigma_z^2(x)}\right)\right]. \tag{2.15}$$

This equation is the standard Gaussian plume model that is commonly used in the source strength estimations in combination with plume measurements taken in the field (e.g. Caulton et al. (2018)). The dispersion coefficients, $\sigma_y(x)$ and $\sigma_y(x)$, apart from the downwind distance from the source, also depend on the atmospheric stability. For example, a plume dispersing in stable atmosphere will be narrower than one dispersing in the unstable condition. This is due to the turbulent mixing which is enhanced for the unstable conditions through the buoyancy effects. The dispersion coefficients are empirically determined from field release experiments and their expressions depend on the stability class of the atmosphere (e.g. Barad (1958).

2.3 MicroHH model

The main idea behind the work presented in this thesis is to use high-resolution modeling techniques to bring further insight into plume dispersion. The model used here is the MicroHH model developed by van Heerwaarden et al. (2017), which is capable of performing both DNS and LES. In this section we give only the governing equations and physical parameterizations relevant for the studies presented in this thesis. For further description of MicroHHs capabilities, numerical schemes and the tests performed to benchmark the model, we refer the reader to van Heerwaarden et al. (2017) and the GitHub repository `https://microhh.github.io/`.

2.3.1 Governing equations

MicroHH solves the equations for conservation of mass, momentum and energy under the anelastic approximation. The approximation means that profiles of potential temperature, pressure and density exhibit only small deviations from their base state, i.e. $\psi = \psi_0(z) + \psi'$, where the subscript zero and the prime denote mean state and its deviation and ψ is an arbitrary variable. The simplification to the anelastic approximation is known as the Boussinesq approximation which assumes ψ_0 is constant with height. We omit writing down equations in the Boussinesq form as they are easily obtained by implementing the constant density assumption in the anelastic form. However, both approximations are available in MicroHH.

We write the equation for conservation of mass under the anelastic approximation as

$$\frac{\partial \rho_0 u_i}{\partial x_i} = \rho_0 \frac{\partial u_i}{\partial x_i} + \rho_0 w H_\rho^{-1} = 0, \tag{2.16}$$

where u_i is the velocity vector (u,v,w), x_i denotes one of the principal directions (x,y,z) and $H_\rho \equiv \left(\frac{1}{\rho_0}\frac{d\rho_0}{dz}\right)$ is the scale height for density.

The conservation of momentum equation can be written in its flux form

$$\frac{\partial u_i}{\partial t} = -\frac{1}{\rho_0}\frac{\partial \rho_0 u_i u_j}{\partial x_j} - \frac{\partial}{\partial x_i}\left(\frac{p'}{\rho_0}\right) + \delta_{i3} g \frac{\theta_v'}{\theta_{v0}} + \nu \frac{\partial^2 u_i}{\partial x_j^2} + F_i. \tag{2.17}$$

Here, θ_v' is the perturbation virtual potential temperature, θ_{v0} is the reference virtual potential temperature, p' is the pressure perturbation, g is the gravitational constant, ν is the kinematic viscosity, δ is the Kronecker delta and F_i is the external forcing coming from parametrizations of the large scale.

The equation for obtaining the pressure field is written in full as

$$\frac{\partial}{\partial x_i}\left[\rho_0 \frac{\partial}{\partial x_i}\left(\frac{p'}{\rho_0}\right)\right] = -\frac{\partial}{\partial x_i}\left(\frac{1}{\rho_0}\frac{\partial \rho_0 u_i u_j}{\partial x_j}\right) + \delta_{i3} g \frac{\partial}{\partial x_i}\left(\frac{\theta_v'}{\theta_{v0}}\right) + \nu \frac{\partial^3 u_i}{\partial x_i \partial x_j^2} + \frac{\partial F_i}{\partial x_i}. \tag{2.18}$$

Now, we consider the transport of scalars. Since methane is considered a scalar on timescales of hours studied in this work, methane is governed in the simulation through the conservation of scalar equation:

$$\frac{\partial \zeta}{\partial t} = -\frac{1}{\rho_0}\frac{\partial \rho_0 u_j \zeta}{\partial x_j} + \kappa_\zeta \frac{\partial^2 \zeta}{\partial x_j^2} + S_\zeta \tag{2.19}$$

where ζ is an arbitrary scalar, κ_ζ is its diffusivity, and S_ζ represents all sources and sinks of the scalar.

The final equation solves the conservation of energy and we give it here in its dry form for potential temperature θ. For a moist atmosphere, the liquid potential temperature θ_l has a similar shape:

$$\frac{\partial \theta}{\partial t} = -\frac{1}{\rho_0}\frac{\partial \rho_0 u_j \theta}{\partial x_j} + \kappa_\theta \frac{\partial^2 \theta}{\partial x_j^2} + \frac{\theta_0}{\rho_0 c_p T_0} Q. \tag{2.20}$$

In this equation κ_θ is the thermal diffusivity, c_p is the specific heat capacity, T_0 is the referent temperature, and Q are the external sources and sinks of heat.
Equations 2.17–2.20 form the dynamic core of the MicroHH model. Solving these equations is performed numerically in a domain discretized on a staggered Arakawa C-grid. The time advancement in the model is achieved by using the Runge-Kutta integration scheme of either third- or fourth-order. The spatial discretization is done through the finite difference scheme which can be either second- or third-order. From the discretized expressions a higher order spatial operators, such as advection or diffusion, can be derived. For more information on discretization, we refer to van Heerwaarden et al. (2017).
When the equations 2.16 – 2.20 are explicitly solved, the model performs a direct numerical simulation (DNS). However, due to resolution requirements (and consequently computing power) necessary to achieve numerical stability in the model (Pope, 2000) only low to moderately turbulent flows are attainable from DNS simulations. These flows are not turbulent enough compared to atmospheric turbulence. As a side note, we will show in Chapter 5 that this requirement does not have to be fulfilled in order to perform realistic scalar dispersion. When domains of several kilometers are considered, eddies on the scale of millimeters can be filtered out and modeled with a sub-grid parameterization. In this way a large-eddy simulation (LES) is preformed and the flow can reach high turbulence.

2.3.2 Large-eddy simulations

Sub-filter scale model

As mentioned above, implementing LES requires very small eddies to be filtered out from the simulations. The filtering is done similarly as Reynolds decomposition shown in eq. 2.2. Therefore, for example the velocity components, would be split into part that is being resolved $\widetilde{u}_i$ and the part that is filtered out u_i'', i.e.

$$u_i = \widetilde{u}_i + u_i''. \tag{2.21}$$

When the filtering is applied to the momentum equation (eq. 2.17), it can be re-written as

$$\frac{\partial \widetilde{u}_i}{\partial t} = -\frac{1}{\rho_0}\frac{\partial \rho_0 \widetilde{u}_i \widetilde{u}_j}{\partial x_j} - \frac{\partial \pi}{\partial x_i} - \frac{1}{\rho_0}\frac{\partial \rho_0 \widetilde{\tau_{ij}}}{\partial x_j} + \delta_{i3} g \frac{\widetilde{\theta}_v{}'}{\theta_{v0}} + \nu \frac{\partial^2 u_i}{\partial x_j^2} + F_i. \tag{2.22}$$

where π is the modified pressure

$$\pi \equiv \frac{\widetilde{p'}}{\rho_0} + \frac{1}{3}(\widetilde{u_i u_i} - \widetilde{u}_i \widetilde{u}_i), \tag{2.23}$$

and τ_{ij} is the anisotropic subfilter-scale momentum flux tensor

$$\tau_{ij} \equiv \widetilde{u_i u_j} - \widetilde{u}_i \widetilde{u}_j - \frac{1}{3}(\widetilde{u_i u_i} - \widetilde{u}_i \widetilde{u}_i). \tag{2.24}$$

The tensor above contains the filtered product of unfiltered velocity components, which is unknown and needs to be parameterized. In MicroHH this is done with the Smagorinsky-Lily model (Lily, 1968; van Heerwaarden et al., 2017) and the tensor takes a shape like:

$$\tau_{ij} = -K_m \left(\frac{\partial \widetilde{u_i}}{\partial x_j} + \frac{\partial \widetilde{u_j}}{\partial x_i} \right). \tag{2.25}$$

The expression in brackets is the strain tensor defined as:

$$S_{ij} = \frac{1}{2} \left(\frac{\partial \widetilde{u_i}}{\partial x_j} + \frac{\partial \widetilde{u_j}}{\partial x_i} \right) \tag{2.26}$$

and K_m is the subfilter eddy diffusivity which also needs to be modeled as:

$$K_m = \lambda^2 S \left(1 - \frac{\frac{g}{\theta_{v0}} \frac{\partial \widetilde{\theta_v}}{\partial z}}{Pr_t S^2} \right)^{\frac{1}{2}}, \tag{2.27}$$

where $S \equiv \sqrt{2 S_{ij} S_{ij}}$ is the magnitude of the strain tensor, and Pr_t is the turbulent Prandtl number set to one third in the model. The mixing length λ is defined as

$$\frac{1}{\lambda^n} = \frac{1}{[\kappa(z + z_0)]^n} + \frac{1}{c_s \Delta} \tag{2.28}$$

where $\Delta \equiv (\Delta x \Delta y \Delta z)^{1/3}$ is the filter size (or sub-filter length scale), n is a free parameter set to 2, c_s is the Smagorinsky constant and κ is the von Karman constant.
The same filtering approach is applied on all the governing equations discussed in the previous section. For the scalars, the filtered equation becomes:

$$\frac{\partial \widetilde{\zeta}}{\partial t} = -\frac{1}{\rho_0} \frac{\partial \rho_0 \widetilde{u_j} \widetilde{\zeta}}{\partial x_j} - \frac{1}{\rho_0} \frac{\partial \rho_0 R_{\zeta,j}}{\partial x_j} + \widetilde{S_\zeta} \tag{2.29}$$

where $R_{\zeta,j}$ is, again, subfilter scalar flux that is modeled as:

$$R_{\zeta,j} = \widetilde{u_j \zeta} - \widetilde{u_j} \widetilde{\zeta} = -\frac{K_m}{Pr_t} \frac{\partial \widetilde{\zeta}}{\partial x_j}. \tag{2.30}$$

Surface model

Since a part of the turbulent motions is parametrized in LES, this also requires a parameterization of the surface-flow interface. To relate surface fluxes to their near-surface gradients the Monin-Obukhov similarity theory (MOST) is often used (Anderson & Meneveau, 2010). This MOST is also used in MicroHH, where the parametrization has been constrained to rough surfaces and very turbulent flows, as is often the case in the atmosphere. In MOST, the surface fluxes and the gradients just above the surface are related through empirical functions that depend on the first model level height z_1 and the Obukhov length $L \equiv -\frac{u_*^3}{\kappa B_0}$, where u_* is the friction velocity, κ is the von Karman

constant and B_0 is the surface kinematic buoyancy flux.
The momentum fluxes and friction velocity can therefore be connected to the wind gradient above the surface following the relation:

$$\frac{\kappa z_1}{u_*}\frac{\partial U}{\partial z} \approx -\frac{\kappa z_1 u_*}{\overline{u'w'}}\frac{\partial \tilde{u}}{\partial z} \approx -\frac{\kappa z_1 u_*}{\overline{v'w'}}\frac{\partial \tilde{v}}{\partial z} \approx \phi_m\left(\frac{z_1}{L}\right). \tag{2.31}$$

Here, $U = \sqrt{\tilde{u}^2 + \tilde{v}^2}$ and $\overline{u'w'}$ and $\overline{v'w'}$ are the surface momentum fluxes. These variables can be found by relating surface roughness length z_{0m} and z_1, which yields:

$$u_* = f_m\left(U_1 - U_0\right), \tag{2.32}$$

$$\overline{u'w'} = -u_* f_m\left(\tilde{u_1} - \tilde{u_0}\right), \tag{2.33}$$

$$\overline{v'w'} = -u_* f_m\left(\tilde{v_1} - \tilde{v_0}\right). \tag{2.34}$$

where

$$f_m \equiv \frac{\kappa}{\ln\left(\frac{z_1}{z_{0m}}\right) - \Psi_m\left(\frac{z_0}{L}\right) + \Psi_m\left(\frac{z_{0m}}{L}\right)}. \tag{2.35}$$

Ψ_m and ϕ_m are empirical functions that depend on atmospheric stability. For an unstable atmosphere they have the form (Wyngaard, 2010)

$$\phi_m = \left(1 + \gamma_m|\zeta|^{\frac{2}{3}}\right)^{-\frac{1}{2}} \tag{2.36}$$

$$\Psi_m = 3\ln\left(\frac{1+\phi_m^{-1}}{2}\right), \tag{2.37}$$

where $\gamma_m = 3.6$ and $\zeta = \frac{z}{L}$, z is a height above the surface. For the stable atmospheric conditions they are (Wyngaard, 2010)

$$\phi_m = 1 + \lambda_m\zeta \tag{2.38}$$

$$\Psi_m = -\lambda_m\zeta \tag{2.39}$$

with $\lambda_m = 4.8$.
The same procedures are applied for scalar fluxes:

$$\frac{\kappa z_1 u_*}{\overline{\phi'w'}}\frac{\partial \tilde{\phi}}{\partial z} \approx \phi_h\left(\frac{z_1}{L}\right), \tag{2.40}$$

$$\overline{\phi'w'} = u_* f_h\left(\tilde{\phi_1} - \tilde{\phi_0}\right), \tag{2.41}$$

$$f_h \equiv \frac{\kappa}{\ln\left(\frac{z_1}{z_{0h}}\right) - \Psi_h\left(\frac{z_0}{L}\right) + \Psi_h\left(\frac{z_{0h}}{L}\right)}, \tag{2.42}$$

where Ψ_h and ϕ_h are defined in the same manner as for the momentum fluxes (Wyngaard, 2010), and for the unstable atmosphere they take the form (Wyngaard, 2010):

$$\phi_h = \left(1 + \gamma_h|\zeta|^{\frac{2}{3}}\right)^{-\frac{1}{2}} \tag{2.43}$$

$$\Psi_h = 3 \ln \left(\frac{1 + \phi_h^{-1}}{2} \right), \tag{2.44}$$

where $\gamma_h = 7.9$ and $\zeta = \frac{z}{L}$. For stable atmospheric conditions (Wyngaard, 2010):

$$\phi_h = 1 + \lambda_h \zeta \tag{2.45}$$

$$\Psi_h = -\lambda_h \zeta \tag{2.46}$$

with $\lambda_h = 7.8$. All of the above equations cannot be calculated without knowing the Obukhov length L. In the surface model L is calculated by relating the dimensionless number $\frac{z_1}{L}$ with the Richardson number. The definition of this relationship depends on the chosen boundary conditions. Here, we write the explicit form of the relation, which is used when both the friction velocity u_* and surface kinematic buoyancy flux B_0 are known:

$$Ri = \frac{z_1}{L} = -\frac{\kappa z_1 B_0}{u_*^3}. \tag{2.47}$$

2.4 Conclusions

In this chapter, we have given an overview of the three main techniques that are used in this thesis to simulate plume dispersion The relationship between the models and their ability to simulate the plume dispersion has not yet been discussed in detail. This will be the main topic in some of the following chapters: The relationship between the stationary GPM and non-stationary LES will be discussed in detail in chapter 3 and the ability of DNS and LES to simulate close-source plume dispersion is the topic of chapter 5.

Chapter 3

Evaluation of two common source estimation measurement strategies using large-eddy simulation of plume dispersion under neutral atmospheric conditions

This chapter is based on: Ražnjević, A., van Heerwaarden, C., & Krol, M. (2022). Evaluation of two common source estimation measurement strategies using large-eddy simulation of plume dispersion under neutral atmospheric conditions, Atmos. Meas. Tech., 15, 3611–3628, https://doi.org/10.5194/amt-15-3611-2022

Abstract

This study uses large-eddy simulations (LES) to evaluate two widely-used observational techniques that estimate point source emissions. We evaluate the use of car measurements perpendicular to the wind direction and the commonly used Other Test Method 33A (OTM33A). The LES study simulates a plume from a point source released into a stationary, homogeneous and neutral atmospheric surface layer over flat terrain. This choice is motivated by our ambition to validate the observational methods under controlled conditions where they are expected to perform well since the sources of uncertainties are minimized. Three plumes with different release heights were sampled in a manner that mimics sampling according to car transects and the stationary OTM33A method. Subsequently, source strength estimates are compared to the true source strength used in the simulation. Standard deviations of the estimated source strengths decay proportionally to the inverse of the square root of the number of averaged transects, showing statistical independence of individual samples. The analysis shows that for the car transect measurements at least 15 repeated measurement series need to be averaged to obtain a source strength within 40% of the true source strength. For the OTM33A analysis, which recommends measurements within 200 m from the source, the estimates of source strengths have similar values close to the source, which is caused by insufficient dispersion of the plume by turbulent mixing close to the source. Additionally, the derived source strength is substantially overestimated with the OTM33A method. This overestimation is driven by the proposed OTM33A dispersion coefficients, which are too large for this specific case. This suggests that the conditions under which the OTM33A dispersion constants were derived, were likely influenced by motions with length scales beyond the scale of the surface layer. Lastly, our simulations indicate that, due to wind-shear effects, the position of the time-averaged centerline of the plumes may differ from the plume emission height. This mismatch can be an additional source of error if a Gaussian plume model (GPM) is used to interpret the measurement. In case of the car transect measurements, a correct source estimate then requires an adjustment of the source height in the GPM.

3.1 Introduction

Reducing methane emissions can have a more immediate positive influence on the mitigation of climate change than reducing the emissions of carbon dioxide (e.g. Baker et al. (2015); Zickfield et al. (2017); Caulton et al. (2018)). However, methane is emitted by a high variety of activities, which makes the identification and quantification of the sources a complicated endeavour, and as such the methane budget is uncertain (e.g. Saunois et al. (2016)). In order to address the urgency in constraining the methane budget, the Methane goes Mobile - Measurements and Modelling ($MEMO^2$) project, in which our study is embedded, started in 2017. Reducing the uncertainties has two elements. First, methane sources need to be identified, and second, accurate measurements are needed to quantify the source magnitude. In this paper, we focus on the latter and demonstrate how three-dimensional large eddy simulations (LES) can help us in estimating the uncertainty in methods that derive the source strength from field observations, and in setting up appropriate measurement strategies.

Before presenting our study, we provide an overview of the state-of-the art in plume measurement techniques and three-dimensional simulation of dispersion. Observation of plumes can be performed using a wide range of techniques, such as satellite remote sensing (e.g. Houweling et al. (2014); Wunch et al. (2019)) and aircraft measurements (Cui et al., 2019), sensors mounted on towers (Röckmann et al., 2016), unmanned aerial vehicles (UAVs) (Berman et al., 2012; Andersen et al., 2018; Shah et al., 2019), and tracer release correlation techniques (Mønster et al., 2015; Mitchell et al., 2015). For the detection and quantification of local sources, techniques using mobile platforms are particularly useful, since they allow for large areas being covered with measurements in relatively short time period and quick source strength estimations using simple models. In this paper, we will analyze two prominent methods that are widely used: line observations made using driving cars, and stationary observations using the Other Test Method 33A (U.S. EPA, 2014). In these methods, the Gaussian plume model is used to translate observations of concentration and wind speed into an expected emission source strength.

The first method, car measurements, has been used for large variety of sources, i.e. leaks from gas and oil production facilities (e.g. Yacovitch et al. (2015); Atherthon et al. (2017); Baillie et al. (2019)), emissions from landfills (e.g. Hensen & Scharff (2001)), urban pipeline leaks (Phillips et al., 2013), and agricultural emissions (Hensen et al., 2006). Drawbacks of this method are its dependency on the available road infrastructure, the necessity to know the exact source location and the assumption of constant wind speeds that often needs to be made (e.g. Seinfeld (1986); Atherthon et al. (2017); Caulton et al. (2018)) The second method, the OTM33A method, combines downwind point measurements of methane concentrations and wind to derive the emission flux employing the Gaussian plume model. The OTM33A method has been used in estimation of emissions from oil and gas production facilities (e.g. Brantley et al. (2014); Lan et al. (2015); Foster-

Wittig et al. (2015); Robertson et al. (2017)) and the method has recently been evaluated by Edie et al. (2020). The advantage of this method is its relatively simple measurement process that relies on wind direction variations that move the plume over the stationary measurement device positioned directly downwind of the source. By averaging over a sufficient amount of time, a one-dimensional Gaussian profile of the plume can be recorded. Drawbacks of this method are its inability to account for buoyant plumes, variation in the emission and measurement heights and ground reflection of the plume. In particular, the latter requirement demands the observations to be done close to the source on distances of 20 - 200 m (U.S. EPA, 2014; Edie et al., 2020).

Both measurement techniques, as previously mentioned, rely on the Gaussian plume model to estimate emission rates. The Gaussian model is the solution to the advection-dispersion equation for a point source with the assumption of constant wind and dispersion coefficients that are functions of downwind distance and atmospheric stability (e.g. Seinfeld (1986)). As such, the methods compare the modeled stationary plume with the measured turbulent plume. Such comparison is bound to lead to estimation errors, unless enough measurements have been collected to average out the atmospheric variability. Therefore, a systematic and controlled study is needed to constrain the influence of turbulence on these measurement techniques. Apart from Caulton et al. (2018), who analysed the car transect method using LES and concluded that at least 10 transects are needed to average out the variability, such study has not been conducted to the best of our knowledge.

Three-dimensional simulation techniques, such as large-eddy simulation (LES) and direct numerical simulation (DNS), can aid in understanding and quantifying the uncertainties in the two measurement methods. In the past, LES and DNS have been used to study atmospheric dispersion. LES, which parametrizes the smallest scales of turbulence, has been successful in simulating dispersion at close and moderate distances from the source (e.g. Boppana et al. (2010, 2012); Matheou et al. (2016); Ardeshiri et al. (2020)). DNS, as it resolves all details of the flow, would be an ideal approach for studying plume dispersion, however, due to unfeasible computing costs involved, it cannot reproduce high Reynolds number flows (Pope, 2000). Nevertheless, in recent years DNS is becoming more affordable for atmospheric studies (e.g. Branford et al. (2011); Oskouie et al. (2017)), as computers have sufficient power to simulate atmospheric boundary layers with statistics that are slowly becoming Reynolds number independent.

In this study, we evaluate the car and OTM33A methods using LES. Numerous studies have shown that LES is an established tool for studying plume dispersion (e.g. Dosio & de Arellano (2006); Boppana et al. (2012); Ardeshiri et al. (2020); Cassiani et al. (2020)). Due to the high computational costs involved in LES, we limit this study to the lower atmospheric boundary layer under neutral conditions. The neutral atmospheric surface layer can be well represented by a turbulent channel flow and is one of the most canonical and well-studied cases of atmospheric turbulence. Moreover, the two measurement

methods are expected to perform well under neutral atmospheric conditions. This study, therefore, provides a baseline test for the two measurements methods. The LES represents the ideal experiment in which all sources of uncertainty are controllable and quantifiable. By using LES we are able to study the influence of turbulent fluctuations on plume dispersion and consequently on the measured plume, which can be used as a benchmark for future measurement campaigns.

This paper is structured as follows: In Section 3.2 we shortly describe the Gaussian plume model, since it is the basis for source estimation in the two studied measurement strategies. We also describe in detail the OTM33A and the car sampling methods. Furthermore, in Section 3.3, details of our numerical simulation setup are presented, as well as the implementation of Gaussian-shaped sources, which proved to be necessary for this study. In Section 3.4 the performance of LES is validated against a wind tunnel experiment, described by Nironi et al. (2015). Furthermore, the similarities of time averaged LES plumes and Gaussian plumes are discussed, followed by an analysis of the impact of plume averaging on source strength estimations. Finally, Section 3.5 provides an overview and discussion of our findings.

3.2 Measurement methods

Here, we discuss the two measurement methods: measuring from driving cars and the OTM33A method. Before discussing both in detail, we provide a brief overview of the Gaussian plume model as this is the essential model for both methods to convert concentration measurements into a source strength.

3.2.1 The Gaussian plume model

The simplest approach to describe plume dispersion is the Gaussian plume model, which represents the stationary solution to the advection-diffusion equation (e.g. Seinfeld (1986)). The solution to the equation with a reflective ground component is given by Eq. 3.1 (e.g. Csanady (1973)):

$$C(x,y,z) = \frac{Q}{2\pi\sigma_y(x)\sigma_z(x)\overline{u}} \exp\left(-\frac{(y-y_s)^2}{2\sigma_y^2(x)}\right)\left[\exp\left(-\frac{(z-z_s)^2}{2\sigma_z^2(x)}\right) + \exp\left(-\frac{(z+z_s)^2}{2\sigma_z^2(x)}\right)\right]. \tag{3.1}$$

Here, x direction is defined as the direction of the mean wind $\overline{u}$, y is the horizontal crosswind direction and z points away from the surface. C is the scalar concentration at the position (x,y,z), $\sigma_y(x)$ and $\sigma_z(x)$ are the plume dispersion parameters which depend on the distance from the source and the atmospheric stability. These parameters are calculated following one of many proposed parametrizations, most of which follow the

Pasquill-Gifford's stability class scheme (e.g. Seinfeld (1986); Briggs (1973); Korsakissok et al. (2009)). Q is the source strength positioned at ($x_s = 0$,y_s,z_s). The model has been studied in detail, and advanced versions are currently in use as a fast-response approach to scalar dispersion modeling (e.g. Cimorelli et al. (2005); Korsakissok et al. (2009)). One of the main assumptions of this model is the plume stationarity, which deviates greatly from the measured instantaneous plumes, and the model should be interpreted as an average of an infinite number of instantaneous plumes (e.g. Seinfeld (1986)). Studies suggest that the sufficient averaging time, depending on the distance from the source and the stability, ranges between 2 and 60 minutes (Fritz et al., 2005). For the neutral stability class D, which corresponds with our study, the averaging time ranges from 2 to 30 minutes at distances of 100 to 1000 m.

One set of dispersion coefficients σ_y and σ_z that is widely used (e.g. Korsakissok et al. (2009)) is the Briggs parametrization. This parameterization is appropriate for urban and for rural sites and is given in the form (Griffiths, 1994):

$$\sigma_i = \alpha x(1 + \beta x)^{\gamma}, \tag{3.2}$$

where i = (y, z) and α, β and γ are coefficients that depend on the dispersion direction, stability class, and orography of the site where measurements are taken and x [m] is the downwind distance from the source. For rural sites and neutral stability, coefficients have values of α = [0.08, 0.06], β = [0.0001, 0.0015] for the y and z directions respectively, and γ = - 0.5 for both directions.

3.2.2 OTM33A Measurement Method

The OTM33A method was developed by the US Environment Protection Agency (U.S. EPA, 2014). The method consists of two parts: detection of plumes and quantification of emissions. The detection is performed by driving downwind from the likely source, perpendicular to the mean wind direction, with the goal to detect the average plume centerline. After the average plume centerline is detected, the car is parked directly downwind from the source, at distance x $\in$ [20, 200] m. The inlet of the measurement device is oriented directly towards the mean wind direction in order to minimize the impact of turbulent eddies generated by the measurement equipment. Subsequently, the methane concentrations, wind speed, wind direction, and temperature are measured continuously for 20 min at the assumed height of the release. Emissions are quantified following the Gaussian plume equation, with the assumptions (i) the measurement inlet is positioned at the height of the release (ii) the measurement are taken directly downwind from the source and (iii) the reflection from the ground is negligible at [20-200] m from the source. Therefore, Q_{estim} [kg s^{-1}] can be estimated from:

$$Q_{estim} = 2\pi\sigma_y\sigma_z c_{max}\overline{u}, \tag{3.3}$$

where σ_y and σ_z [m] are dispersion coefficients that are provided in look-up tables. These coefficients depend on the distance from the source and the atmospheric stability. To calculate c_{max}, methane concentrations are binned in wind-direction bins of 10°, and the average methane concentration in every bin is calculated. c_{max} [kg m^{-3}] is taken from the bin with the highest averaged concentration. $\overline{u}$ denotes the average wind speed [m s^{-1}] during the measuring period. Note that equation 3.3 does not have a term that accounts for plume reflection at the surface, buoyancy of the plume, and a possible difference between the source height and the measurement height. Equation 3.3 assumes no background concentrations.

The OTM33A method is used for the quantification of small (point-like) sources. Since the distances over which this method is employed are not sufficient for the plume to fully disperse, the plume is still narrow, patchy, and meandering in behavior (Gifford, 1959). Moreover, the method assumes that the terrain over which the plume is dispersing is flat without any obstacles that can distort the shape of the plume.

3.2.3 Estimating source strength from car measurements using an Inverse Gaussian method (IGM)

The car measurement method consists of measurements perpendicular to the mean wind direction, downwind from the source (e.g. Yacovitch et al. (2015)). This method, as opposed to OTM33A, provides the one-dimensional spatial extent of the plume by moving the instrument instead of relying on the wind direction changes to move the plume over the instrument. Usually, the meteorological conditions are measured simultaneously by either instruments placed on site (Caulton et al., 2018) or instruments placed on the car (Atherthon et al., 2017).

The method for estimating the source strength from measured plume transects is based on the ratio of modeled and measured concentrations. If the mean wind is along the x-axis and drive-by's are in the cross-plume y-direction, then the source strength can be calculated by summing the modeled and measured concentrations C_{meas} along the y-axis and by scaling the source strength (Caulton et al., 2018)

$$Q_{estim} = \frac{\sum_y C_{meas}}{\sum_y C_{Gauss}} \times Q_r \tag{3.4}$$

where C_{Gauss} are the modeled concentrations. To calculate C_{Gauss}, Eq. 3.1 is used with the referent emission rate Q_r, measured mean wind $\overline{u}$, and dispersion coefficients chosen for the encountered conditions in the field. The estimates rely on line integral in the y

direction. Therefore, the technique is not sensitive to possible misrepresentation of lateral dispersion in the modelled plume but assumes that the vertical dispersion is described correctly. Equation 3.1 takes into account the reflection from the ground and assumes that the exact location and height of the source are known. In this procedure, no background concentrations are assumed.

3.3 Case set-up and numerical simulation

Numerical simulations have been performed using MicroHH (`www.microhh.org`, van Heerwaarden et al. (2017)).

We study a stationary, homogeneous, turbulent channel flow in which a non-reactive scalar is being released from multiple point sources. The model set-up follows the experimental study by Nironi et al. (2015).

Our simulation uses a second-order-accurate finite volume scheme to solve dynamics in the system. For the advection, sixth order interpolations are applied and for the advection of scalars a flux limiter is applied to ensure monotonicity. Time is advanced with a third order Runge-Kutta time-integration scheme. We use periodic boundary conditions for the three wind components on the lateral boundaries of the domain. The second-order Smagorinsky model is used for the subgrid parametrization of the velocity components. The upper boundary condition is free-slip and the tangential components of velocity are assumed zero ($\frac{\partial u}{\partial z} = \frac{\partial v}{\partial z} = 0$). There is no penetration through the upper boundary ($w = 0$). The lower boundary has no-slip ($u = v = 0$) boundary conditions and no penetration through the lower boundary. For the scalar, in-flow and out-flow conditions were set on all the lateral boundaries to prevent it from re-entering the domain. Dirichlet boundary conditions are set for in-flow on the left and upper boundary and Neumann conditions for the out-flow on the right and lower boundary.

3.3.1 Implementation of sources

The MicroHH code has been extended to support placement of point and line sources of scalars at arbitrary positions in the domain. In order to avoid numerical artefacts, which would arise from injecting tracer mass into the simulation at a single grid cell, the implementation of a point source is achieved in the form of a 3-D Gaussian function that spans over $[-4\sigma_i, 4\sigma_i]$, where σ_i is the standard deviation in the respective coordinate direction (i = x, y, z), around the source location (x_0, y_0, z_0). The value of σ_i is chosen by the user, dependent on the required size of the source. Consequently, the source S that is added to the grid has the shape

$$S(x, y, z) = Q\ s\ \exp\left(-\frac{(x - x_0)^2}{\sigma_x^2} - \frac{(y - y_0)^2}{\sigma_y^2} - \frac{(z - z_0)^2}{\sigma_z^2} \right). \tag{3.5}$$

Here, Q [kg s^{-1}] is the total source strength that is released in the simulation, distributed over the 3-D Gaussian function $S(x, y, z)$. The source S integrates into Q by using a normalization constant:

$$s = \frac{1}{\sqrt{\pi^3}\sigma_x\sigma_y\sigma_z \mathrm{erf}(4)^3}. \tag{3.6}$$

3.3.2 Numerical experiment

As previously mentioned, the domain was set up to mimic the experimental study of Nironi et al. (2015), with a domain size of 6144 × 1536 × 1000 m, and sources were placed at 306 × 770 × [0, 60, 190] m. The friction velocity had the value $u_\tau = 0.16$ m s^{-1}, the eddy viscosity was $\nu = 0.011$ m^2 s^{-1} and the wind speed at the top of the domain was $u = 5$ m s^{-1}. The domain was discretized on a 1536 × 384 × 360 grid, with uniform spacing in the horizontal direction (Δx = Δy = 4 m), and a stretched grid in the vertical with Δz ≈ 1 m close to the surface and Δz ≈ 6 m at the top. The sources were added into the simulation as a 3D (elevated sources) or 2D (ground source) Gaussians (section 3.3.1) with $\sigma_{source} = 4$ m, equivalent to one grid box size. Note that the source at 0 m was not part of the Nironi et al. (2015) experiment. Nevertheless, we add this experiment because ground sources are often encountered when measuring in the field. The source strength for all three sources is set to $Q_{source} = 1 \cdot 10^{-3}$ kg s^{-1}. The simulation was first run for 25200 s to achieve statistical stability of the flow, after which the three sources were released into the flow and run for an additional 3600 s. The concentrations were recorded every 1 s on multiple downwind distances over various 2D domain transects (x – y, x – z or y – z).

3.3.3 Plume sampling

Simulating plume meandering

Figure 3.1a shows that, when our simulated plume is sampled according to the OTM33A protocol, we capture very narrow plume with wind direction that spans over [-10°, 10°] angle. We hypothesize that this is caused by the absence of large-scale meandering in our simulation. The external forcing of our flow is determined by a large-scale pressure gradient force directed constantly in the x direction of the domain. As a result, our LES only contains meandering motions that are driven by turbulent motions in the domain itself and not by larger scale flow fluctuations. Close to the emission source, the OTM33A sampling protocol always samples the plume. Consequently, the sampled concentration variations visible in Fig. 3.1a are mostly caused by the applied shape of the emission source (see section 3.3.1). Small-scale turbulent motions did not have time to mix the plume, which is consequently still retaining the shape of the source. In order to impose the lacking large-scale meandering, we mimicked meandering of the plume by moving the

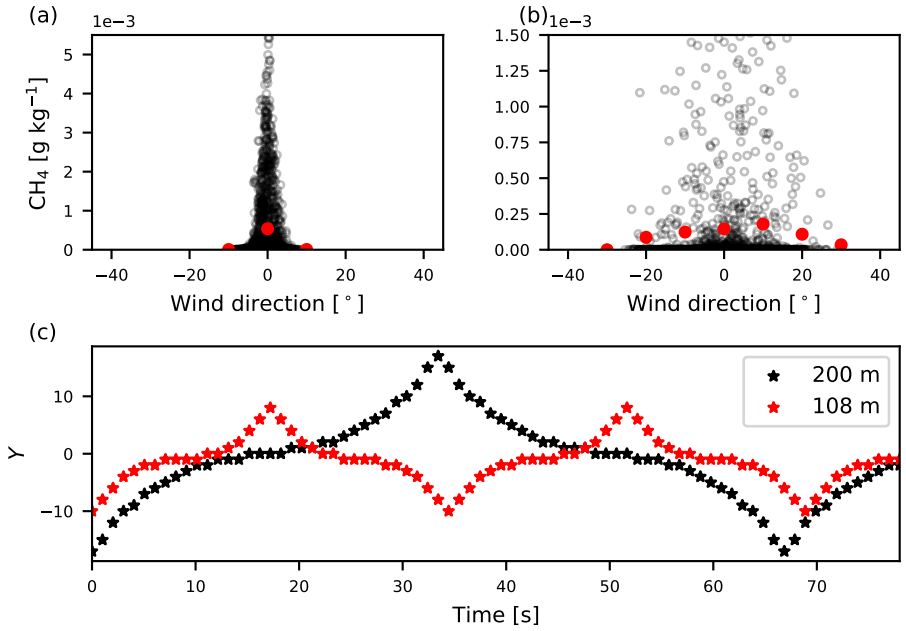

Figure 3.1: (a) Methane concentration plotted against the wind direction according to OTM33A protocol for the case when no meandering is imposed. (b) Methane concentrations against wind direction with imposed meandering. Red circles indicate bin averages. Bins of 10° are used. (c) An example of the sampling pattern used to impose meandering for two distances from the source.

measurement point through the plume, perpendicular to the mean wind.

The sampling was performed on an angle of $\theta \in$ [-15°, 15°] around the plume centerline in the y direction. This angle was chosen in order not to sample outside of the plume. Onto the sampling angle, the instantaneous wind direction measured at each sampled point was added. We move the location at which we record the sample back and forth between the plume edges, with a denser sampling close to the centerline, as shown in Figure 3.1c (see Appendix 3.6). Note that we impose larger values of Y when we sample further downwind from the source. Figure 3.1 b shows the resulting OTM33A concentrations after we sampled the plume with the additional meandering.

We have sampled the plume at four downwind distances that fall into the proposed range (x = [20, 200] m, Edie et al. (2020)). The samples were taken at x = [48, 108, 152, 200] m from the source. All three plumes were sampled at the height of their release (i.e. [0, 60, 190] m) with the frequency of 1 Hz for a duration of 30 min. Each plume was sampled 20 times with a time delay of 60 s between each sample to achieve reliable statistics.

Simulating car sampling

The sampling of the plume mimicking the car movements was performed in a similar manner as OTM33A measurements. The concentration measurements were taken perpendic-

ular to the mean wind over the whole width of the domain (1536 m). The measurements were taken at the height of the release for each of the three emission heights, and at eight downwind distances from the source, x = [108, 200, 312, 624, 1248, 2500, 3748, 5000] m.

Firstly, we have recorded instantaneous plume transects over the y direction, i.e. mimicking an infinitely fast car. These instantaneous samples are used as a benchmark for plume measurements taken with realistic car speeds. We have taken 70 sets of measurements, each consisting of 100 plume transects to gather statistics. The time delay between each set of measurements was taken as 10 s. The transects have also been sampled with a 10 s delay in between them. Secondly, to study the possible influence of driving speed on the source strength estimations, we have sampled the plume with two different car speeds, V = [4, 12] m s^{-1}, with a sampling frequency of 1 Hz. The 1 Hz frequency represents the highest temporal resolution available from our simulation. As with the instantaneous plume transects, we recorded 70 sets of 100 plumes, with a time delay of 10 s between sets and individual plumes respectively.

To study the influence of atmospheric variability on the source strength estimation when using the Gaussian plume model, we averaged plumes in each of the 70 sets for each sampling strategy. The averaging was performed such that the resulting plume $\overline{C_j}^t$ (j $\in$ [1, 384] is the position on the y-axis) is an average of t ($t \in [1, 100]$) previous plumes. In this way, we transformed each set of turbulent plumes into a set of averaged plumes. The first element is a single, non-averaged plume, and the last plume is an average of 100 plumes.

3.3.4 Statistical properties of the plumes

To further our understanding of the processes that govern plume dispersion close- and far-field from the source, plume dispersion can be subdivided into two processes. The first process (relative dispersion) is mixing by the turbulent eddies with a size smaller than or comparable to the size of the plume. The second process (meandering) is the displacement of the plume center of mass by the turbulent eddies that are larger than the size of the plume (e.g. Dinger et al. (2018)).
To separate the influence of plume meandering from the influence of relative dispersion on the total plume growth, we can define relevant plume metrics in an absolute coordinate system (i.e. in relation to the ground) and a relative coordinate system (i.e. dispersion around instantaneous center of mass). First, the center of mass of the instantaneous plume relative to the surface, z_m, on its y-z transect is defined as:

$$z_m(x,t) = \frac{\int c(x,y,z,t)\, z\, dz\, dy}{\int c(x,y,z,t)\, dz\, dy}. \tag{3.7}$$

An ensemble average over many such instantaneous plumes will be equal to the center of mass of the time averaged plume $\overline{z_m}$. Next, different metrics that measure plume

displacement from its center of mass are defined. First, the absolute fluctuation z' is the displacement of an in-plume particle from the mean center of mass $\overline{z_m}$. Second, the relative fluctuation z'_r is the displacement of a in-plume particle from the instantaneous plume center of mass z_m. Third, z'_m is the displacement of the instantaneous plume centerline from the mean plume center of mass. These three metrics relate to each other as:

$$z' = z - \overline{z_m}, \quad z'_r = z - z_m, \quad z'_m = z_m - \overline{z_m}. \tag{3.8}$$

Now the vertical plume widths, stemming from the two dispersion processes $\sigma_{z,mean}$ (meandering) and $\sigma_{z,mix}$ (mixing) are defined as:

$$\sigma^2_{z,meand}(x,t) = \frac{\int c(x,y,z,t)\, z'^2_m \, dy\, dz}{\int c(x,y,z,t)\, dy\, dz}, \quad \sigma^2_{z,mix}(x,t) = \frac{\int c(x,y,z,t)\, z'^2_r \, dy\, dz}{\int c(x,y,z,t)\, dy\, dz}. \tag{3.9}$$

A similar expression applies to the total plume spread $\sigma_{z,tot}$ around the mean center of mass z_m:

$$\sigma^2_{z,tot}(x,t) = \frac{\int c(x,y,z,t)\, z'^2 \, dy\, dz}{\int c(x,y,z,t)\, dy\, dz}, \tag{3.10}$$

where

$$\sigma^2_{z,tot} = \sigma^2_{z,meand} + \sigma^2_{z,mix}. \tag{3.11}$$

Similar expressions apply to dispersion in y direction.

3.4 Results

3.4.1 Velocity and mean plume statistics

As a first step, the velocity statistics from the LES are validated against wind tunnel measurements presented in Nironi et al. (2015). The statistics are obtained as time (60 samples over an hour of simulation) and horizontal (over the whole domain) averages. Figure 3.2 a shows discrepancies between the non-dimensional wind speeds in the experiment and the LES. The wind speed at the top of the boundary layer in the LES is 4.9 m s^{-1}, which is very close to the value of 5 m s^{-1} presented in Nironi et al. (2015). However, the friction velocities, u_*, have values of 0.163 m s^{-1} and 0.185 m s^{-1} in the LES and the experiment respectively. As a result, the mean wind speeds differ when normalization with u_* is used. Another possible reason of the discrepancies is the so-called overshoot of the mean wind in LES, which has has been addressed previously (e.g. Brasseur & Wei (2010); Ardeshiri et al. (2020)). Overshoot in LES has been found to depend on the subgrid-scale (SGS) model, grid aspect ratio, grid resolution and the wall model. Despite

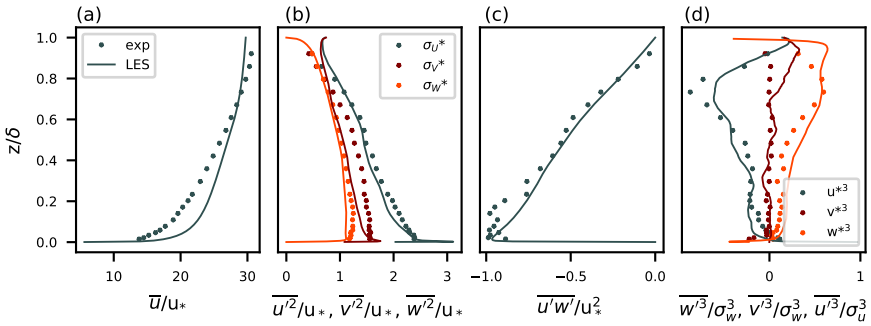

Figure 3.2: Vertical profiles of non-dimensional velocity statistics and comparison with the Nironi et al. (2015) data. (a) Mean longitudinal wind speed, purple line indicates the law of the wall with u_* from Nironi et al. (2015). (b) Variances of three wind components, (c) Reynolds stress and (d) triplet correlations.

the slight discrepancy in the mean wind, very good agreement is found between the wind speed variances (Fig. 3.2 b) and covariances (Fig. 3.2 c). Very good agreement is found for the triplet correlations as well (Fig. 3.2 d). Ardeshiri et al. (2020) also reproduced the Nironi et al. (2015) case using LES, and presented very similar results.

Following the good agreement of the higher order velocity statistics, we expect that the mixing of the plume in the cross-wind directions is well represented in the LES. The longitudinal mean wind affects the advection of the plume, i.e. the time the plume spent in the atmosphere being mixed by the turbulent eddies. Consequently, the statistics of the Nironi et al. (2015) plumes and the LES plumes cannot be compared at the same downwind distances. They can, however, be compared at the same effective distances from the source x_*, defined as the downwind distance x scaled with one eddy overturn distance X:

$$x_* = \frac{x}{X} = \frac{x}{\overline{u}T} = \frac{u_* x}{\overline{u}\delta}, \tag{3.12}$$

where T is the characteristic eddy overturn time, $\overline{u}$ is the mean wind speed, u_* is the friction velocity and δ is the boundary layer height. The downwind distance x_{LES} at which the LES plume has spent an equal amount of "mixing-time" compare to the Nironi et al. (2015) plume (x_N) is:

$$x_{LES} = \frac{u_{*,N}}{u_{*,LES}} \frac{\overline{u_{LES}}\,\delta_{LES}}{\overline{u_N}\,\delta_N} x_N. \tag{3.13}$$

Figure 3.3 shows a comparison of the first four central moments, raised to the power of $\frac{1}{n}$, $n = [1, 2, 3, 4]$, respectively, of the mean plume concentrations at the distance $x_N = 2.5\,\delta$. The moments are calculated over the horizontal and vertical plume transects at the height of the release and the y-position of the source respectively. The comparison is shown for

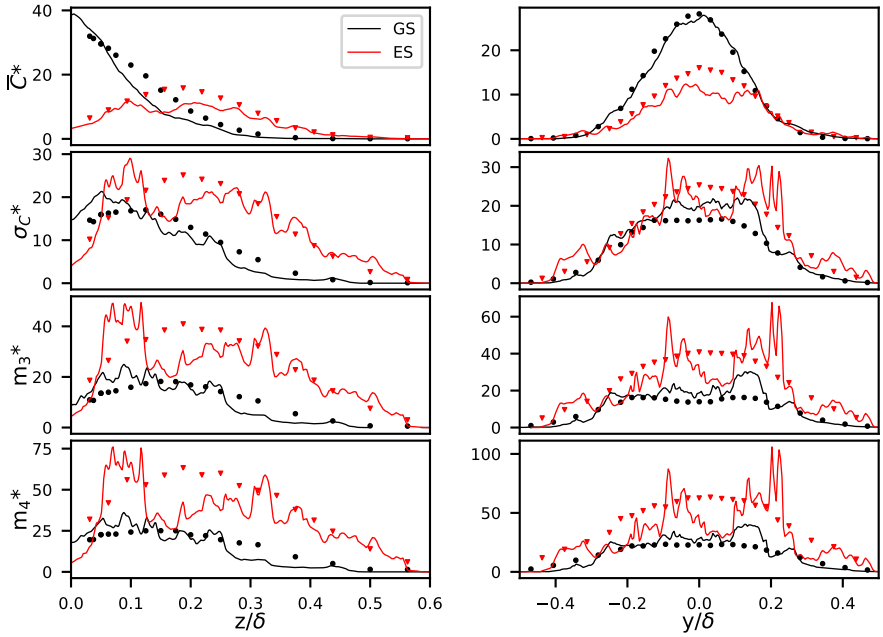

Figure 3.3: Vertical (left column) and horizontal (right column) profiles of the first four central moments of plume concentration raised to the power of $\frac{1}{n}$, $n = [1, 2, 3, 4]$ respectively. Lines denote LES results and symbols are corresponding results from Nironi et al. (2015). GS (black) denotes the source emitted at 0.06δ and ES (red) the source at 0.19δ. The transects are taken at $x_N = 2.5\delta$ for the experiments. The corresponding values for x_{LES} are 4.5 and 4.2δ for GS and ES, respectively.

the plumes released at 0.06 δ and 0.19 δ. The moments have been normalized (denoted by superscript *) with the plume emission rate Q [g s^{-1}], free-stream velocity u_∞ [m s^{-1}] and the height of the boundary layer δ, e.g. $C^* = C\frac{u_\infty \delta^2}{Q}$ is the normalized mean plume concentration. The mean plume profiles (Fig. 3.3 first row) show very good agreement over both transects: peaks of concentration and the plume width are well captured in the LES. The variances for the sources at 0.19δ (Fig. 3.3 second row) also show very good agreement. For the plume emitted closer to the ground, the variances agree well with the experiment at the edges of the plume, but are higher in the LES in the plume centerline. The same can be observed for the other two moments shown here, the skewness m_3^* and kurtosis m_4^* (Fig. 3.3 bottom two rows). Note here that, for higher moments, LES curves do not show the same smoothness visible in the experiment despite the 600 samples used to calculate the average.

To give the reader an intuitive understanding of the spatial distribution of the plumes, Figure 3.4 shows instantaneous x-z cross-sections of the three simulated plumes at the y position of the source (y_s). The lowest plume stays relatively close to the surface and slowly mixes up with the increasing distance from the source. The middle plume stays compact around the emission height for a relatively short time before it is transported towards the surface. In contrast, the highest plume stays elevated for considerable distance

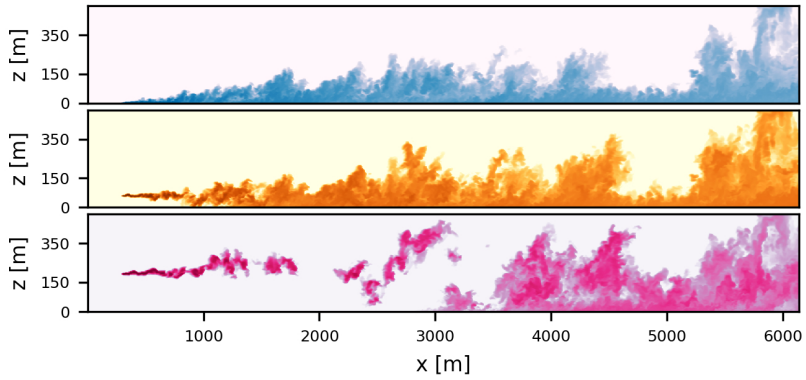

Figure 3.4: Snapshot of x-z transects of the three plumes taken through the plume centerline. Blue, orange, and pink correspond to emission heights of 0, 60, and 190 m, respectively.

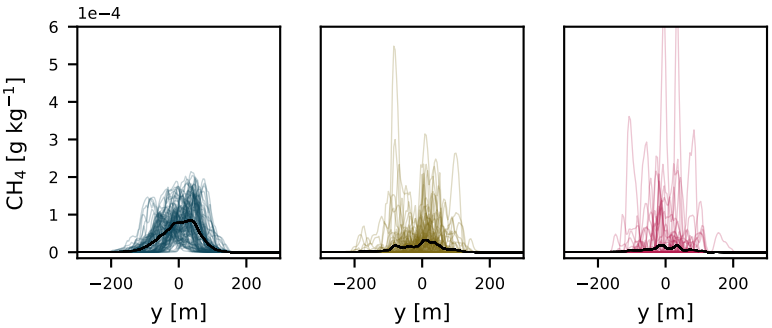

Figure 3.5: Example of 100 instantaneous transects from 3 plumes, taken at the emission height of the respective plumes, at a distance of 1248 m from the source. The mean of the 100 plumes is shown in black. Blue, brown, and pink correspond to emission heights of 0, 60, and 190 m, respectively.

from its source ($\approx$ 3000 m) before it gets transported to the surface. While elevated, the highest plume exhibits highly meandering behavior: the spread of the plume around its instantaneous center of mass is narrow, and is transported and broken up by larger eddies.

To illustrate these meandering motions, Figure 3.5 shows 100 instantaneous y-transects taken at emission height for each plume, separated by 24 s and at 1248 m from the source. Clearly, enhanced variability is found for the highest plume. Large eddies do not cause mixing close to the surface, and dispersion at this level is predominantly caused by diffusive processes. Furthermore, the lowest plume exhibits higher mean concentrations, which can be attributed to the lower mean wind speed close to the ground (Fig. 3.2 a).

3.4.2 Structure of the time averaged LES plume

The Gaussian plume model is a solution to the stationary advection-diffusion equation (Seinfeld, 1986), and can be interpreted as a time average of an infinite number of plume

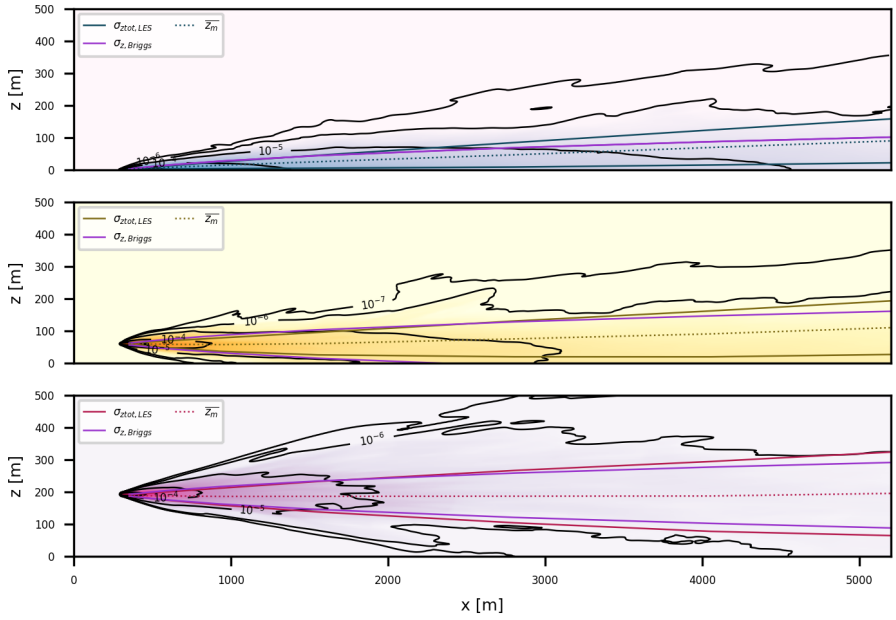

Figure 3.6: Time averaged x-z cross-section of the LES plume at (top) 0 m, (middle) 60 m and (bottom) 190 m height. The concentration fields are averaged over half an hour. The isolines are connecting the areas with the same concentration shown here in [g kg^{-1}]. Also plotted are the plume edges of the Gaussian plume (assuming Briggs diffusion coefficients) and the LES plumes. Centerlines $\overline{z_m}$ are plotted as dashed lines.

realizations. Therefore, by time averaging the LES plume over a large number of time steps, a Gaussian plume shape is expected. Figure 3.6 shows the time-averaged LES plumes in the x-z plane at the y position of the releases (y_s = 0 m). Figure 3.6 also shows the edges $\sigma_{ztot,LES}$ of the plumes and the plume centerline $\overline{z_m}$ (see section 3.3.4). For comparison, the edge of a Gaussian plume $\sigma_{z,Briggs}$ for stability class D defined by Equation 3.2 are given.

Firstly, it can be observed that mean plume centerlines behave differently depending on the release height. For the highest release height (Fig. 3.6 (bottom)) the mean plume centerline stays at the emission height irrespective of the downwind distance from the source. Conversely, the plume centerline is lifted from the surface for the source at 0 m (Fig. 3.6 (top)) and at 60 m (Fig. 3.6 (middle)). This is a consequence of the vertical velocity field that is positively skewed at the lower heights (not shown). As a result, there are large areas of slowly sinking motions with occasionally strong upward ejections lifting the mean centerline position. Secondly, the lowest plume shows clear discrepancies in the lines that outline the plume edges in the Gaussian plume model and the LES. The Gaussian plume model only accounts for the effects of vertical mixing through the vertical dispersion coefficient, σ_z. Consequently, the plume centerline remains always at the emission height. Lastly, for the highest emission height, the width of the Gaussian plume and the highest LES plume only start to diverge far from the source. For the

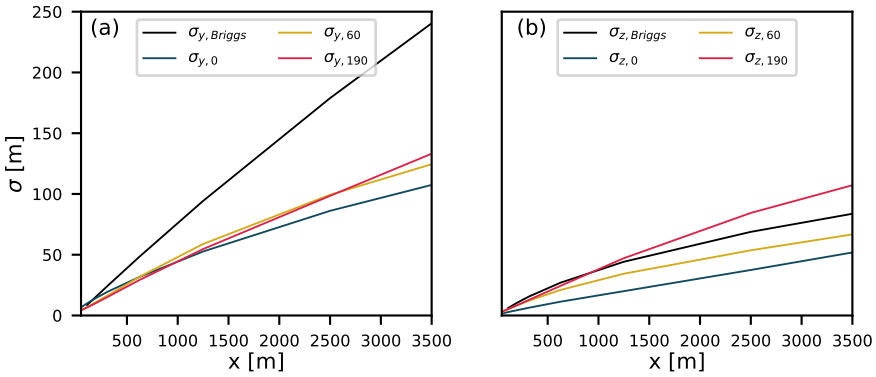

Figure 3.7: (a) Horizontal and (b) vertical plume width as a function of downwind distance from the source. Plume widths are shown for all three release heights as well as plume widths calculated using Briggs (Eq. 3.2).

Table 3.1: Coefficients of horizontal and vertical plume dispersion (Eq. 3.2) fitted for LES plumes with different source height. γ = - 0.5 remains unchanged from eq 3.2.

Source height [m]		0	60	190
σ_y	α	0.07	0.062	0.048
	β	0.001	0.001	2×10^{-4}
σ_z	α	0.017	0.043	0.049
	β	9×10^{-5}	0.001	5×10^{-4}

lower two emission heights, the differences between the plume widths are larger. This is better illustrated in Fig. 3.7 b. Here, σ_z values from Briggs and the 190 m release height are similar to approximately 1000 m downwind from the source before they start to diverge. The slower vertical dispersion of the lower two plumes is also clearly visible. LES therefore indicates that vertical dispersion coefficients should be height dependent to capture changes in the wind regime with height. In contrast, horizontal dispersion coefficients (Fig. 3.7 a) show very little variation with changing release height, but are much smaller than the Briggs Gaussian plume coefficients. The small dispersion in the y direction can be attributed to the lack of the large scale forcing in our simulation or the absence of eddies larger than the domain size (1536 m). We dictated the meandering part of dispersion in the horizontal direction (see Section 3.3.3).

To mimic the Gaussian plume growth in both directions with Eq. 3.2, Table 3.1 gives the optimized coefficients that lead to a match with the LES plumes. These coefficients will be used in Section 3.4.3 to compare to the dispersion coefficients from the look-up tables used in the OTM33a method.

Now we move on to use the LES results to evaluate two techniques to infer the source strength from downwind concentration measurements: OTM33A, and the Inverse Gaussian Model using drive-by's.

3.4.3 OTM33A

In order to obtain Gaussian profiles of mean concentrations (see Fig. 3.1), we followed the sampling procedure described in Section 3.3.3 to mimic plume meandering. Source strength estimates using the OTM33A method at 4 different distances from the source (x = [48, 108, 152, 200] m) are shown in Fig. 3.8. The tracer concentrations were recorded over 20 min (1200 data points). To obtain measurement ensembles, the sampling was repeated 20 times, as described in Section 3.3.3.

The most striking result is that for nearly all emission heights the OTM33A method overestimates the source strength. Uncertainties generally increase slightly with increasing distance from the source. Only for the 190 m source the estimated source strength at the downwind distance of 48 m is close to the true source strength. We found that this effect is caused by the way we introduce the source in the atmosphere. Instead of emitting the tracer as a point source, we use a Gaussian distribution to pre-disperse the source (see sections 3.3.1 and 3.3.2). In combination with the implemented meandering (section 3.3.3), sampling close to the source coincidentally leads to plume dispersion similar to the dispersion of the OTM33A imposed Gaussian plume. Following this, we expect the different source size to have a different effect on the source strength estimation on distances very close to source. In future studies, it is recommended to quantify the effect of the prescribed source size on the source estimation using OTM33a.

Further away from the source and with lower emission heights, a general overestimation is found. The estimated source strengths using the OTM33A method depends linearly on the dispersion parameters (Eq. 3.3). Consequently, too large dispersion parameters automatically lead to overestimated source strengths. The dispersion parameters used here were taken from the recommended look-up table (U.S. EPA, 2014). These values are based on the Pasquill-Gifford dispersion curves, just like the Briggs coefficients. As we have shown above (Fig. 3.7 a), these values are too large in the y direction compared to our LES dispersion calculation, explaining the overestimates. We have also shown that dispersion parameters in the z direction depend on the height of the source. While the differences in the z direction are not so pronounced, especially for the highest source (Fig. 3.7 b), they also contribute to the error in estimates. At the closest distance from the source, the estimates for the two lower sources have larger errors compared to the highest source. There are several causes for this. Firstly, as previously discussed, the vertical dispersion coefficient for the highest plume has a better agreement with the Briggs dispersion coefficient at distances close to the source. Secondly, according to the OTM33a protocol, the concentrations should be recorded at the plume centerline, which is assumed to be at emission height. However, we found that for different emission heights the instantaneous plumes centerline positions behave differently. Figure 3.9 shows the pdfs of instantaneous plume centerline positions relative to the y and z position of the source (y_s, z_s). In the z-direction, the pdfs have longer

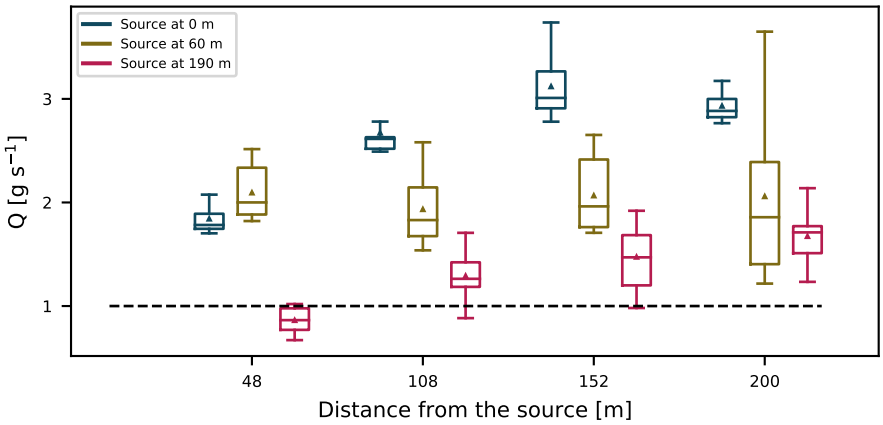

Figure 3.8: Estimates of the source strength using the OTM33a method for the emission heights 190 m, 60 m and 0 m at four different distances. Boxes show the interquartile range, while the whiskers span from 5 to 95 percentile of the data and show the mean and median. The dashed line refers to the true source strength used in the LES.

tails for values above the emission height (positive skewness). In contrast, the lowest plume lifts off the ground with distance from the source. With downwind distance, the displacements from the emission height grow as do the errors in the source strength estimates. In the y direction, the highest and the lowest plumes have slightly positively skewed pdfs relative to the emission point. The skewness in the middle plume is even more pronounced. This, in combination with the plumes still being very narrow, results in plumes being sampled at their edges, which leads to high estimation errors. The error also depends on the distance from the source as the height of the plume median is not constant. Further downwind this effect is less pronounced since the plumes get wider and sampling slightly out of the plumes median position still characterises the plume well.

Next, we study the influence of the averaging time on the source estimation. In Fig. 3.10 we show source estimates for six different averaging times at four sampling distances. The estimates for all emission heights show similar behaviour. Averaging for 20 minutes leads to smaller estimation errors for all three sources. Convergence of the error becomes slower with increasing distance from the source for the two higher sources. The lowest source had a small estimation error even for short averaging times on most downwind distances. From Fig. 3.5 it is visible that the lowest plume shows little variability even when measured much further from source (1248 m on Fig. 3.5) than the OTM33a method suggests.

Lower variability in estimations closer to the source can be attributed to short dispersion time. As previously mentioned, the plumes dispersion is a combination of relative dispersion around the instantaneous center of mass and the meandering motions. On very short distances from the source the plume will retain the initial source shape until

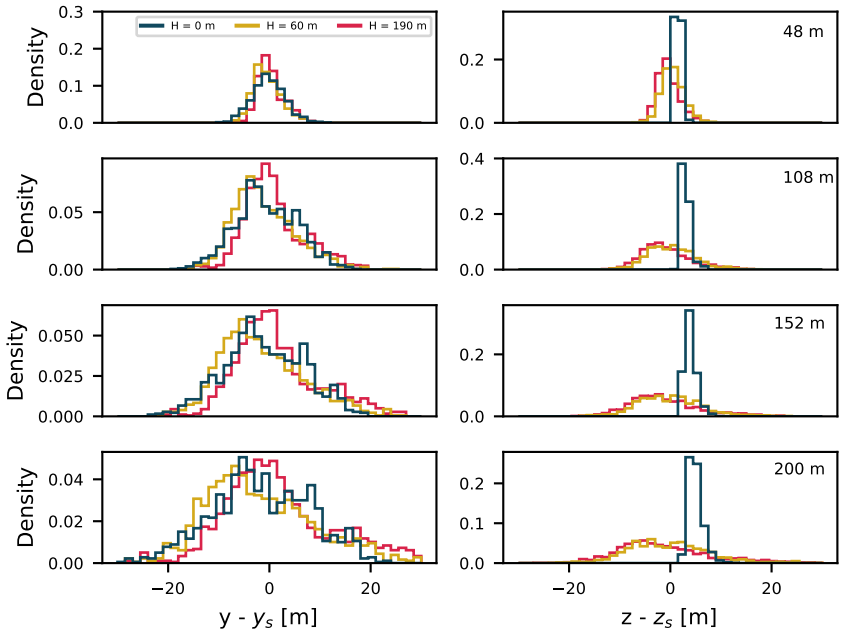

Figure 3.9: Probability density functions of the instantaneous plume centerline positions with respect to the plume emission positions (blue: 0 m, yellow: 60 m, pink: 190 m) in the y (left column) and z (right column) directions. Bins of 1.5 m were used.

it gets sufficiently mixed by the relative motions. Even with the added meandering that we implement (see Section 3.3.3, Fig. 3.1), the sampled plume resembles the shape of the source. Consequently, until the plume gets sufficiently mixed by smaller eddies, the variability between OTM33a experiments used to produce the box-plots on Fig. 3.10 is not large. The increase in uncertainty with distance is related to the increase of the plume size.

Structure of the plume close to the source

To study the structure of the plumes close to the source, we analyze the plume statistics following the approach described in Section 3.3.4. To that end, we investigate the two processes responsible for plume dispersion (mixing and meandering) separately. The effect of turbulent mixing on the plume (σ_{mix}, as defined in section 3.3.4, eq. 3.9) is isolated by averaging the 3600 plumes after aligning them according to their (displaced) center of mass in y and z directions. Figure 3.11 shows these time averaged plumes, both aligned and non-aligned (meandering included) in the y direction at four distances from the source for the largest emission height. The figure also depicts Gaussian functions fitted to the aligned and non-aligned plumes, calculated according to Eqs. 3.9 (σ_{mix}) and 3.10, respectively. For reference, also the recommended OTM33A Gaussian dispersion is plotted.

In general, the non-aligned Gaussian functions are wider due to the meandering effect

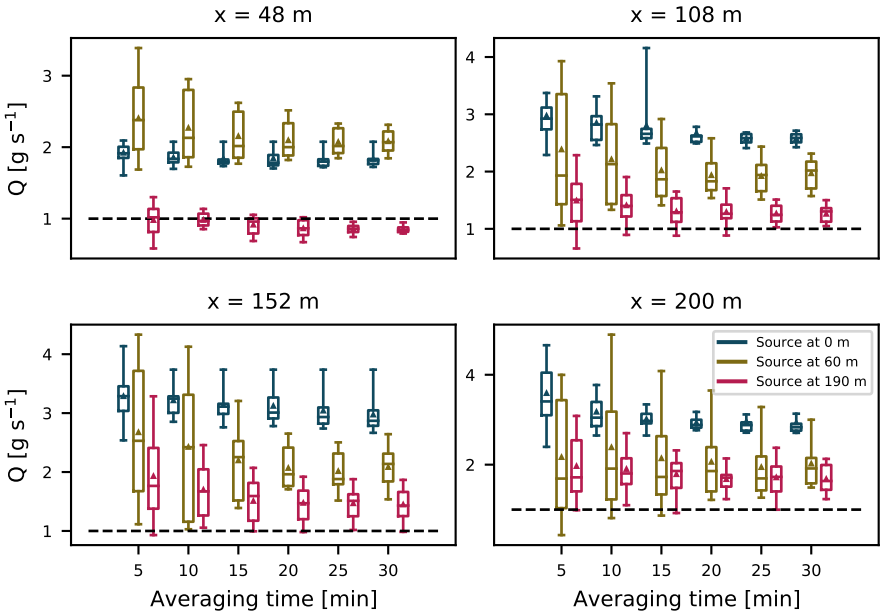

Figure 3.10: Source estimation using OTM33a method for 4 different distances from the source and for different averaging times. Boxes show the interquartile range, while the whiskers span from 5 to 95 percentile of the data and show the mean and median. The dashed lines refer to the true source strength used in the LES.

of the larger eddies that has been implemented (Eq. 3.9, $\sigma_{meander}$). As before, we find that the OTM33A dispersion coefficients are significantly larger than the time-averaged plumes. For the closest transect at 48 m, the tails of the non-aligned plume are very short and very similar to the aligned plume. This supports the observation that close to the source the plume is still very narrow and is not moved much by the larger sized eddies or dispersed around its centerline by the smaller ones. The shape of the plume at 48 m is determined by the shape of the sources (section 3.3.1). Further downwind the difference between the aligned and non-aligned plumes grows, which indicates that the plume is being moved around significantly by larger eddies. At 200 m from the source, the aligned plume is still compact, which indicates that dispersion by small eddies is a slow process. The same behavior can be observed for the z direction (not shown). The values of the derived dispersion coefficients are given in Table 3.2.

We tested the OTM33a method with the dispersion coefficients derived from the LES. Understandably, the source estimates improve largely compared to OTM33A method, but we still find estimation errors up to ≈ 40 % (not shown). We argue that these errors are caused by the vertical displacement of the plume during transport (see Fig. 3.6). As previously mentioned, one of the assumptions of the OTM33a method is that the measurements are taken at the emission height. However, very close to the source the mean plume position, emission height, and the mode of the instantaneous plume positions do not necessarily coincide (Fig. 3.9). This is a likely consequence of the skewed vertical

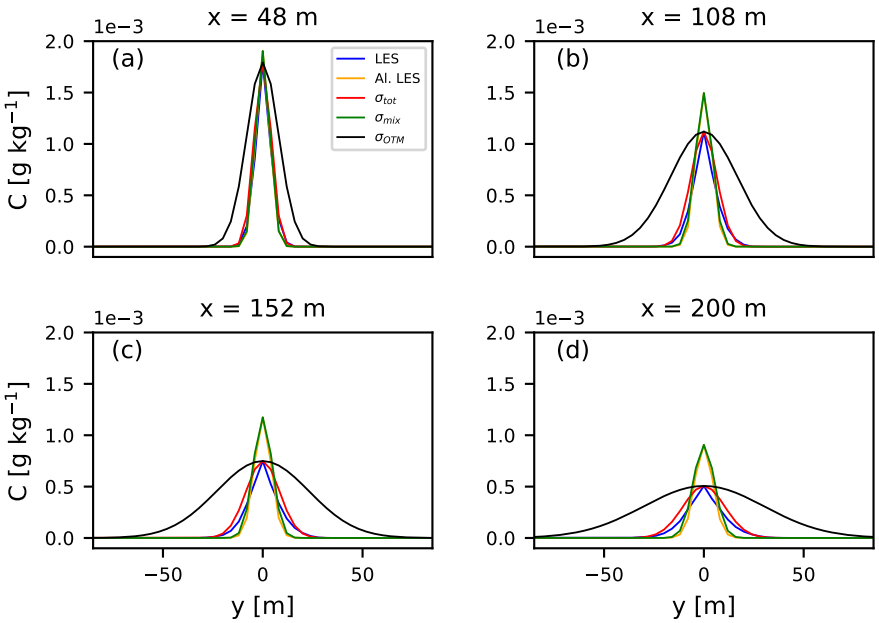

Figure 3.11: Time averages of instantaneous plumes (blue) on the plume centerline and the instantaneous plumes aligned according to their centers of mass (orange), in the y direction. Fitted through them are Gaussian functions with one standard deviation of their width σ_i [m] (green: mixing; red: total). For reference, we show Gaussian functions fitted to the maximum of the non-aligned plume with σ taken from OTM33A (black). Emission and sampling heights were 190 m.

Table 3.2: Dispersion coefficients σ (in m), obtained by using the definitions presented in section 3.3.4, for the plume emitted at 190 m.

Distance [m]	$\sigma_{y,tot}$	$\sigma_{y,mix}$	$\sigma_{y,meand}$	$\sigma_{z,tot}$	$\sigma_{z,mix}$	$\sigma_{z,meand}$
48	4.56	3.62	2.78	2.90	1.83	2.25
108	7.63	4.68	6.02	5.60	3.06	4.69
152	10.01	5.54	8.34	7.50	4.02	6.33
200	12.65	6.56	10.80	9.44	5.08	7.69

velocity field discussed previously in section 3.4.2. On top of that, we found that the pdf of the instantaneous plume positions is also slightly skewed in the y direction (Fig. 3.9), which contributes to the overall error.

In conclusion, we find that the errors associated with the OTM33A method are sizeable. One source of errors is associated with the assumed dispersion coefficients, which were found to be too large compared to LES. Other sources of errors are related to assumptions made in the Gaussian plume model.

3.4.4 Source strength estimation from car measurements

Now we move to the analysis to more dispersed plumes that are sampled further away from the source ($>$ 200 m). Figure 3.12 shows results of car measurements taken perpendicular to the mean wind and at plume emission height for all three sources. Estimates were made following the Inverse Gaussian method described in Section 3.2.3. The employed Gaussian plume model (Section 3.2.1) uses Briggs dispersion coefficients and the mean wind speed in the x direction at the height of the release. Estimates are shown for transects taken by an infinitely fast car. The transects are taken according to the sampling procedure described in Section (3.3.3). If only one transect is made, the estimated source strength shows a large spread for all distances, with estimates being up to 4 times larger than the real source strength. The medians show a negative bias indicating that a large fraction of the plumes has relatively low concentrations, and a few plumes exhibit (very) large concentrations. This result is expected, since the most concentrated part of the plume is moving over a 2D (y-z) plane (e.g. Fig 3.5). The probability of sampling this part of the plume with a 1-D transect is less likely. When the source strength is calculated using averaged plumes (see Section 3.3.3), it becomes more likely to estimate the emission strength. This is due to turbulent fluctuations in the plumes being averaged out. As a result, the averaged plume becomes more Gaussian as more transects are included in the average. For instance, the spread drops by $\approx$ 50% if 10 transects are averaged. These results are in line with the findings of Caulton et al. (2018), who proposed averaging over at least 10 transects. As opposed to the estimations from the higher two plumes, the estimations from the lowest plume exhibit very little variability. As we have discussed in

relation to Fig. 3.5, large eddies do reach the surface but merely displace the plume, and plume dispersion at this level is predominantly caused by small eddies processes.

In contrast to the OTM33A method, the estimated source strengths converge to the true value with sufficient averaging time using car transects. This is due to the fact that car transect method calculates the mass flux of the tracer by integrating over the (assumed) Gaussian profile. The flux of the mass through any given y-z plane in both models is conserved and equal, irrespective of the width of the actual plumes. Note here that the LES plume in our analysis is still much narrower in the y direction compared to the Gaussian plume. In the vertical direction, the LES plume width is comparable to the Gaussian (Fig. 3.7). If this would not be the case, the analysis would give incorrect source estimates, since a different displacement of mass in the vertical would lead to a different horizontal line integral.

It can be seen that the estimations, depending on their distance from source, converge to a slightly different value than the true source strength. This can be related to the position of the plume centerline and the plume mode discussed in sections 3.4.2 and 3.4.3. For the LES plumes the position of the mode varies with the distance from the source while in the Gaussian plume model the plume centerline does not diverge from the emission height. This mismatch in the two models effectively means that two plumes with different emission heights are being compared. When the emission height in the Gaussian plume model is adjusted to match the height of the LES plume mode for a certain downwind distance, the estimation error disappears.

Lastly, we have repeated the analysis of source strength estimations sampled outside of the plume centerline (not shown). Notably, the closer the plume is sampled to its edge, the more transects are needed for the estimates to converge to the true value. This was an expected result since at its edge the plume shows greatest variability as shown in previous studies (e.g. Dosio & de Arellano (2006); Gailis et al. (2007); Ardeshiri et al. (2020)).

To study the convergence of the results, Fig. 3.13 shows standard deviations of the source strength estimation for the plume emitted at 190 m. The standard deviations are shown for the first 40 plumes at 8 different distances from the source. After ≈ 10 transects, the standard deviation decays with the inverse square root of the number of averaged plumes. This confirms that all transects through the plume are independent, and that the time difference between the samples was not too short. We also studied the influence of driving speed through the plume for cars driving slow (4 m s^{-1}) and fast (12 m s^{-1}) but have found no significant difference in results from transects taken by infinitely fast cars.

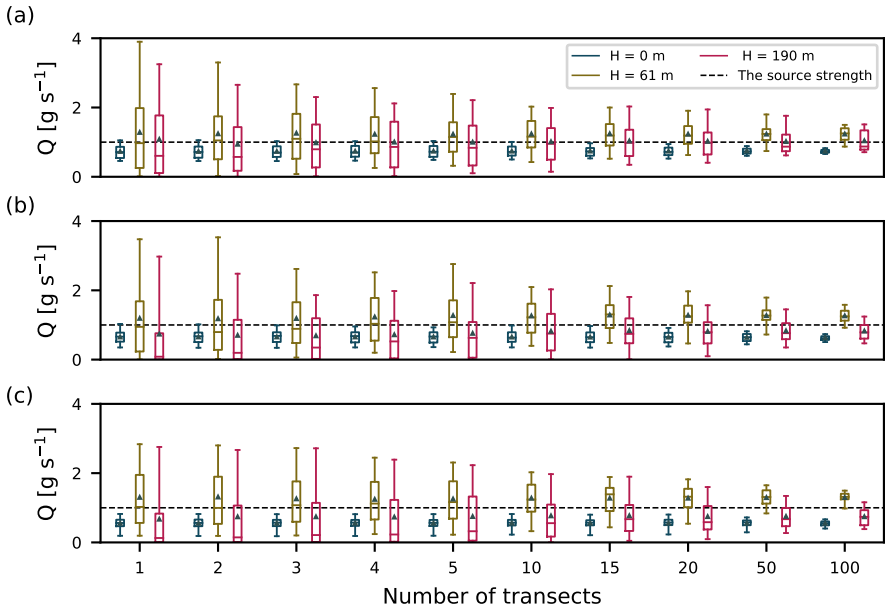

Figure 3.12: Estimates of the source strength from instantaneous plume transects for all three emission heights. Boxes show the interquartile range, while the whiskers span from 5 to 95 percentile of the data and show the mean and median. Distances from the source are (a) 200 m, (b) 624 m, (c) 1248 m.

3.5 Discussion and conclusion

In this study, we performed a large eddy simulation (LES) of point source plumes released into a neutrally stable, homogeneous and statistically stationary turbulent flow over a flat terrain. Simulations were performed following the laboratory experiment by Nironi et al. (2015) of point-source plume dispersion in a turbulent channel flow. Point sources were placed at three altitudes z = [0, 60, 190] m. We sampled our numerical plumes according to two measurement protocols that aim to estimate point source strengths with the aid of the Gaussian plume formalism. The aim was to quantify the uncertainties of the drive-through and OTM33a methods.

We found that the time-averaged LES plume has a Gaussian shape, but that the dispersion rate of the plume in the y direction is slower compared to a Gaussian plume with the Briggs dispersion coefficients representative of a neutral boundary layer (e.g. Griffiths (1994)). One of the reasons why our y-dispersion is smaller might be the lack of large scale variability in our simulation, which is instead forced by a constant gradient pressure force. In the vertical, the discrepancies between the Briggs coefficients and the LES plumes were less pronounced. However, for smaller release heights, the mean plume centerline is displaced in the vertical, a feature that is not captured in the standard Gaussian plume dispersion coefficients. The rise of the plume centerline downwind from the source is caused by the nature of the boundary layer turbulence, which has large areas of slow

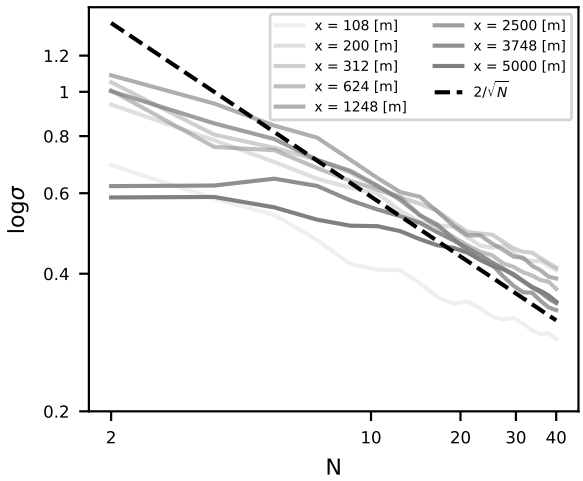

Figure 3.13: Standard deviation of the source strength estimates with increasing sample size for eight different distances from the source. The emission and sampling heights were 190 m.

sinking motions, and small areas with stronger upward motions.

Application of the OTM33A method to our simulated plumes showed that we tend to overestimate the source strength by ≈ 50 - 200 %. Previous studies (Edie et al., 2020) showed a two-σ uncertainty in the source strength of ± 70 %, but without a bias. The significant overestimation in our results is a direct consequence of the OTM33A formalism in which the derived source strength depends linearly on the dispersion coefficients. Coefficients based on Pasquill-Gifford dispersion curves (U.S. EPA (2014), e.g. Seinfeld (1986)) and Briggs coefficients (Griffiths, 1994) are both too dispersive compared to the LES simulation.

By aligning and averaging the plumes according to their center of mass we were able to show that, at distances smaller than ∼150 m from the source, the plume shows a shape similar to the source shape, i.e. a very narrow Gaussian. The aligned and non-aligned plumes are similar indicating that the plume is moved very little from its center of mass by larger eddies (meandering) even though OTM33A accounts for that. From Fig. 3.3 this is most obvious for the plume at 48 m. Further downwind the height of the aligned plume peak gets smaller indicating the dispersion in the z direction also plays an important role. Nevertheless, if the dispersion coefficients derived for the individual LES plumes are used in combination with the OTM33a method, significantly smaller errors are found. Another source of the errors in the OTM33a method is the position of the plume in relation to its centerline. The method assumes that the plume centerline position, emission height and the mode of the centerline position coincide. We were able to show that this is not necessarily true and that this mismatch leads to additional uncertainties in the source estimation.

We also simulated drive-by's at distances up to 1248 m from the source. The plumes were sampled simulating different car speeds with a sampling frequency of 1 Hz to mimic realistic field conditions. We used the Inverse Gaussian Model (IGM) method to derive the source strength, with the mean wind taken from the LES at release height and using Briggs dispersion coefficients. We found that the correct source strength is estimated if the result is averaged over sufficient different realisations. To estimate the source strength within $\approx 40\%$, we recommend to average over at least 15 drive-by's. This supports the findings from Caulton et al. (2018) who recommended at least 10 transects. Our results show no significant influence of the driving speed on the source strength estimation. The IGM method is insensitive to errors in y-dispersion, because the method depends on the line integral in the y-direction. We found, however, that a mismatch between the vertical centerline position of the plume and the emission height does produce an error in the source estimation. This error can be corrected by adjusting the height of the Gaussian plume to match the simulated plume centerline.

The plumes studied here were emitted into the neutral channel flow as this is the most canonical case of the atmospheric turbulence. Similar study should be performed for unstable and stable conditions. Based on our findings, we expect additional variance of the plume under unstable conditions because of buoyancy effects producing additional turbulence. Conversely, for a stable atmosphere, we expect that a shorter averaging time (less plume transects) would be needed to achieve 40 % accuracy.

Our study has shown some of the advantages and drawbacks of two commonly used measurement techniques for source strength estimations. To arrive at our conclusions, we used the neutral channel flow experiment that resembles the purely shear driven turbulence in an atmospheric surface layer. In this setting, the possible errors in the estimations are expected to be minimized since the turbulence is well understood and the Gaussian plume model is logically derived. A next step would be to repeat this study for different stability conditions in a idealized setting such as this, as for example the LES experiment preformed by Xiao et al. (2021) of plume dispersion in stable boundary layer, or to re-create real field conditions (Ražnjević et al., 2022). With constantly improving numerical techniques, LES is capable of reproducing real meteorological conditions encountered in the field. Combined with the improving observational techniques, this approach is expected to lead to better estimates of source strengths.

3.6 Plume sampling procedure to mimic large-scale induced plume meandering

Here we describe the plume sampling procedure used to mimic the large-scale plume meandering necessary for the OTM33a method.

If we define 0 as the left edge of the plume and 1 as the right edge, we can define a

function of time, ζ, that oscillates between 0 and 1 with an uniform step, essentially mimicking forward and backward motions through the plume. In order to achieve denser sampling around the centerline, we re-define our sampling function in a way that gives us the relative position between -0.5 and 0.5, $\widehat{y}_i$, as:

$$\widehat{y}_i = \zeta_i + A(\tfrac{1}{2} - \zeta_i)(1 - \zeta_i)\zeta_i - \tfrac{1}{2}. \tag{3.14}$$

Where $\widehat{y}_i$ is the grid point at which the sample was taken at the timestep i. Factor A determines the density of the sampling points around the centerline, and we have set it to $A = 3$. We can then convert this array into dimensional units to find the position, Y_i, at which the sample is taken, by adapting the relative position, $\widehat{y}_i$, to the actual plume width L as is shown in Eq. 3.15

$$Y_i = L\widehat{y}_i. \tag{3.15}$$

The acquired sampling pattern for two distances from the source is shown in section 3.3.3, Fig. 3.1a. We applied the sampling strategy at x = [48, 108, 152, 200] m from the source. With the assumed $\theta = 15°$, the width over which plumes were sampled was L = [21, 37, 49, 62] m for each of the distances from source respectively.

Chapter 4

Interpretation of field observations of point-source methane plume using observation-driven large-eddy simulations

This chapter is based on: Ražnjević, van Heerwaarden, C., van Stratum, B., Hensen, A., Velzeboer, I., van den Bulk, P., & Krol, M.: Interpretation of field observations of point-source methane plume using observation driven large-eddy simulations, Atmospheric Chemistry and Physics, 22(10), 6489-6505, https://doi.org/10.5194/acp-22-6489-2022, 2022.

Abstract

This study demonstrates the ability of large-eddy simulation (LES) forced by a large-scale model to reproduce plume dispersion in an actual field campaign. Our aim is to bring together field observations taken under non-ideal conditions and LES to show that this combination can help to derive point source strengths from sparse observations. We prepared a one-day case study based on data collected near an oil well during the ROMEO campaign (ROmanian Methane Emissions from Oil and gas) that took place in October 2019. We set up our LES using boundary conditions derived from the meteorological reanalysis ERA5 and released a point source in line with the configuration in the field. The weather conditions produced by the LES show close agreement with field observations, although the observed wind field showed complex features due to the absence of synoptic forcing. In order to align the plume direction with field observations, we created a second simulation experiment with manipulated wind fields. The estimated source strengths using the LES plume agrees well with the emitted artificial tracer gas plume, indicating the suitability of LES to infer source strengths from observations under complex conditions. To further harvest the added value of LES, higher order statistical moments of the simulated plume were analysed. Here, we found good agreement with plumes from previous LES and laboratory experiments in channel flows. We derived a length scale of plume mixing from the boundary layer height, the mean wind speed and convective velocity scale. It was demonstrated that this length scale represents the distance from the source at which the predominant plume behaviour transfers from meandering dispersion to relative dispersion.

4.1 Introduction

The reduction of greenhouse gases (GHG) emissions is of the highest importance in mitigation of climate change. Methane (CH_4) is one of the most potent GHGs, but due to its relatively short lifetime in the atmosphere, reduction of CH_4 emissions can have more immediate positive effects on the mitigation of climate change effects (e.g. Baker et al. (2015); Zickfield et al. (2017); Caulton et al. (2018)). Methane has large variety of sources that differ in origin (anthropogenic or natural) and size (e.g. point-like, diffuse, line). An overview of different source types and their contribution to global methane budget is given by Saunois et al. (2016).
In order to help constrain methane emissions, the Methane goes Mobile – Measurements and Modelling ($MEMO^2$) project started in 2017. The goal of the project was to improve CH_4 emission factors in inventories on European scale by combining extensive measurement campaigns of different sources of CH_4 with modelling techniques across different scales. The $MEMO^2$ consortium participated in a campaign in which methane emissions from Romanian oil and gas industry (ROMEO) were sampled. The campaign took place during October 2019. Sources of methane were measured on basin and well scales employing various measurement techniques.
With methane often being released from small but strong sources in a turbulent atmosphere, the observation of plumes is challenging. A large variety of measurement techniques have been developed for identification and quantification of GHG sources, ranging from satellite based observations (e.g. Bergamaschi et al. (2007); Jacob et al. (2016)) and basin-scale measurements using aircraft (Conley et al., 2017) to local source measurement techniques. These local techniques include, among others, instruments placed on unmanned aerial vehicles (UAVs) (e.g. Andersen et al. (2018); Shah et al. (2019)), instruments placed on ground vehicles (e.g. Hensen et al. (2006); Baillie et al. (2019)) and point measurements from sensors mounted on towers (Röckmann et al., 2016). Each of these techniques has its own strengths, either being highly accurate in time or covering large spatial areas, but neither does both. Dispersion models provide insight into the behavior of plumes and can help with the data interpretation and planning of measurement strategies. These models vary greatly in their complexity and underlying assumptions. Most commonly, Gaussian plume models are combined with observations to quantify sources (Caulton et al., 2018; Edie et al., 2020; Rybchuk et al., 2020). These simple models are fast and easy to use but come with restrictive assumptions (e.g. stationarity of the plume and the mean wind) that make their application challenging under the strongly transient conditions that often characterize the local atmospheric boundary. With the development in computer power in the past decades, high resolution models that are able to simultaneously resolve the turbulent velocity field and describe the transport of emitted tracers, large eddy simulations (LES), have been increasingly used for plume studies (Cassiani et al., 2020). LES explicitly resolve the largest eddies, which carry most of the energy, and parameterize the smallest

scales using subgrid-scale models (e.g.Deardorff (1973); Pope (2000)). LES have been utilized in many dispersion studies, mostly focusing on idealized channel flows in various stability regimes (e.g. Dosio & de Arellano (2006); Boppana et al. (2012); Ardeshiri et al. (2020)). LES have been successfully validated (e.g. Dosio & de Arellano (2006); Ardeshiri et al. (2020)) against a considerable amount of extensive laboratory dispersion studies. These dispersion studies include channel flows in either water or air (e.g. Fackrell & Robins, (1982a,b); Gailis et al. (2007); Nironi et al. (2015)). One of the main advantages of LES in dispersion studies is that it provides a high temporal and spatial resolution of the 3D plume. This enables detailed analysis of the plume statistics, something which is difficult to do only from observations. Furthermore, LES can be used as a laboratory for optimizing measurement strategies. Despite the vast amount of idealized studies, the performance of LES has not been validated against many experimental field studies. (Steinfeld et al., 2008; Ardeshiri et al., 2020; Rybchuk et al., 2020). For instance, the Prairie Grass experiment (Barad, 1958) still serves as a common reference for LES studies. More recently, Caulton et al. (2018) evaluated the performance of the Gaussian plume model against measurements in a neutral atmosphere and LES while Rybchuk et al. (2020) evaluated WRF LES with Prairie Grass experiment for convective conditions.

In this study, we aim to bring together actual field observations under less than ideal conditions with LES. The ROMEO campaign focuses on sampling methane from spatially distributed sources covering a large area using the mobile measurement techniques. While this approach is very useful in detecting unknown sources, measurements of individual, isolated plumes are often sparse. This is due to the measurement techniques employed. For example, plume transects using cars only provide observations at the surface in one dimension. Moreover, this observation strategy is limited by the conditions in the field (accessibility of the source, the amount of adjacent roads on which measurements can be taken, road conditions etc.). Here, we aim to demonstrate how LES can help in interpreting sparse observations in the field both from a viewpoint of validation and interpretation. We will present an LES dispersion study of a methane plume measured during the ROMEO campaign. The LES study is set-up combining local meteorological observations with ECMWF ERA5 (Hersbach et al., 2020). We will compare the measured plume with the LES simulated plume in order to gain insight in the information gathered through the measurement process, and to evaluate the performance of LES. Finally, we will use LES to study the structure of the simulated plume in convective conditions and its behavior by analyzing the higher order statistical moments. We will build on the idealized studies Dosio & de Arellano (2006); Cassiani et al. (2020) and apply the statistical analyses to simulations that represent realistic field conditions.

The structure of this paper is as follows: In Section 4.2 we introduce the location where the measurements took place and look at the meteorological conditions relevant for the

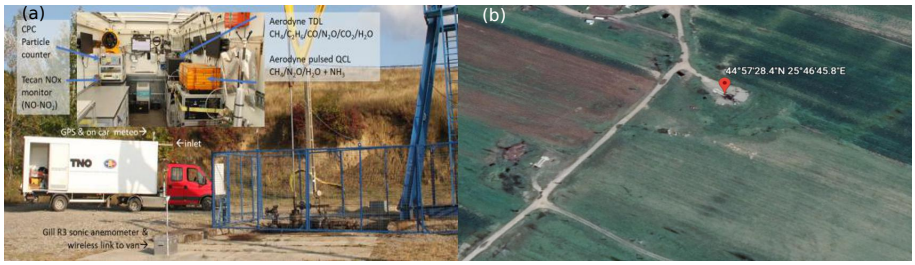

Figure 4.1: (a) (Inset figure) The measurement set-up inside the TNO vehicle. TNO vehicle used in the measurement campaign, Location of the inlet is indicated on the figure. (b) Google Earth view of the measurement site with the oil-well location pointed out.

plume dispersion. Following this, in Section 4.2.2 we present available data from the campaign as well as the methods and instruments employed in the field. In Section 4.3 we present the numerical model used to perform the LES, the simulation set-up and forcing used to reproduce the meteorological conditions. In this section we will also outline the statistical methods used to inspect the simulated plume behavior. In Section 4.4 we evaluate the LES plume with observation and discuss the characteristics of both plumes. This is followed by a more in-depth analysis of the simulated plume at various distances from the source. Finally, in Section 4.5 we evaluate the usability of LES for dispersion studies under realistic meteorological conditions.

4.2 Case description

4.2.1 Site description and meteorological conditions

The case study presented here is based on measurements performed by a team from the Netherlands Organisation for Applied Scientific Research (TNO) during the ROMEO campaign in Romania. The measurements were taken in the Parhova County of the oil well 1474 in Darmanesti. The county is located in the region between the Transylvanian Alps and Bucharest, which is characterized by plains in the South and the Carpathian mountains in the North. The actual site is located in the central part of the county, where the two distinct landscapes meet. The measurements were performed on the road downwind from an oil well over the course of 3 h. The length of the road segment on which the plume was measured was 150 m, while the distance from the middle of road to the well was 78 m. The measured well and the adjacent road on which measurements were performed is shown on Fig. 4.1 (b) and the vehicle with which the measurements were performed is shown on 4.1 (a).

The measurements were performed in the afternoon (14.30 - 17.30 LT (UTC + 3h)) on 17 October 2019. The weather at the location was characterized by very low winds and

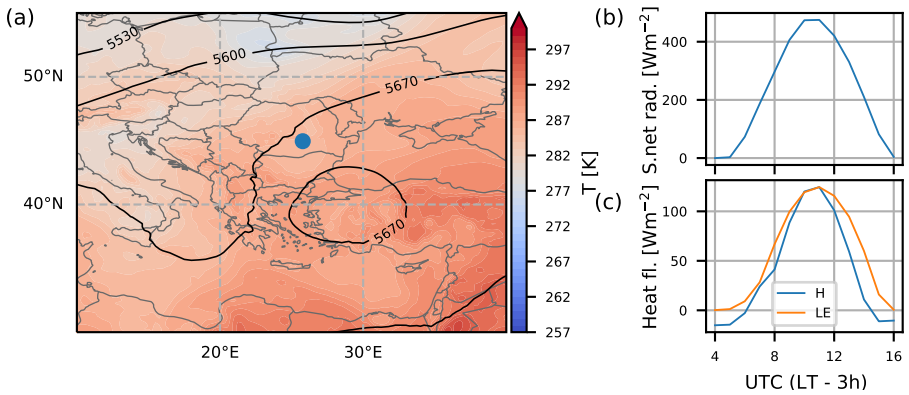

Figure 4.2: Meteorological situation over SE Europe on 17th October 2019. (a) Geopotential height (m) at the 500 hPa pressure level and temperature at 850 hPa at 12 UTC. Location of the studied region is indicated on the map by a blue circle. (b) Surface net solar radiation, (c) hourly values of sensible an latent heat at the location of the measurements.

no cloud cover, as confirmed by the participants of the campaign. To analyse the overall synoptic situation over Europe and Romania in particular, we used the geopotential height and temperature chart obtained from ERA5 (Hersbach et al., 2020). The weather over Romania was characterized by very low gradients in both temperature and pressure (Fig. 4.2 a), resulting in low wind speeds and advection during the campaign. Hence, we expect that the conditions were strongly influenced by local convection.

The Figure 4.2 shows the surface net solar radiation and the sensible and latent heat fluxes in the region (panels (b) and (c) respectively) retrieved from the ERA5 data. The surface heat fluxes are comparable indicating dry conditions (Fig. 4.2 b), and the solar radiation indicates no clouds were present. Furthermore, it was inferred from the ERA5 data that the temperature maximum at the surface was 22°C and the boundary layer (BL) depth reached 700 m at 12 UTC (not shown). The ERA5 height wind profiles show wind turning with height. Maxima in wind speeds in opposite direction from those at the ground were seen at approximately 1000 m height, or just above the BL top. For the duration of the measurements, the mean horizontal wind at the surface showed variation of 10° (not shown).
As will be presented later in Figure 4.3, we find that, for the duration of the measurements, the temperature at 1000 hPa level remained almost constant, and showed almost linear decrease with height. Similarly, the specific humidity showed peak values at the surface and constant values in the mixing layer above it. Above the BL, specific humidity decreased with height. The near constant in time height profiles of specific humidity and temperature confirm that the contribution of large scale advection was negligible during the campaign. As a result, the time evolution of temperature and humidity was determined by local processes. This leads to a complex pattern in vertical baroclinicity, which is a challenge for both collecting experimental data and simulation studies.

4.2.2 Measurement instruments and available data

The measurement device used was a dual laser trace gas monitor based on Tunable Infrared Laser Direct Absorption Spectroscopy (TILDAS; Aerodyne Research Inc., Billerica, US) that measures methane and ethane (CH_4 and C_2H_6) simultaneously. The ethane data is used to discriminate methane plumes originating from fossil fuel related sources (which contain ethane) and agricultural or biomass degradation methane emissions. The instrument also measures H_2O, CO_2, CO and N_2O. The molar fraction levels for these components are measured at sub-ppb resolution with 1 measurement per second (1 Hz). Concentration levels were calibrated versus working standards for CH_4 (B20 flasks with compressed air at 2800 and 5000 ppb) that are linked to the Integrated Carbon Observation System (ICOS) & the National Oceanic and Atmospheric Administration (NOAA) standards used at the Cabauw tall tower in the Netherlands. B20 flasks are 20 L cylinders that hold 2000 L of gas at the pressure of 100 bars. Besides that, during the Romania Campaign, calibrations cylinders from Utrecht University were used, with concentrations of 6.3, 27 and 130 ppm for the higher concentration measurements. The instrument measured CH_4, C_2H_6, N_2O, CO_2 and CO simultaneously at 1 Hz with a precision of 2.4, 0.1, 386.3 and 2.5 ppb, respectively. Here, precision is reported as three times the standard deviation of six minutes constant concentration reading. The instrument was placed into a vehicle that drove along the closest road and its position was logged at 1 Hz with a GPS system. The inlet of the measurement device was placed at the top of the vehicle at a height of 3 m. A delay-time correction is applied to the data to compensate for the 1.5 second delay between the logged GPS location and actual measurement in the TILDAS instrument.
A controlled release of tracer gas N_2O was conducted simultaneously with the CH_4 measurements. N_2O was released using a critical orifice of 0.65 mm^2 at 5 bar. Before and after the release, the mass of the cylinder was determined. Release was 0.59 $\pm$ 0.02 g s$-$1

The wind speeds (u, v, w) were measured from a battery-operated Gill R3 sonic anemometer placed close to the source and at 1.8 m above ground level. The sonic data was stored at 20 Hz, and 1 Hz values were transmitted with a wireless link to the central computer in the van. For this analysis, 1 min averages of wind speeds were used.
Due to the road conditions the vehicle speed varied from transect to transect. Therefore, the measured plumes have a different number of measured points and the exact distribution of these points over the measurement transect differs. To obtain a uniform dataset, two end points were selected that encompass all plumes. Values of the vehicle location, CH_4 and N_2O data were linearly interpolated on a 250 point grid.

4.3 Numerical methods

Large-eddy simulations were performed using the MicroHH model, which is an open-source computational fluid dynamics code (van Heerwaarden et al., 2017). The code solves conservation equations of energy, momentum, and mass under the anelastic approximation. The transport of passive scalars is solved with the advection-diffusion equation. The second-order Smagorinsky model is used for the subgrid parametrization of the velocity components.

Time integration is performed using third-order accurate Runge-Kutta scheme and the spatial domain is discretized on a staggered Arakawa-C grid.

The advection term for dispersing scalar in the model is solved using a second-order energy conserving scheme. For atmospheric transport, positivity in numerical schemes plays a crucial role. By imposing positivity using a flux limiter, over- and under-shoots are avoided in areas with strong concentration gradients (Hundsdorfer et al., 1995).

A periodic boundary condition was imposed for the momentum and thermodynamic variables on the lateral boundaries of the domain. The lower boundary had no-slip ($u = v = 0$) and no penetration ($w = 0$) boundary conditions, while the upper boundary had free-slip boundary conditions, with tangential components of velocity being zero ($\frac{\partial u}{\partial z} = \frac{\partial v}{\partial z} = 0$). The inflow and outflow boundary conditions for the scalar representing CH_4 were imposed at the lateral boundaries of the domain to prevent the plume from re-entering. The boundaries were set using Neumann (right and lower boundaries) and Dirichlet (left and lower boundaries) boundary conditions which were used to interpolate values of scalars in two ghost cells outside of the domain.

In order to achieve LES that corresponds to the field conditions large scale forcings of relevant variables is imposed by coupling the LES simulations with the ERA5 data (Hersbach et al., 2020). The geostrophic wind and large scale advection terms are interpolated from the ERA5 data, while the nudging of the simulation is applied on a relevant timescale to prevent the simulation from drifting from the large-scale mean profiles while smaller scale turbulence can still develop independently. The coupling is based on Schalkwijk et al. (2015).

4.3.1 Simulation set-up

The LES was performed in a three dimensional domain of 4.8 × 4.8 × 3.085 km (x, y and z direction respectively). The domain was discretized on a 960 × 960 × 480 (x, y, z) grid. This results in uniform horizontal resolution of 5 m, while the vertical direction is resolved on a stretched grid with 2 m resolution in the first 1 km of the domain and 50 m at the top. The resolution was chosen with the computational feasibility in mind such that the grid was dense enough for the dispersion to be well represented, but still have

the domain large enough to capture the meteorological effects relevant for this study. A constant source of passive scalar was added as a two-dimensional Gaussian placed on the bottom of the domain. The Gaussian had the $1\sigma_i$ (i = x, y) value equal to size of one grid box, therefore 97% of the source was spread on 4^2 grid. It has been shown in laboratory studies of plume dispersion that the ratio of the source size and the size of larger scale eddies has significant impact on plume statistics (Fackrell & Robins,, 1982a,b; Nironi et al., 2015). To circumvent this issue, the size of the source should be larger than the size of one grid box. Recently, Ardeshiri et al. (2020) investigated the influence of resolution on the flow and plume statistics in LES. They have shown that the scalar variances converge for the sources resolved by at least 4^3 grid nodes. We have placed the source in the top right corner of the domain at the position (3600, 3600) m, where the domain origin is defined at the lower left corner. The scalar was emitted with constant flux of 1 g s^{-1}.

In order to reproduce meteorological conditions in the fields encountered on the measurement day, the simulation was nudged according to height profiles of horizontal wind speed, temperature and specific humidity obtained from the ERA5 data. Large scale forcing was imposed through geostrophic wind with the Coriolis parameter for this latitude being $f_C = 1.0305 \cdot 10^{-4}$ s^{-1}. Furthermore, roughness lengths of $z_{0h} = 0.001$ m and $z_{0m} = 0.05$ m were imposed on the lower boundary for scalar and momentum respectively.

The simulation was run for 7.5 hrs in total. A spin-up time was imposed to have the boundary layer fully developed and resembling field conditions as closely as possible. First, the fields from ERA5 were initiated at 7 AM UTC and the simulation was started with an integration time step of 6 s. The simulation was run for 7.5 hrs with vertical profiles being nudged towards ERA5 profiles every hour. At 11 UTC, the source was activated in the simulation. The instantaneous plume concentrations c, wind components u, v and w and liquid potential temperature θ_l were recorded on various two-dimensional cross-sections of the domain.

The mean wind in this simulation shows fluctuating behavior, which influences the direction of the plume dispersion. Here, we assume that the local wind that influenced the dispersion was governed by local influences that are not captured in ERA5. To be able to still compare the plume at different simulation times, the mean wind speed between observations and simulation should be aligned. Therefore, we performed another simulation in which the mean wind was directed along the x axis, while keeping all the other specifics, apart from the source location, identical. These two simulations will be further on referred to as *realistic* and *idealized* for the first and second simulation, respectively. The overview of the specifics of the two simulations are given in Table 4.1. Note that in the idealized simulation, the nudging profiles for potential temperature and

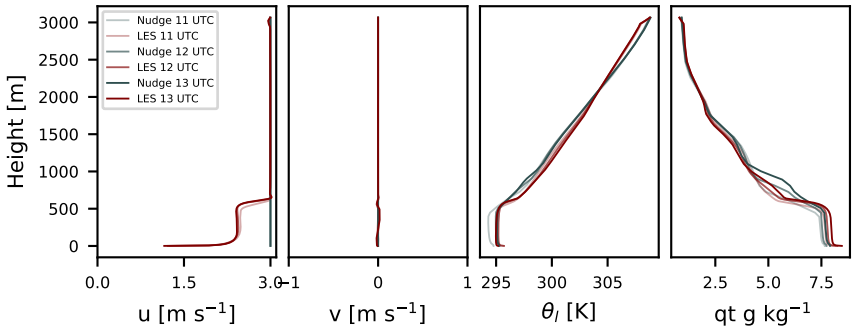

Figure 4.3: The nudging height profiles and the hourly mean height profiles of variables from the simulation with centered mean horizontal wind direction.

specific humidity still originate from the ERA5 dataset. For the wind, however, we set the height profile of the v component in the nudging profiles to zero and set the u profile to a constant value of 3 m s^{-1}. This wind speed was chosen through manual tuning to get a good match with the measured wind speed at 2 m height. In this way the wind direction was kept constant without loosing the general characteristics of the realistically simulated boundary layer.

4.3.2 Estimation of the unknown emission rate

Source quantification from one-dimensional transect measurements is often performed using a mass balance approach. This method compares the total line-integrated flux of the time averaged plume from an unknown source with the flux from a known source under the same atmospheric conditions and at the same downwind distance from the source. This method has been used in conjunction with either a tracer release, or - if no tracer is co-emitted - with simple plume transport models such as the Gaussian plume model (e.g. Caulton et al. (2018)). The equation used for this approach reads:

$$Q_{estim} = \frac{\sum_y C_{meas}\overline{u_{meas}}}{\sum_y C_{ref}\overline{u_{ref}}} \times Q_{ref}. \tag{4.1}$$

Here the Q_{estim} is the emission rate of the unknown source in g s^{-1}, C g kg^{-1} and $\overline{u}$ m s^{-1} denote the time-averaged measurements and the mean wind speed, respectively. Subscripts ref and $meas$ refer to the reference tracer with known source Q_{ref} and measured tracer, respectively. Note that the reference plume can be either measured of inferred from a model.

4.3.3 Statistical properties of the modeled plume

Finally, we present a short overview of the statistical moments calculated for the simulated plumes that will be discussed in Sections 4.4.2 – 4.4.2. Higher order statistics can provide

Table 4.1: The specifics of the two performed simulations. First row shows set-up of the simulation with highly turning mean wind and the second the set-up of the simulation with the mean along the x axis.

Simulation	Domain size (km)	Resolution	Source position (m)	Geostrophic wind	Tendencies: u and v	Tendencies: θ_l and q_t
Realistic	$4.8 \times 4.8 \times 3.085$	$960 \times 960 \times 480$	(3600, 3600, 0)	On	On	On
Idealized	$4.8 \times 4.8 \times 3.085$	$960 \times 960 \times 480$	(480, 2400, 0)	Off	Off	On

further insight into the behavior of the measured plume but are often unattainable from the measurements due to insufficient spatial and temporal resolution. Figure 4.4 shows a scheme of an idealized plume emitted from a ground point source. Let z be the vertical position of a particle in an instantaneous plume at a distance x from the source. This plume is characterized by its centerline position z_m defined as its center of mass:

$$z_m(x,t) = \frac{\int c(x,y,z,t)\, z\, dz\, dy}{\int c(x,y,z,t)\, dz\, dy}. \tag{4.2}$$

An ensemble of such instantaneous plumes will have its own centerline position $\overline{z_m}$ defined as the mean over all the realizations. Now the fluctuations of the instantaneous plume around these mean positions can be defined. The absolute fluctuation z' is the displacement of the particle in the plume from the mean centerline position $\overline{z_m}$, relative fluctuation z'_r is the displacement from the instantaneous plume centerline z_m and the fluctuation of the instantaneous plume centerline z'_m is the displacement from the mean position $\overline{z_m}$. These can be written as

$$z' = z - \overline{z_m}, \quad z'_r = z - z_m, \quad z'_m = z_m - \overline{z_m}. \tag{4.3}$$

The mean plume positions and the displacements in the y direction can be defined in a similar manner.
Following the definition of Nieuwstadt (1992), the absolute plume dispersion, or the second-order moment, in the vertical direction is written as

$$\sigma^2_{za}(x,t) = \frac{\int c(x,y,z,t)\, z'^2\, dy\, dz}{\int c(x,y,z,t)\, dy\, dz}. \tag{4.4}$$

The absolute plume dispersion can be decomposed to its meandering and relative contributions, or dispersion due to movement of the plume centerline, or meandering, and diffusion of particles from the plume centerline. Therefore, it holds

$$\sigma^2_{za} = \sigma^2_{zm} + \sigma^2_{zr} \tag{4.5}$$

where

$$\sigma^2_{zm}(x,t) = \frac{\int c(x,y,z,t)\, z'^2_m\, dy\, dz}{\int c(x,y,z,t)\, dy\, dz}, \quad \sigma^2_{zr}(x,t) = \frac{\int c(x,y,z,t)\, z^2_r\, dy\, dz}{\int c(x,y,z,t)\, dy\, dz}. \tag{4.6}$$

The third-order moment is therefore

$$\begin{aligned}
\overline{z_a}^3(x,t) &= \frac{\int c(x,y,z,t)\, z'^3\, dy\, dz}{\int c(x,y,z,t)\, dy\, dz}, \\
\overline{z_r}^3(x,t) &= \frac{\int c(x,y,z,t)\, z^3_r\, dy\, dz}{\int c(x,y,z,t)\, dy\, dz}, \\
\overline{z_m}^3(x,t) &= \frac{\int c(x,y,z,t)\, z'^3_m\, dy\, dz}{\int c(x,y,z,t)\, dy\, dz}.
\end{aligned} \tag{4.7}$$

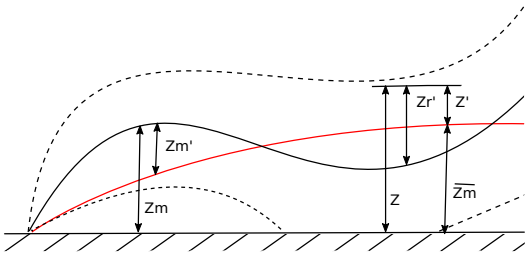

Figure 4.4: Scheme of idealized plume dispersing from a ground point-source. Shown here are the mean position of the instantaneous plume z_m and the centerline position and the total mean of centerline positions $\overline{z_m}$ (red line). Also shown are the displacements of particles in the instantaneous plume from its centerline position z_r and from the total mean centerline position z' as well as the displacement of the instantaneous centerline from the total mean centerline z'_m.

Similar expressions hold for moments in the y direction. Lastly, we define skewness here as $S_i = \frac{\overline{i^3}}{\sigma_i^3}$, where i = (y, z).

4.4 Results

4.4.1 Validation of modeled meteorological conditions with available data

Figure 4.5 shows multiple instantaneous xy cross-sections of the simulated plume from the *realistic* simulation. The cross-sections have been taken at 3 m above the ground, i.e. the inlet height on the vehicle used during the campaign (Fig. 4.1 (a)) It can be seen that the variation of the plume direction is pronounced throughout the simulation. This behavior is caused by very low mean wind speeds that change direction frequently in the simulated turbulent flow field. As was demonstrated in Section 4.2, the large-scale wind and temperature fields showed no pronounced gradients above the area on the simulated day. Therefore, local effects likely governed the flow that was measured on the site. Since ERA5 does not resolve these local effects, the discrepancies between modeled and measured wind are to be expected. To correct for this, the *idealized* simulation was set up.

Simulated and nudging profiles for the *idealized* run are compared in Fig. 4.3. Note that we replaced the ERA5 wind profiles. The simulated profiles were obtained as spatial averages over the whole domain that were time-averaged over one hour. Throughout the run, θ_l and q_t show very good agreement with the ERA5 profiles. The profiles show hardly any variability over time, and are constant with height in the lower $\approx$ 700 m. This indicates that the spin-up time of the run was sufficiently long for the development of a well-mixed boundary layer. The u wind profile in the *idealized* run shows virtually no vari-

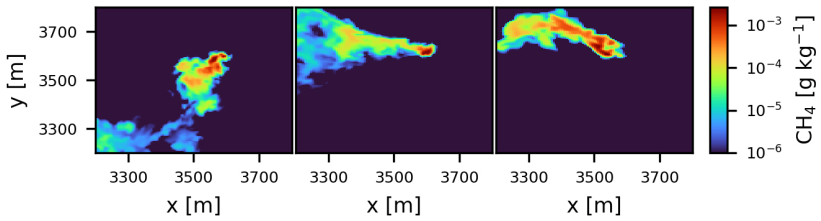

Figure 4.5: Snapshots of instantaneous plumes at 3 m above the surface. Plume at (left) 11:30:00 UTC, (middle) 12:15:00 UTC, (right) 13:00:00 UTC.

ation. A well-mixed layer above the surface is clearly visible, with stronger and constant winds above 700 m, which correspond to the nudging profiles, and a logarithmic decline towards the surface. The simulated v profiles agree with the imposed zero nudging profiles.

Figure 4.6 a shows the measured CH_4 and N_2O plumes. The plumes in the figure are shown with the background subtracted. Background subtraction follows the procedure described in Ruckstuhl et al. (2012). To help the interpretation of the plumes, N_2O was released from a cylinder 20 cm above the well head with the constant rate of (0.59 ± 0.02) g s^{-1} for the duration of the measurements.
The measured horizontal wind speed (Fig. 4.6 b) was low during the the whole day, varying from 0.8 m s^{-1} to 2.8 m s^{-1} (1-minute averages) during the measurements. A weak periodicity of approximately 55 min can be noticed in the wind speed data. It is possible that it is caused by influences from the local orography, since the area is in vicinity of hills. The closest elevated area is about 5 km away towards W, and higher mountains are located approximately 10 km towards N and NW. It was shown in the work of Nastrom et al. (1987) that the mountains can have a considerable effect on atmospheric variability on scales of 4 to 80 km. To verify the possible influence of the mountains in this case, however, the wind data should be considerably longer. The periodicity, on the other hand, is not present in the simulated wind (Fig. 4.6 b). This is caused by the imposed flat orography in the domain and the constant wind forcing through the nudging on the lateral boundaries. If the surrounding hills were included in the simulation the fluctuations in the wind direction would likely be captured. However, to achieve this, the domain would have to be expanded far beyond the measurement site but the resolution would have to stay the same to see the fine details in the plume close to the source. With the current computing resources, this endeavor is unfeasible. Nevertheless, the simulated and measured wind speeds show good agreement. This is also visible in the 1 min averages of the instantaneous wind direction (Fig. 4.6 c). Since the mean wind direction in the *idealized* simulation was set to be easterly, the wind was rotated to match the mean wind direction from the observations. It can be seen that the wind angle in the *idealized* simulation fluctuates comparable to the observations. The standard deviation in wind direction is $\sigma_{WD,obs} = 16.9°$ for the measured wind and $\sigma_{WD,LES} = 18.6°$ for the simulated

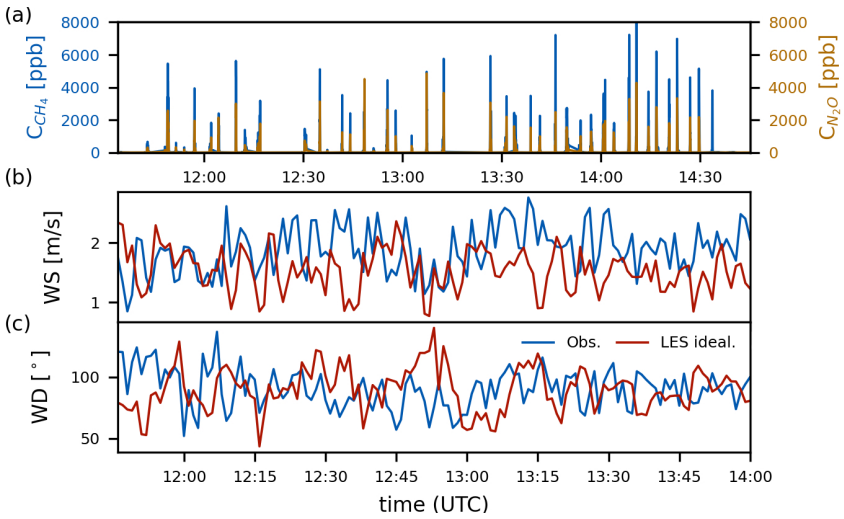

Figure 4.6: (a) CH_4 concentrations measured over the read adjacent to the emitting oil-well and N_2O concentrations emitted from next to the well. Comparison of the observed and simulated (b) horizontal wind speed, (c) horizontal wind direction. The values are given as one minute averages of instantaneous wind. The dotted lines are rolling means of respective wind speeds, shown here for easier interpretation of the mean wind speed.

one.

4.4.2 Comparison of modeled and measured plume characteristics

Time-averaged plumes from the measurements are given in the Fig. 4.7. The measured plumes were averaged over half hour increments, and are shown here together with the mean wind speed and direction for the corresponding time period. The mean horizontal wind direction did not change significantly during the measurement period, except for the first half hour, which deviates by $\approx 40°$. The mean wind speed for the whole period was small and did not exceed 2.4 m s^{-1}. Since the measurements were collected on a public road, the number of averaged plumes varies from one half-hourly period to another. The number of plumes per half-hourly time period amounts to n = [3, 6, 8, 4, 9, 10] starting from 11.30 UTC until 14.30 UTC.

On the right-hand panel of Fig. 4.7 the corresponding time-averaged simulated plumes are shown. Transects through the plume were sampled according to the observations: at 3 m height and 80 m downwind from the source. Plume transects were taken every 1 min, resulting in 150 transects for the entire simulation. After 14.00 UTC the surface flux of sensible heat turns negative and that is when the simulation stops. For that reason, the set of time-averaged plumes from LES contains one less element than the measurement set. The half-hour averages of the simulated plumes are smoother compared to the corresponding measured plume averages. This conclusion follows from comparing the average skewness of the mean plumes defined as $S = \frac{1}{\overline{x}_{max} N}(\sum_{i=1}^{N}(x_i - \overline{x})^3)^{\frac{1}{3}}$, where

x is the half-hour average from either measurement or simulation, $\overline{x}$ is the mean value of that half-hour average and $\overline{x_{max}}$ is a maximum value of the total mean plume (red line on Fig. 4.7). Therefore, the LES, CH_4 and N_2O have the average skewness of $S_{LES} = 0.32$, $S_{CH_4} = 0.44$ and $S_{N_2O} = 0.42$. This is because the number of plumes averaged per half-hour increment is much lower in the measurements compared to the simulation.
The angle over which the wind direction varies during the simulated period amounts to 18°, with the exception of the last half-hourly period period, in which the wind direction deviated from the mean by $\approx 50°$.

We used Eq. 4.1 to infer the unknown $CH4_4$ emission rate from the oil well using the LES plume as the reference. To this end, we compare the time-averaged measured CH_4 plume from the oil-well (red line in Fig. 4.7 (b)), combined with the measured mean horizontal wind speed ($\overline{u_{meas}} = 1.93$ m s^{-1}), to the corresponding flux of the time-averaged LES plume (red line in Fig. 4.7 (c)), combined with the simulated wind speed ($\overline{u_{ref}} = 1.72$ m s^{-1}). This leads to the estimated emission rate of $Q_{estim,CH_4} = (1.11 \pm 0.34)$ g s^{-1}. Using the same principle we estimate an N_2O emission rate of $Q_{estim,N_2O} = (0.53 \pm 0.15)$ g s^{-1} (true emissions was $Q_{N_2O} = (0.59 \pm 0.02)$ g s^{-1}). To benchmark the performance of LES in this experiment, we also estimate the unknown CH_4 source using the the N_2O gas as reference, and obtain an emission rate of $Q_{estim,CH_4} = (1.23 \pm 0.12)$ g s^{-1}. Note here that the standard deviations have been calculated using the source strength estimation from the half-hour averages. The discrepancies between both methods can have various reasons. Firstly, even though the mean wind in the LES is very close to the measured mean wind, their magnitudes and variations are not identical, which can also contribute to the error. However, the most notable cause for the estimation error might arise from the averaging time of the measurements, which is likely too short. It can be observed from Fig. 4.7 that the time-averaged plumes are not Gaussian shaped, which indicates that turbulent eddies of various sizes still influenced the time-averages. The deviation from the normal distribution can be estimated using the Shapiro–Wilk test, and the p-values are calculated to be $p = [9 \cdot 10^{-6}, 6 \cdot 10^{-16}, 1 \cdot 10^{-16}]$ for the LES, CH_4 and N_2O plumes respectively. Therefore, the measured plumes are deviating from the expected Gaussian profile and are not as smooth as the LES one due to the much smaller set of plumes being averaged. Nevertheless, we have shown that LES is a useful tool in source estimation in real-atmosphere conditions, e.g. in cases for which the source location is inaccessible for a tracer release.

Absolute dispersion

In this section, we analyze the general behavior of the LES plume through its first three statistical moments i.e. the center of mass, width of the plume and skewness. As shown in the previous section, the typical mobile plume measurements consist of a relatively small number of 1D plume transects. While such measurements might be well suited for inferring the unknown source strength, we aim here to exploit LES further. We will do

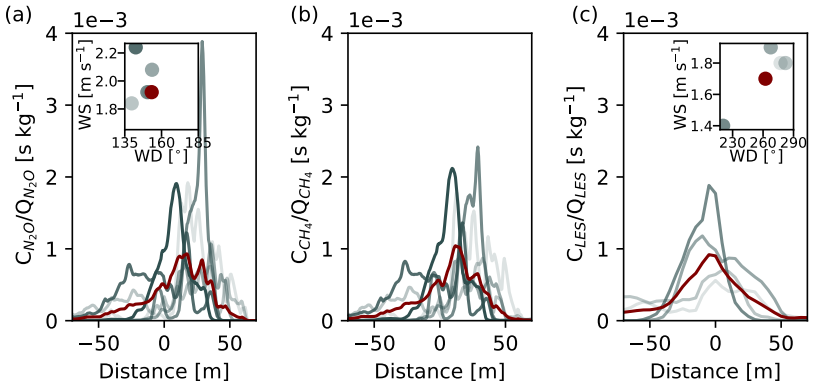

Figure 4.7: Averages of instantaneous plumes over periods of half hour from (a) N_2O, (b) CH_4 and (c) LES. All plumes have been scaled with their respective emission rates, i.e. Q_{N_2O} = 0.59 g s^{-1}, Q_{CH_4} = 1.23 g s^{-1} and Q_{LES} = 1 g s^{-1}. LES transects were taken at 3 m height and 78 m downwind from the source. Plumes are shown with a color gradient corresponding to the half-hour increments i.e. lightest gray plume is the average of plumes measured over the time period 11.30 - 12.00 UTC, dark grey is the average over 14.00 - 14.30 UTC. The inset shows horizontal wind speed and direction for the corresponding half-hour averages in (a) measurements and (c) LES. Overplotted in red is the average of all the plumes, as well as the averages of horizontal wind speed and direction in the insets.

this by linking the simulated plume to previous, more idealised, plume dispersion studies. First we focus on the absolute motion of the plume with respect to the ground surface, and will statistically analyse plume dispersion due to plume meandering and due to motions relative to the plume center of mass. In a later stage, we will separate the two, as described in Section 4.3.3, and analyse the contribution of the two processes separately.
Figure 4.8 shows instantaneous and time averaged plumes (averaged over 105 timesteps). The plumes were integrated over depth (x-y transect), and width (x-z transect). Clear differences in the structure of the plume can be observed between the instantaneous and time-averaged shape. Firstly, the top-view on the time averaged plume (panel b) shows a clear Gaussian shape as expected, which deviates from the instantaneous plume shown in panel (a). In the instantaneous plume, eddies of different sizes influence the plume throughout. The integrated x-z transect of the plume shows more complex behavior. The solid line in the bottom panel of Fig. 4.8 shows the mean of all centerline plume positions as defined by Eq. 4.2. In contrast, the dotted line denotes the position of the maximum concentration of the integrated x-z plume. Firstly, it can be noticed that the positions of the maximum and the mean do not coincide close to the source (x $\leq$ 2500 m), while at large distances the two lines tend to converge. Secondly, the position of the maximum concentration is located at the ground level for x $\leq$ 2000 m. For larger distances, the maximum concentration moves towards the top of the boundary layer and a local minimum is visible at the surface. Dosio & de Arellano (2006) performed a turbulent channel flow study with a similar set-up as we presented here. They presented their results

as a function of the normalized distance x_*, defined as:

$$x_* = \frac{w_*}{h_{BL}} \frac{x}{\overline{u}}, \tag{4.8}$$

where w_* is the convective velocity scale, h_{BL} is the height of the boundary layer, x is the distance from the source and $\overline{u}$ is the mean wind speed over the whole domain. Intuitively, this distance quantifies the number of overturns of the largest eddies (convective timescale $T_M = \frac{h_{BL}}{w_*}$) at distance x from the source (advective timescale $T_A = \frac{x}{\overline{u}}$). Dosio & de Arellano (2006) reported similar behavior in the mean of their plume emitted from an elevated source. In that simulation the concentration maximum was first transported towards the surface and later lifted towards the boundary layer top. The corresponding local minimum at the surface occurred at $x_* = 1.75$. In our simulation, with $w_* = 0.94$ m s^{-1}, $\overline{u} = 2.64$ m s^{-1}, and $h_{BL} = 564.64$ m , where the boundary layer height has been calculated as a the maximum of domain- and time- averaged vertical profile of potential temperature gradient, the minimum occurs at $x_* = 1.9$, which is in good agreement with the results of Dosio & de Arellano (2006). As mentioned previously, the position of the concentration maximum converges to the plume centerline position at larger distances from the source. This result, however, differs from the results reported by Dosio & de Arellano (2006). In their simulation, the plume never reaches a well-mixed state, which was in agreement with water tank experiments performed by Willis & Deardorff (1978) who reported well-mixed plume only at very large distances from the source at $x_* = 6$. In comparison, in our simulation the maximum of concentration starts approaching the mean plume position at $x_* \approx 2.5$. The instantaneous plume we show here (Figure 4.8, panel (c)), has stayed close to the ground for ≈ 1500 m from the source, after which it gets mixed in with larger sized eddies towards the top of the boundary layer. Additionally, puff-like structures with higher concentrations can be observed, which have been lifted from the ground and are carried to the top of the BL even at large distances from the source (e.g. x = 3000 m).

Figure 4.9 shows the first three statistical moments of the plume. The top two panels show the plume centerline position in the y and z direction, downwind from the source. The centerlines of the instantaneous plume positions in y direction show large variability throughout the domain. However, the mean center of mass is constant and centered at the y-position of the source. In contrast, the centerline position of the plume in the z-direction changes drastically downwind from the source and stabilises at approximately 300 m height at 1500 m from the source. As the plume gets mixed through the boundary layer, the variability in the plume centerline positions drops. Thus, while in the y direction the plume keeps growing throughout the domain, the growth stops in the z-direction once the plume reaches the top of the boundary layer (Fig. 4.9 c,d). The skewness of the plume positions (Fig. 4.9 e) shows that the plume is oscillating around its mean value in the y direction. In the vertical direction, however, the instantaneous plumes are more

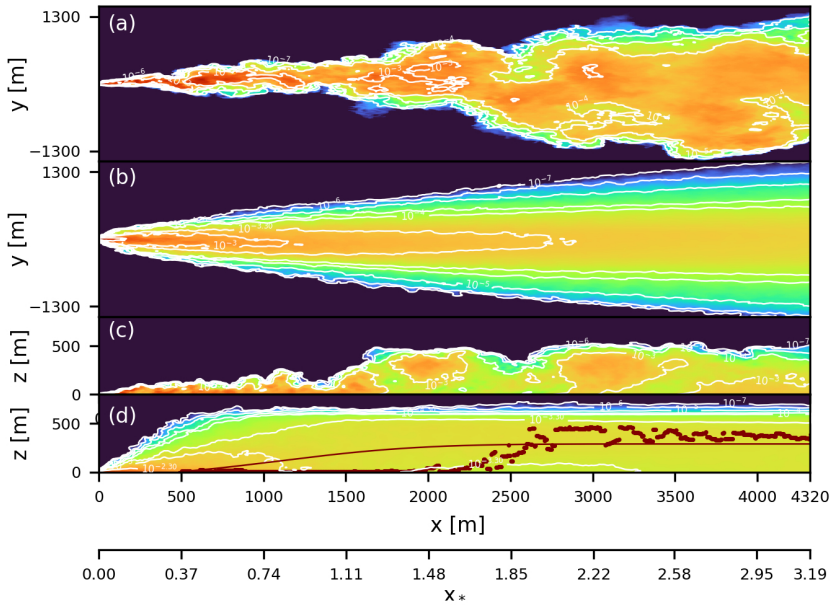

Figure 4.8: Top view on vertically integrated (a) instantaneous and (b) time averaged plume. Horizontally integrated (c) instantaneous and (d) time-averaged plume. On (d) are also shown mean plume centerline position (solid red line) and position of the maximum of concentrations (dotted red line). x_* is the normalized distance from the source as defined in Eq. 4.8.

likely to have their centerline position below the mean plume centerline in the first 1500 m from the source ($\overline{S_{za}} \geq 0$).

To inspect the skewness of the plume more closely, Fig. 4.10 shows probability density functions (pdfs) of center of mass positions in the y and z directions around their mean values at various downwind distances. As already noted in discussing Fig. 4.9, in the y-direction the plume positions show a Gaussian distribution on all distances from the source. Note that the spread of the centerline positions grows with distance from the source, indicating that the plume gets moved further away from the mean centerline position with bigger and bigger eddies. This Gaussian distribution of the plume centerline position was also found in previous studies. For instance, Gailis et al. (2007) assumed a Gaussian distribution of the plume centerline position for their fluctuating plume model, which they experimentally confirmed in a water channel experiment. In contrast, close to the source, the centerline position distribution in the z-direction is positively skewed. A Gaussian distribution is attained further downwind. This result differs somewhat from the previous studies (Gailis et al., 2007; Marro et al., 2015), in which a lognormal and reflected Gaussian distribution were assumed for modelling the plume vertical mean position. We show here that only close to the source, the lognormal distribution provides a good description of the centerline positions. Further downwind, where the plume gets better mixed in the convective boundary layer, the centerline position starts oscillating around its mean position.

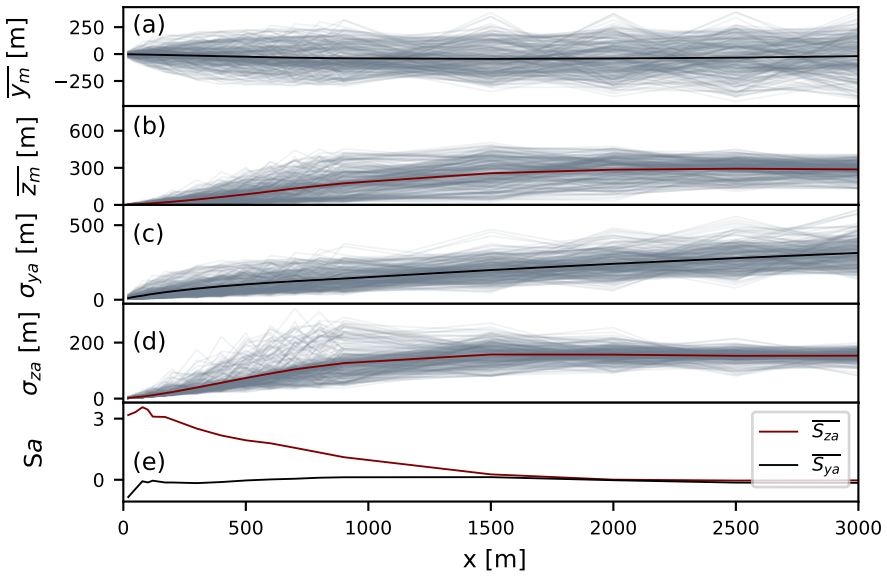

Figure 4.9: The first three statistical moments of the simulated plume in the absolute coordinate system. The first four panels show: position of the center of mass in y and z direction and the plume width in the y and z directions. All values are shown as function of downwind distance x. Grey lines denote instantaneous plumes and mean values are shown as solid black and red lines in y and z directions, respectively. The bottom panel shows the skewness of the mean centerline plume position as a function of distance from the source.

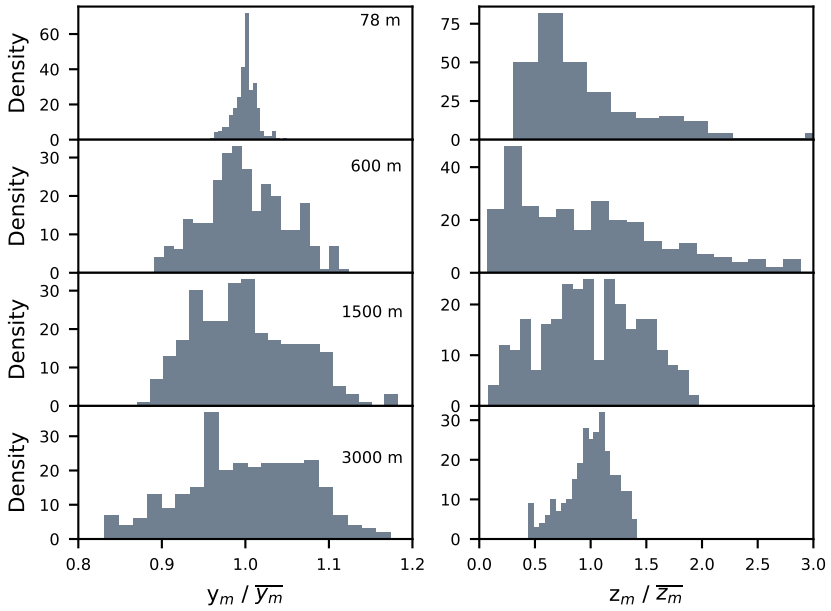

Figure 4.10: Probability density functions of the instantaneous plume position scaled with the mean centerline position at various downwind distances from the source.

Relative dispersion

There are two processes that affect plume growth: meandering motions (discussed in the previous section) and relative dispersion due to mixing by small eddies. Understanding these two processes, and quantifying where a certain process is dominant, can aid the development of measurement strategies. For example, at downwind distances where relative dispersion dominates, the instantaneous plumes remain close to the mean position, and the chance of measuring the plume close to its centerline increases.
Firstly, we focus on the relative dispersion. Relative dispersion is defined as dispersion of the plume around its centerline due the eddies of comparable size or smaller than the plume. We present second and third order statistics of relative plume dispersion in Figure 4.11 (left column). Close to the source, the contribution of relative dispersion to the total plume growth is still small, which is especially visible in the y- direction (Fig 4.11 a). As the plume moves away from the source, it grows in size. This enables bigger and bigger eddies to be involved in the mixing of the plume (Cassiani et al., 2020). For this reason, the size of the plume due to relative dispersion is growing downwind from the source at a constant rate. Similar behaviour is seen for dispersion in the z-direction. Close to the source, the contribution of relative dispersion is small and it grows further downwind. Unlike the z-direction, in which the plume growth is limited by the size of the BL, the growth of the plume in the y-direction is unrestricted by boundaries. This implies that the plume growth will continue until the plume is so dispersed that it becomes indistinguishable from the background concentrations. The skewness of the relative plume dispersion in the z-direction shows a positive value close to the source, which can be attributed to plume reflection at the surface. Since the small turbulent motions that are responsible for relative dispersion are random and Gaussian in nature, the asymmetry has to originate from the fact that the plume is close to the surface (Dosio & de Arellano, 2006). In the y-direction, the plume shows virtually no skewness.

Meandering

Finally, we look at the plume dispersion due to the meandering of the plume, i.e. displacement of the plume caused by the eddies that are larger than the plume itself. Figure 4.11 (right column) shows the second and third moment of the plume due to the meandering motions. It can be observed that in the y-direction the plume shows large symmetric growth very close to the source (Fig. 4.11 b). The magnitude of the meandering component in this region is up to 2.5 times larger than the relative dispersion (Fig. 4.11 a). However, while the relative contribution continues to grow further downwind, the growth due to meandering drops significantly and becomes almost constant. This observation is in line with the theoretical analysis given in Csanady (1973) where y-scaling was reported according to $\sigma_{ym} = \sigma_v t$ (where σ_v is the variance of the v component of velocity and t is the time since the plume left its source) close to the source, and $\frac{d\sigma_{ym}}{dt} = 0$ far from the source. This was later confirmed in the water tank experiment by Weil et al. (2002),

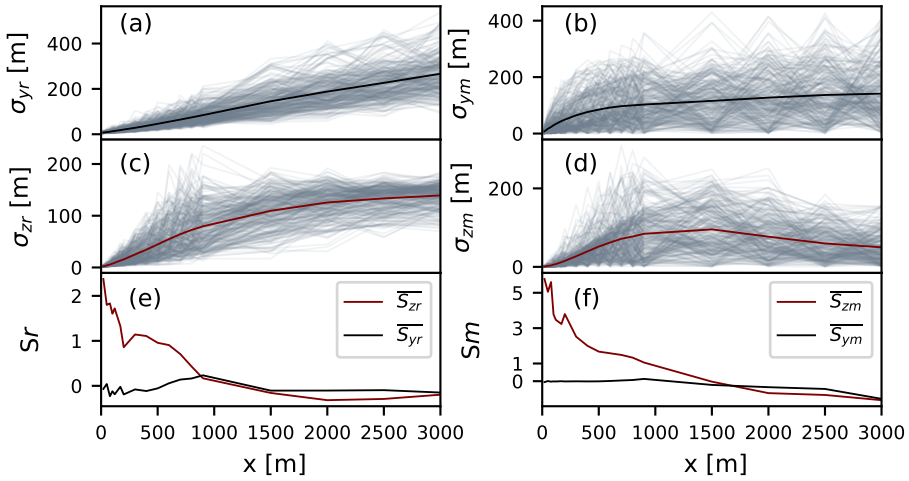

Figure 4.11: The second and third statistical moments of the simulated plume for the relative (left column) components centered around the mean plume position and for the meandering (right column) components. The first two panels in a row show the plume width in the y and z directions. All values are shown as functions of downwind distance. In grey are shown values of instantaneous plumes while their mean values are shown as solid black and red lines in y and z directions respectively. The last panel shows skewness of the mean relative plume position as a function of distance from the source.

and the LES study presented by Dosio & de Arellano (2006). Our results agree well close to the source. However, in our simulation there are still eddies big enough to move the whole plume even far downwind, since our value of σ_{ym} does not become fully constant. In contrast, the contribution of meandering to the total dispersion in z-direction tends to zero further downwind from the source. The size of the eddies that develop in vertical direction is constrained by the depth of the boundary layer. For this reason, with only meandering, the plume attains a size comparable to these eddies.

The distance at which the relative regime becomes predominant can be estimated from the relevant convective and advective timescales introduced in Section 4.4.2. When the two time-scales become equal, the plume has spent enough time in "flight" to be mixed with the largest eddies. Therefore, a length-scale, L_{mix}, can be derived that defines the downwind distance at which the plume starts to be mixed with eddies of all sizes and at which the relative dispersion becomes predominant

$$L_{mix} = \frac{\overline{u}\, h_{BL}}{w_*}. \tag{4.9}$$

In this study, this distance amounts to $L_{mix} \approx 1360$ m. Alternatively, this distance can be obtained from the meandering ratio $M \equiv \sigma_{im}/\sigma_{ir}$, i = y,z (Oskuie et al., 2015). When M drops to values smaller than 1, the relative dispersion becomes the dominant process. This occurs at $x \approx 1320$ m downwind of the source, which is in good agreement with the estimated length scale. Note that this distance is specific for each case. It depends not

only on the turbulence regime and the BL height, but also on the release height.

4.4.3 Concentration statistics

Finally, we will present concentration statistic in the absolute and relative coordinate systems. Additionally, we will compare these statistics to parametrizations that are commonly used in fluctuating plume models (Gailis et al., 2007; Marro et al., 2015; Cassiani et al., 2020). These fluctuating plume models have been validated against dispersion studies in laboratory channel flows, often by taking line transects through the plume (e.g. Nironi et al. (2015)). Here we aim to utilize the high spatial and temporal resolution of LES to estimate dispersion parameters, needed in these models. Figure 4.12 (first and second row) shows y-z transects through the time-averaged plume (average of 287 instantaneous plumes) in the absolute (left) and relative (right) coordinate systems. In the relative system, the instantaneous plumes were aligned with the center of mass of the mean plume ($\overline{y_m}$, $\overline{z_m}$). It can be seen that close to the source (top row) the two plumes are similar in shape since the maximum of concentration and centerline position still coincide. Further downwind, there is a clear difference between the plumes since the plume entered the regime in which it was more frequently carried upwards by strong ejections (see e.g. Fig. 4.10). On the distances furthest downwind (Fig. 4.12, bottom row) the two plumes again attain similar shapes. Here, the relative dispersion is the dominant mechanism and the centerlines of the instantaneous plumes do not move far from its mean position by meandering motions. For the two distances closer to the source, the edges of the plumes show large variability, despite the large amount of plume transects that was used in time-averaging. This is caused by the plume behaviour. Close to the source, the plume tends to stay close to the ground. The large spatial variability away from the ground is caused by occasional ejections by strong upwards motions. Further downwind, the plumes attain a more uniform shape, resembling a Gaussian distribution.

Parametrization of concentration fluctuations intensity

One of the commonly used parameters to model the concentration *pdf* is the concentration fluctuation intensity, defined as $i_c = \frac{\sigma_c}{\bar{c}}$ (Gailis et al., 2007; Nironi et al., 2015; Cassiani et al., 2020), with $\bar{c}$ being the mean concentration (x of plumes averaged) and σ_c its standard deviation. As pointed out in Marro et al. (2015), the spatial evolution of this non-dimensional parameter is often assumed to depend only on the x-coordinate. This can lead to significant discrepancies between modeled concentration fields and the measured ones. We use LES to demonstrate the complex spatial structure of variable i_c, both in absolute and relative coordinates, over a plume crosswind transect (Fig. 4.12, third and fourth rows). Close to the plume centerline i_c has minimum value, but it increases noticeably towards the plume edge. This is most clearly visible close to the source. In the far-field, these differences are less pronounced, which is a consequence of plume being better mixed, which decreases the intermittent behavior.

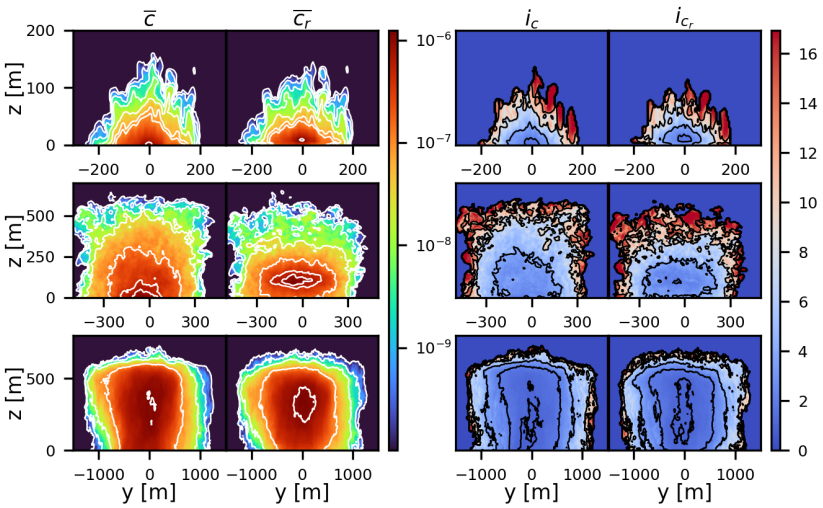

Figure 4.12: (First two columns) y-z transect of mean plume concentrations in absolute ($\overline{c}$) and relative ($\overline{c_r}$) coordinate system. (Last two columns) Concentration fluctuation intensity in y-z plume in absolute (i_c)and relative ($_{cr}$) coordinate systems. Distances from the source are (top) 100 m, (middle) 600 m and (bottom) 3000 m.

Furthermore, from a measurement point of view, knowledge of the shape of i_c can help in planning the measurement campaigns. High values of the i_c imply that the probability of measuring the plume in that area are lower, longer measurement times are required to achieve reliable plume statistics. Knowledge of the optimal downwind distance and height at which to measure can considerably improve the efficiency of the measurement process. The measurements used in this study were taken as line transects at a single height (3 m). According to the results presented here, at 3 m height the plume was the least fluctuating very close to the source ($x \lesssim 300$ m) and in the far field ($x \gtrsim 1500$ m). We have previously shown that in the close field the pdf of vertical centerline position is positively skewed (Fig. 4.10 right row), therefore there was higher likeliness of capturing the plume closer to the ground than at its centerline. Conversely, far from the source, the plume is oscillating around its centerline and there is the highest chance of measuring the plume. In the mid-field ($300 \gtrsim x \lesssim 1500$ m), the plume is highly oscillating at the ground and at the centerline position, but since it is still positively skewed, there is a higher chance of measuring the plume at the ground.

The complex 3D structure of i_{cr} has been addressed in previous studies. Marro et al. (2015) expanded upon the definition of i_{cr} given in Gailis et al. (2007), where the relative concentration fluctuation has been expressed in terms of the mean relative concentration

field. The model presented in Marro et al. (2015) is given as:

$$\begin{aligned} i_{cr}^2 =& (1+i_{cr0})^2 \left\{ \exp\left[-\frac{(y-y_m)^2}{2\sigma_{yr}^2} \right] \right\}^{-\zeta_y(x)} \\ & \times \left\{ \exp\left[-\frac{(z-z_m)^2}{2\sigma_{zr}^2} \right] + \exp\left[-\frac{(z+z_m)^2}{2\sigma_{zr}^2} \right] \right\}^{-\zeta_z(x)} \\ & \times \left\{ 1 + \exp\left[-\frac{(2z_m)^2}{2\sigma_{zr}^2} \right] \right\}^{-\zeta_z(x)} - 1, \end{aligned} \tag{4.10}$$

where i_{cr0} is the value of relative concentration fluctuation at the plume centerline (Fig 4.13 a), $\zeta_y(x)$ and $\zeta_z(x)$ are the shape parameters introduced to account for anisotropy in the y and z directions. The variables that determine the crosswind shape of i_{cr}, y_m, z_m, σ_{yr} and σ_{zr}, need to be either determined from plume measurements, or parametrized using one of the models (e.g. Gailis et al. (2007), Marro et al. (2015)). Here they are calculated from the LES data as defined in section 4.3.3. The two ζ functions were assumed to be sigmoid, such that the modeled i_{cr} has value i_{cr0} close to the source and has self-similar profiles in the far field in both y and z directions. As previously mentioned, the LES data show the U-shaped profile in the far field, but also close to the source (not shown). This is likely caused by the fact that in the simulation the source is not introduced as point source, as assumed in the plume model, but as a 2D Gaussian in the x and y directions with one standard deviation the size of one grid box ($\Delta\mathrm{x} = \Delta\mathrm{y} = \sigma_{source} = 5$ m). Therefore, 95 % of mass is being emitted from an area that has an horizontal transect of 20 m. The size of the smallest eddies that can develop in the simulation is $\approx 4\Delta\mathrm{x}$. This means that very close to the source there is no internal mixing in the plume by the smaller eddies and all of the fluctuations are caused by entrainment of ambient air by eddies comparable in size to the plume.

We have adapted the definition of the shape functions ζ given in Marro et al. (2015) to account for the shape of the source in the near-field y direction and kept the same behavior in the far-field. The far-field was defined as the distance at which the relative dispersion becomes dominant, therefore at the characteristic length scale $L \approx 1360$ m (section 4.4.2). The slope of the sigmoid function β, which defines the shape of functions ζ, was determined using L. It was assumed that at distance L from the source the value of ζ has p % (here used $p = 70$ %) of the amplitude defined in Marro et al. (2015). p was chosen as the ratio of relative to absolute dispersion for the respective directions at the distance L. As a result, the functions take the shape:

$$\zeta_y = \gamma + \frac{\alpha_y - \gamma}{1 + \exp\left[-\beta_y(x - x_0)\right]}, \qquad \zeta_z = \frac{\alpha_z}{1 + \exp\left[-\beta_z(x - x_0)\right]}. \tag{4.11}$$

Where $\gamma = 2 \times 10^{-3}$ is the correction for the shape of the source, $\alpha_y = 0.45$ and $\alpha_z = 0.9$ are the amplitudes taken from Marro et al. (2015), $x_0 = 0.5L$ is the location of the

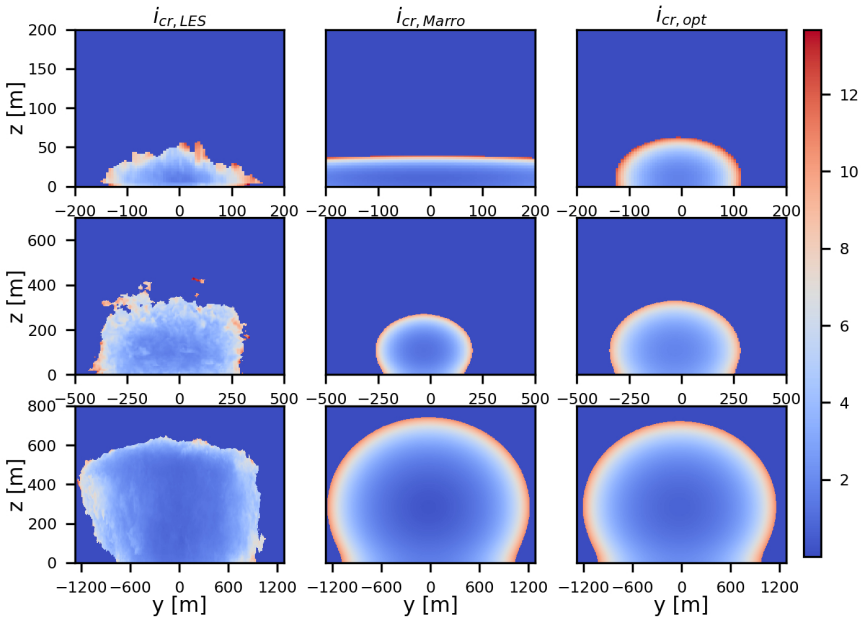

Figure 4.13: y-z transect of the concentration fluctuation intensity in the relative coordinate system i_{cr} calculated from the LES data. The other two columns show i_{cr} calculated with Eq. 4.10 as found in the literature (middle column) and optimized for this case (right-hand column).

function's midpoint, and the slopes are calculated as:

$$\beta_y = -\frac{2}{L}\ln\left(\frac{(1-p)\,\alpha_y}{p\,\alpha_y - \gamma}\right), \qquad \beta_z = -\frac{2}{L}\ln(1-p). \tag{4.12}$$

Figure 4.13 shows the comparison of i_{cr} calculated from the LES data and i_{cr} modeled with the two definitions of the ζ function. As previously mentioned, the definition of ζ found in the literature (Marro et al., 2015) agrees well with the LES-calculated relative fluctuations in the far field. Very close to the source the LES plume has a similar structure as in the far field, which is not accounted for when the assumption of constant valued i_{cr} is made. When the correction for the source shape is added (equation 4.11), the i_{cr} model represents the plume behavior well, both in the far-field and close to the source. It should be noted here that the plume behavior at distances from the source where meandering is important, is still misrepresented by the plume model.

One of the assumptions in the meandering plume model is that the relative dispersion and the fluctuations of the instantaneous center of mass are statistically independent processes. This assumption is violated when the size of the plume is comparable to the average size of eddies in the domain. In this case, the eddies that are capable of moving the center of the mass of the instantaneous plume are still small enough to entrain ambient air deep into the plume making the separation of two processes complicated.

Concentration probability density function

Lastly, we look at the concentration *pdf* at multiple in-plume locations. A large number of studies have found the Gamma distribution to be an appropriate description for the *pdf* of relative concentrations in the far-field (e.g. Dosio & de Arellano (2006), Nironi et al. (2015), Marro et al. (2015), Cassiani et al. (2020)). In the far field, relative dispersion becomes the main mechanism that drives the plume fluctuations. Therefore, the probability of the plume centerline position tends towards a Dirac delta function, and the plume spread due to meandering motions becomes negligible. The *pdf* can then be expressed as:

$$p = \frac{\lambda^{\lambda}}{\overline{c_r}\,\Gamma(\lambda)}\Big(\frac{c_r}{\overline{c_r}}\Big)^{\lambda-1}\exp\Big(-\frac{\lambda\, c_r}{\overline{c_r}}\Big), \tag{4.13}$$

where $\lambda = 1/i_{cr}^2$ and the subscript r denotes the relative plume. Figure 4.14 shows *pdf*s of the relative concentration sampled at the plume centerline on multiple downwind distances and, for comparison, at the inlet height at which data presented in section 4.2.2 were measured. The Gamma distribution is indeed a good fit for concentration *pdf* at the plume centerline on most downwind distances. The mean p-value calculated using the Kolmogorov–Smirnov test amounted to 0.26 in the range $x = [100, 1500]$ m downwind from the source. The optimal range of downwind distances where the Gamma distribution is the best fit for the p.d.f has also been found in the LES study of Ardeshiri et al. (2020) where they connected the start of this range with the maximum of i_{cr} on the centerline. Following the results on Fig 4.14, the Gamma functions at the inlet height (z = 3 m) seem to reasonably fit the concentrations away from the plume centerline. However, the p-values obtained from the Kolmogorov–Smirnov test on most all downwind distances had values had values below 0.05 which indicates that the Gamma in this case is not the best fit. Note that the i_{cr} that was used here for the calculation of the *pdf* has been calculated from the LES data. We concluded earlier that the i_{cr} has a complex structure, which cannot be assumed constant in the y-z plane. When its value is known, either from data or from an appropriate plume model, the *pdf* of concentration fluctuations can be modeled with a Gamma distribution for a certain in-plume location.

4.5 Conclusions

Our study aimed to bring together field observations and high-resolution simulations. Large-eddy simulations (LES) have been employed in dispersion studies for the past few decades, but most often simulating dispersion in somewhat idealized settings. The models capable of performing LES are constantly being improved, with higher spatial resolution, and with new parameterizations that include more processes that influence the plume dispersion. We demonstrated here the ability of LES to reproduce plume dispersion in an actual field campaign. We took a step away from idealized channel flows, and used available meteorological data to reproduce field conditions encountered during the campaign.

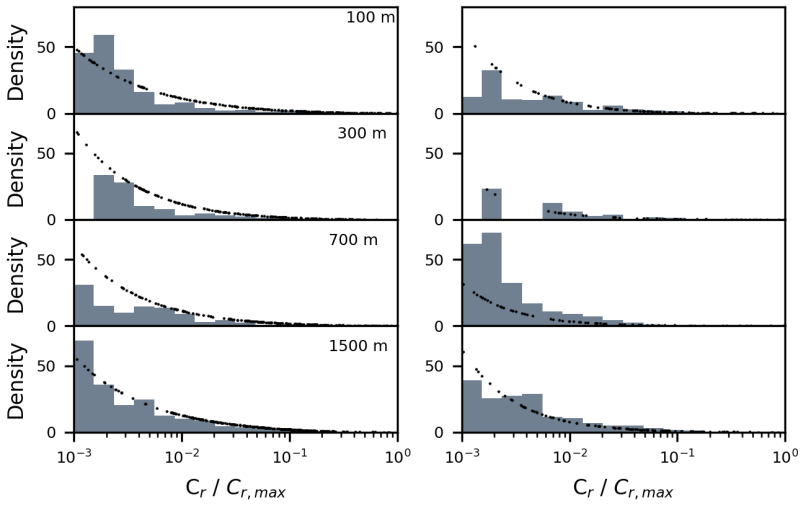

Figure 4.14: Probability density function of concentrations at the plume centerline (left) and at the measurement inlet height (right, see Section 4.2.2) at multiple downwind distances. Over-plotted are Gamma function fits.

Since field observations are sparse, LES can lead to improved understanding in plume behaviour, which can help with planning and optimizing future measurement strategies. In particular, LES can aid in understanding on which heights the plumes centerline can be expected depending on the downwind distance and where the plume is expected to be most fluctuating which then requires a higher number of measurements to average out the atmospheric variability from the mean plume. The case we studied was a methane plume emitted from an oil well that was measured during one day of the Romanian methane emissions from gas and oil industry (ROMEO) campaign. The boundary conditions in the LES were derived from ERA5 data (Hersbach et al., 2020) to ensure correct meteorological conditions in the simulation. The plume in the simulation was released from the lower boundary and sampled in accordance with the field observations.

Firstly, the meteorological variables from the LES were compared with the available field data and the ERA5 profiles. The vertical profiles of specific humidity and temperature in ERA5 data showed little variability for the period in which the measurements were taken. The LES was able to reproduce these profiles correctly. There was very little large-scale advection present for the chosen day, which implies that the wind was driven by local temperature differences and orography that are not properly captured with the model resolution of ERA5. This resulted in discrepancies between the LES generated wind profiles and the measured wind. The issue was circumvented by applying a wind correction and performing a second simulation with this background wind. While the forcing of the boundary conditions with the ERA5 data gave good results, more detailed measurements of meteorological variables (e.g. vertical profiles of wind components, temperature, humidity etc.), together with plume measurements would help to better evaluate

the simulations.

Secondly, the LES was compared against plume observations. A methane plume emitted from an oil well was sampled with an instrument mounted on a moving vehicle. A tracer gas plume emitted close to the oil well was measured simultaneously. The tracer gas plume was used in the estimation of the emission rate from the unknown source. Our aim in this study was to evaluate whether LES can be used as a proxy for the tracer gas. The estimate of the emission rate from the oil well using the tracer gas plume is $Q_{CH_4} = (1.23 \pm 0.12)$ g s^{-1}. Using LES, we found $Q_{CH_4,LES} = (1.11 \pm 0.34)$ g s^{-1}, i.e. a value 10 % lower. To further evaluate LES, we estimated the emission rate of the tracer gas ($Q_{N_2O} = (0.59 \pm 0.02)$ g s^{-1}) using the simulated plume, and found a value of $Q_{N2O,LES} = (0.53 \pm 0.15)$ g s^{-1}. Part of the differences in the estimated emission rates can be attributed to the different mean wind speeds in the simulation and in the measurements. Nevertheless, it was shown that, using a careful set-up of the simulations, LES can replace the co-emitted tracer gas, e.g. in cases of poor access to the source area.

LES provides concentration fields throughout the domain with great temporal and spatial detail. This allows for a more in-depth study of the behavior of the measured plume. The plume was studied by analyzing its absolute position, and by separating the processes driving its dispersion into meandering motions of the plume centerline and the relative dispersion around this centerline. A good agreement of the plume behavior was found with previous experimental and theoretical dispersion studies targeting channel flows. Furthermore, a plume mixing length-scale L was derived from the boundary-layer height, the mean horizontal wind speed and convective velocity scale. This scale was demonstrated to coincide with the distance from the source at which the relative dispersion becomes the main mechanism of plume growth, and for this case study, L is calculated to be 1360 m.

Finally, we used LES to examine parameterizations of concentration fluctuations in simple models: the fluctuating plume model. We did this by focusing on the concentration fluctuation intensity parameter, i_c, an often utilized parameter. LES can provide the detailed 2D fields of i_c, something that is difficult to obtain in laboratory experiments. We confirmed the characteristic U-shape in a horizontal crosswind transect of concentration fluctuation intensity in a relative coordinate system i_{cr} (Gailis et al., 2007) not only in the far field, but also close to the source. We speculate that this is due to spatial extent of the source in the simulation, imposed to avoid numerical instabilities. In this way the simulation differs from the field experiments, where close to the source the plume is mixed by eddies ranging from the Kolmogorov scale to the size of the plume itself, making the plume compact and very well mixed. We adapted the semi-empirical model for i_{cr} from Marro et al. (2015) to account for the source shape and this model showed good agreement with LES.
Furthermore, the knowledge of the shape of i_c can help in planning future measurement

campaigns as it is an indication of the chance that the plume will be measured. For the campaign analysed here it seems that the plume was measured where there was the highest chance of capturing it – close to the source and the ground. In general, far away from the source the plume is best measured close to its mean centerline, which is likely lifted off the ground as the plume gets mixed throughout the boundary layer. Close to the source, however, the plume is mostly below its centerline, so the chances for measuring it are higher closer to the ground. Following the study of Dosio & de Arellano (2006) of dispersion form an elevated source in a convective boundary layer, it seems that this is true for the lifted sources as well, close to the source most plumes first get transported to the ground and then mixed through the BL with larger eddies.

Finally, previous studies found that the probability density function for concentrations in the relative plume can be described by a Gamma distribution. This finding was also confirmed in this study. With the spatial variability of i_{cr} is taken into account, the Gamma distribution is a good fit for the concentration distribution on various downwind distances.

In conclusion, LES has shown to be an invaluable tool for studying plume dispersion. In this study LES has been pushed a step further to bridge the gap between field experiments and simulations. LES can properly reproduce meteorological conditions, but future campaign should provide more detailed measurements to further drive and evaluate the simulations. In the future, more detailed LES models will become feasible due to more powerful computers. For this reason, high-resolution and realistic atmospheric dispersion simulations will likely play an increasing role in tracer dispersion studies.

Chapter 5

Dependency of plume dispersion on Reynolds number

This chapter is based on: Ražnjević, A., van Heerwaarden, C., & Krol, M. Dependency of plume dispersion on Reynolds number. (In preparation)

Abstract

This study tests the ability of direct numerical simulations (DNS) to perform simulations of plume dispersion in flows characterized by low to moderate turbulence. DNS experiments are compared to large-eddy simulations (LES) in the exact same set-up. The study is motivated by the idea that the most relevant plume statistics of higher order will reach the Reynolds number similarity at less–than–atmospheric turbulent flows. This would support the use of DNS in dispersion studies as they, unlike LES, fully resolve all turbulence in the simulations. The study aims to reproduce the wind-tunnel experiment of Nironi et al. (2015) and simulates plumes released from point sources into a neutrally stratified flow over flat terrain. The plumes were released from two heights; very close to the ground and further away from the surface, i.e. at 6% and 19% of the boundary layer height. The study comprises of a series of DNS experiments (five in total) with increasing Reynolds number as well as two LES experiments with low and high spatial resolution. Results for the velocity statistics show very good agreement between the experimental data and simulations, with only cross-wind components of wind variances being somewhat underestimated in all simulations, both DNS and LES. For the plume statistics, the mean plume is well represented in all simulations. For the higher order moments, only the most turbulent DNS ($\mathrm{Re}_\tau = [1118, 1862]$) converge to the experimental values, and perform better than LES on downwind distances closest to the source. Further downwind, DNS experiments overestimate higher order statistics and LES outperforms DNS. The computational cost of the most turbulent DNS was about 3 times as large as that of the high resolution LES, showing that DNS is a viable choice for dispersion studies, especially for close-source studies.

5.1 Introduction

Accurate modelling of passive scalar plume dispersion in the atmosphere is of great importance and interest in many areas of society. Being able to predict where and how a plume will disperse has direct application in fields ranging from air quality in cities, greenhouse gas emission estimation, to military applications. Nevertheless, due to the turbulent nature of the plumes, especially close to their sources where eddies of all sizes significantly influence plume motions (Cassiani et al., 2020), accurate modelling still poses a great challenge. The problem of plume dispersion can be addressed from either Lagrangian or Eulerian perspectives, and we will here focus on only on the latter. For a more detailed overview of different modelling techniques we refer the reader to the review paper of Cassiani et al. (2020). In the scope of the Eulerian reference framework, models range from completely stationary Gaussian plume model (GPM) to fully turbulence resolving direct numerical simulations (DNS). The GPM is very simple and easy to use, but cannot provide the detailed structure of instantaneous plumes, while DNS provides instantaneous turbulent velocity and scalar fields, but is computationally extremely expensive for atmospheric Reynolds numbers (Re). Between these two ends, models like Reynolds-averaged numerical simulations (RANS) and large-eddy simulations (LES) vary in the level in which the turbulent velocity spectra are being resolved and how much they are being parameterized. However, all these methods are computationally more affordable than DNS, but parametrization of part of the velocity field will inherently cause inaccuracies on very small dispersion scales (i.e. close to the source). Therefore, the aim of this study is to test the ability of DNS to accurately reproduce plume dispersion for less–than–atmospheric Re number flows.

In LES, the eddies of the smallest scales are filtered and parametrized by one of the subgrid-scale (SGS) models, while the larger motions are resolved (e.g. Deardorff (1973); Pope (2000)). The main advantage of this approach is that flows with very large Re can be simulated (Ardeshiri et al., 2020). However, despite the large advantages LES experiments have over, for example, time averaged numerical models, there are still some issues arising from the numerical approach and the assumptions in the simulations. For instance, LES has been proven to be sensitive to the cut-off frequencies at which filtering of the small scale begins and the resolution (e.g. Pope (2004); Kemenov et al. (2012)). Simulations with very high (atmospheric) Reynolds numbers come at a cost of unresolved turbulence near walls. In these regions, wall models are used to calculate surface fluxes using the Monin-Obukhov similarity theory (van Heerwaarden et al., 2017). Despite the associated uncertainties, LES has been used in various dispersion studies in the atmospheric boundary layer (ABL). One of the first studies was performed by Henn & Sykes (1992), who simulated dispersion in neutral and convective ABLs. Xie at al. (2004) studied dispersion from sources on different elevations and Xie et al. (2007) addressed dispersion over rough walls, both in a neutrally stratified ABL. Dosio & de Arellano (2006) focused on disper-

sion from a line source in a convective ABL. Recently, Ardeshiri et al. (2020) showed non-monotonic dependence of scalar concentration statistics on the resolution in LES. The influence of the source size on near-field dispersion has been recognized in wind tunnel experiments (Fackrell & Robins,, 1982a,b; Nironi et al., 2015). Following this result, Ardeshiri et al. (2020) showed that the production of scalar fluctuations mostly occurs close to the source. Therefore, a proper resolution of the source is of great importance, and Ardeshiri et al. (2020) advise to use at least 4^3 grid nodes to resolve the source. Their result implies that, in order to properly resolve a very small point source, a very large spatial resolution is needed, which increases the computational cost considerably.

In contrast to LES, DNS resolves all scales of motion. Therefore, DNS is free of uncertainties that follow from the approximations in LES, but due to high computational cost it is unfeasible for simulations with atmospheric Reynolds numbers (e.g. Pope (2000)). Another challenge for DNS is simulating flow over rough surfaces as they directly influence the heat and momentum transfer that are directly linked to the shape of the roughness elements (Kadivar et al., 2021). Despite not being frequently used, DNS has been employed in several dispersion studies at low and moderate Reynolds numbers mostly for neutral channel flows. For example, Vrieling & Nieuwstadt (2003) studied a neutral channel flow with $\mathrm{Re}_\tau = 360$ ($\mathrm{Re}_\tau = \frac{u_\tau \delta}{\nu}$, where u_τ is the friction velocity, δ is channel depth and ν is the kinematic viscosity). Oskouie et al. (2017) studied interference of two plumes emitted from ground point sources and Oskouie et al. (2018) studied interference of plumes from two line sources, both in neutral channel flows. DNS has also proven to be a useful tool for studying dispersion in an urban-like set of obstacles (Branford et al., 2011; Coceal et al., 2014).

As previously mentioned, DNS is currently unfeasible for atmospheric Reynolds numbers. Nevertheless, due to Reynolds number similarity, reaching such highly turbulent flows is not always necessary. Reynolds number similarity is a characteristic of fluids to have flow properties independent of the Reynolds number after a certain critical value (Mellado et al., 2018). For DNS of a neutral channel flow this has been demonstrated in the seminal paper by Moser et al. (1999) for Re_τ up to 590. Recently, Mellado et al. (2018) demonstrated Reynolds number convergence in a DNS of shallow stratocumulus formation. They argue that relevant processes in the cloud formation are driven by scales which are unresolved in LES, and they showed the necessity of performing a DNS to accompany LES studies. Similarly, our aim in this paper is to show that DNS performs well at sufficiently high Reynolds numbers and at reasonable computational costs.

The structure of the paper is as follows: in section 5.2 we outline the numerical model MicroHH which is used to perform LES and DNS experiments. In section 5.2.1 the set-up of the experiments is presented. The results are presented in section 5.3, in which we first discuss statistics of the velocity field and the energy budget (Section 5.3.1). This is followed by a discussion on the plume statistics in section 5.3.2. In the last part of

our results (Section 5.3.3), we present a more in-depth look into the main drivers of dispersion and finally we give a short summary and discussion of our main findings in section 5.4.

5.2 Methods

Numerical simulations were performed using the MicroHH model (van Heerwaarden et al., 2017). The code solves conservation equations for mass, momentum and energy under the Boussinesq approximation. The dynamics of the system is solved using a second order finite volume scheme. The sixth order interpolation scheme is used for advection of scalars with a flux limiter applied to ensure monotonicity. The time integration is achieved using a third order Runge-Kutta scheme. To run LES, a second order Smagorinsky model is used for subgrid-scale parametrizations.

For the three velocity components, periodic boundary conditions were imposed on the lateral boundaries. On the upper boundary, a free-slip condition was used, where tangential components of the velocity were assumed to be zero ($\frac{\partial u}{\partial z} = \frac{\partial v}{\partial z} = 0$), and no penetration through the upper boundary was prescribed ($w = 0$). The lower boundary had no-slip boundary conditions ($u = v = w = 0$). To prevent the scalar from re-entering the domain, in-flow and out-flow boundary conditions were set on the lateral boundaries. On the east and north boundaries, Dirichlet boundary conditions were set to simulate in-flow, and on the west and south boundaries Neumann conditions were set to simulate out-flow.

In LES, effects of the kinematic viscosity are neglected effectively resulting in simulations with very large Reynolds number ($\mathrm{Re} = \frac{U\,\delta}{\nu}$, where U is the velocity at the top of the domain, δ is the domain height and ν is the kinematic viscosity). In this case, the flow near the wall (the lower boundary) remains unresolved and the surface fluxes of momentum and scalars are modeled using the Monin-Obukhov similarity theory (Wyngaard, 2010).

5.2.1 Numerical experiments

The numerical experiments were designed to replicate the study of Nironi et al. (2015). They performed a plume dispersion experiment in which they released scalar plumes into a neutrally stratified turbulent channel flow. Plumes were released from two heights: 0.06δ and 0.19δ (where δ is the depth of the boundary layer).

To study Reynolds-number dependency, we set up a series of five DNS experiments with Re_τ ranging from 316 to 1862. Additionally, two LES experiments with fine and coarse resolution were performed. For simplicity, the experiments were set-up following the turbulent channel DNS study of Moser et al. (1999), where we cut off the upper half of the domain and enforce a free-slip boundary condition at the top to reduce computational costs. In all DNS experiments, the flow was forced by a constant pressure gradient between

the left and right boundaries, resulting in mean bulk wind speed of $U_{B,DNS} = 0.11$ m s^{-1}. All simulations had the same domain size $15.7\,\delta_D \times 3.9\,\delta_D \times \delta_D$, where $\delta_D = 0.8$ m is the domain height. The different Re_τ were achieved by changing the kinematic viscosity ν. All simulations were first run for 3600 s to achieve statistical stability. After this spin-up, two sources of passive scalars were added into the domain at $0.06\delta_D$ and $0.19\delta_D$. The sources were added in the form of 3D Gaussians with σ_s being the size of one grid box. As a consequence, the size of the sources were resolution dependent. The simulations were continued for another 3600 s.

The two LES runs were performed on a domain size of $15.36\,\delta_L \times 3.84\,\delta_L \times \delta_L$, where $\delta_L = 800$ m. The flow was forced by a constant pressure gradient between the right and left domain boundaries resulting in a mean bulk wind speed $U_{B,LES} = 4.325$ m s^{-1}. As previously mentioned, the second order Smagorinsky model was used for the sub-grid parametrization and the value of the Smagorinsky constant c_s was set to 0.16. The simulations were run for 28800 s to achieve statistical stability of the flow. After that, two sources in the shape of 3D Gaussians were placed at $0.06\delta_L$ and $0.19\delta_L$ like in the DNS, after which the simulations were run for another 3600 s. The specifics of the DNS and LES runs are given in Table 5.1.

5.3 Results

5.3.1 Turbulent velocity fields

First, we provide an overview of the velocity statistics in all the numerical experiments compared to the data from Nironi et al. (2015). Figure 5.1 shows vertical profiles of the first three statistical moments. The profiles were acquired by spatially averaging velocity components in both horizontal directions in a given timestep and temporally averaging 60 profiles over the course of the simulations. From Fig. 5.1 a, it can be observed that in the lower part of the boundary layer (up to $\approx 0.4\,\delta$, $\delta = \delta_D$ or δ_L depending on the discussed experiment) the mean u wind profiles from DNS converge to the profiles from the Nironi experiment with increasing Re_τ. In the upper part of the domain the profiles from the experiment diverge from the DNS profiles. However, the experimental data also disagrees from the logarithmic profile expected in surface layers (e.g. Wyngaard (2010)):

$$\frac{\overline{u}}{u_*} = \frac{1}{\kappa} \log \frac{z-d}{z_0} \tag{5.1}$$

computed using the friction velocity $u_* = 0.185$ m s^{-1}, roughness length $z_0 = 1.1 \cdot 10^{-4}$ m and the displacement height $d = 0.0129$ m taken from the Nironi et al. (2015) experiment. The departure from the log law occurs on the interface of the inner region of the wall bounded flow and the region dominated by the free-stream velocity, U_∞ above it (Coles, 1956; Krug et al., 2017). The Nironi et al. (2015) data is well described by adding a wake

Table 5.1: Overview of the performed simulations.

Run	Resolution	Domain size	σ_s	u_*	Re_τ	ν
DNS	$1056 \times 264 \times 168$	$15.7\,\delta_D \times 3.9\,\delta_D \times \delta_D$	$0.015\,\delta_D$	$6.54 \cdot 10^{-3}$	316	$1.65 \cdot 10^{-5}$
DNS	$1536 \times 384 \times 240$	$15.7\,\delta_D \times 3.9\,\delta_D \times \delta_D$	$0.01\,\delta_D$	$6.14 \cdot 10^{-3}$	489	$1 \cdot 10^{-5}$
DNS	$1536 \times 384 \times 240$	$15.7\,\delta_D \times 3.9\,\delta_D \times \delta_D$	$0.01\,\delta_D$	$5.97 \cdot 10^{-3}$	637	$7.68 \cdot 10^{-6}$
DNS	$3072 \times 768 \times 240$	$15.7\,\delta_D \times 3.9\,\delta_D \times \delta_D$	$0.005\,\delta_D$	$5.54 \cdot 10^{-3}$	1118	$3.97 \cdot 10^{-6}$
DNS	$3072 \times 768 \times 240$	$15.7\,\delta_D \times 3.9\,\delta_D \times \delta_D$	$0.005\,\delta_D$	$5.33 \cdot 10^{-3}$	1862	$2.31 \cdot 10^{-6}$
LES	$1536 \times 768 \times 144$	$15.6\,\delta_L \times 3.9\,\delta_L \times \delta_L$	$0.005\,\delta_L$	0.204 [m s^{-1}]	∞	$1 \cdot 10^{-5}$
LES	$768 \times 384 \times 77$	$15.6\,\delta_L \times 3.9\,\delta_L \times \delta_L$	$0.02\,\delta_L$	0.213 [m s^{-1}]	∞	$1 \cdot 10^{-5}$

function to the log law profile (Fig. 5.1 a), so the mean velocity profile takes the shape (Pope, 2000):

$$\frac{\overline{u}}{u_*} = \frac{1}{\kappa}\left(\log\frac{z-d}{z_0} + 2\Pi\sin^2\frac{\pi z}{2\delta}\right) \tag{5.2}$$

where Π determines the strength of the wake, or the deviation from the log law, here taken to be $\Pi = 1$. In Nironi et al. (2015) the velocity profiles were approximated by a power law. As previously mentioned in section 5.2.1, the DNS experiments in this study were set-up as turbulent half-channel flows, therefore the free-stream layer never developed above the surface layer. For this reason, we find no deviation from log law in the simulated DNS profiles.

The two profiles from the LES experiments are also shown in Fig. 5.1 a. Here, the dependency of the profiles on the spatial resolution is clearly visible. The overshoot visible in the mean velocity profile for the lower part of the domain has been identified in the literature as a combination of the SGS model used, grid resolution, and the wall model used (Brasseur & Wei, 2010; Ercolani et al., 2017; Ardeshiri et al., 2020). As with the DNS experiments, the LES experiments represent only the surface layer.

Figure 5.1 b – d show variances for the three wind components. Excellent agreements between both DNS and LES and the wind tunnel data in for the u component can be seen in Fig. 5.1 b. The convergence of DNS with increasing Re_τ towards the data is also visible. Some differences between the numerical experiments and the data are visible in the cross-wind direction v. Nironi et al. (2015) also noticed a difference between their data and data from a wind tunnel experiment of Fackrell & Robins, (1982a) that fitted better with the LES described in Ardeshiri et al. (2020). Good agreement is found for the covariance (Fig. 5.1 e) which attained the expected linear profile. Similarly, good agreements are found for the triplet covariances (Fig.5.1 f – g).

Figure 5.2 shows production (P) and dissipation (ϵ) of turbulence kinetic energy (TKE). A very good agreement is found for the production term (Fig.5.2 (a)) for both DNS and LES. However, discrepancies in the dissipation term can be noticed (Fig.5.2 (b)). All the DNS experiments (apart the one with the lowest $\mathrm{Re}_\tau = 313$) collapse onto the same line that deviates slightly from the experimental data. A small disagreement was also found for ϵ by Nironi et al. (2015) when they validated their data against Fackrell & Robins, (1982a), with the latter study reporting slightly lower values. LES experiments underestimate ϵ more noticeably, differing also from the DNS. This can be attributed to the numerical effects in the sub-grid dissipation term. As thoroughly discussed in Ardeshiri et al. (2020), for an LES to be considered sufficiently resolving the flow, at least 80% of the TKE needs to be fully resolved (Pope, 2000). This is possible only above the surface where numerical dissipation is an important contributor to the total dissipation. In the MicroHH code, as well as in the PALM code used by Ardeshiri et al. (2020), the dissipation in LES is calculated as a residual of the TKE budget, and therefore includes

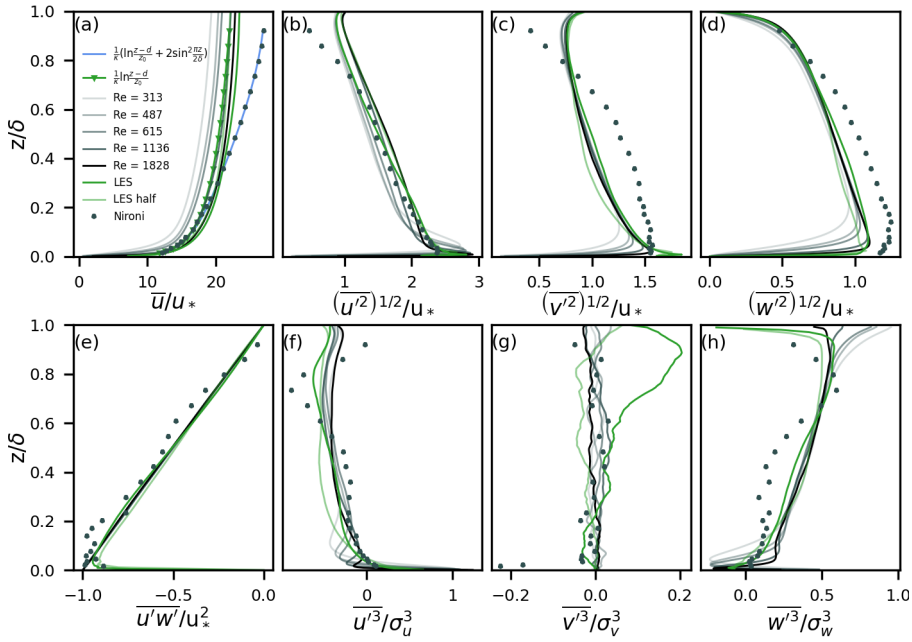

Figure 5.1: (a) Mean wind speed profile, green line indicates the law of the wall with u_* from Nironi et al. (2015). (b) – (d) Variances of three wind components, (e) Reynolds stresses and (f) – (g) triplet correlations.

the numerical dissipation in the total dissipation term.

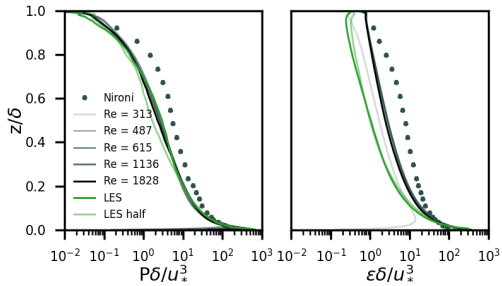

Figure 5.2: (a) TKE production, (b) dissipation of TKE. For the LES experiments the dissipation term is calculated as the residual of the TKE budget.

Figure 5.3 shows time averaged spectra of the vertical velocity at the lower emission height (Fig. 5.3 (a) 0.06δ) and at half of the domain height (Fig. 5.3 (b) 0.5δ). The spectra have been calculated from 1800 samples and have been normalized with the boundary layer height δ and the friction velocity u_*. For DNS, a clear dependence of the spectra on Re_τ is visible. For the low Re_τ there is no clear distinction between the dissipative range and the energetic range of eddies. However, for the two DNS experiments with the highest Re_τ an inertial subrange exists that follows the $k^{-\frac{5}{3}}$ power law, k being the wave number. It is visible that this subrange spans the largest range of wavenumbers for the simulation with the highest Re_τ. Similarly, a short inertial subrange is visible for the LES with the higher resolution, while the low resolution LES is clearly under-resolved.

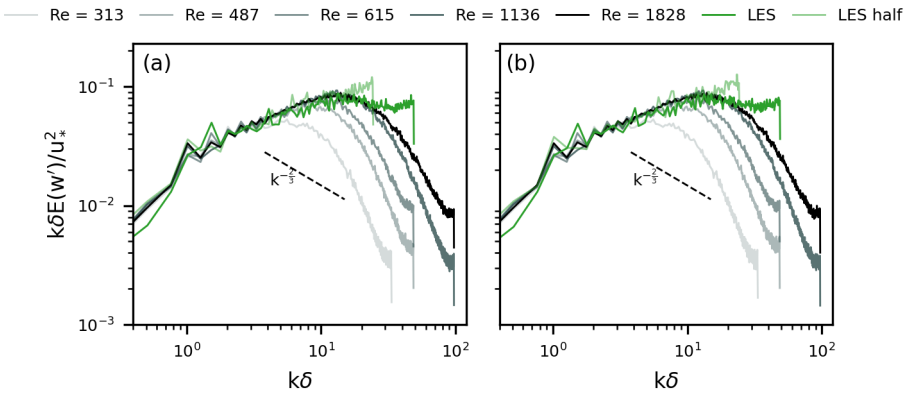

Figure 5.3: Spectra of vertical velocity component w for all performed simulations. Spectra are shown at two distances from the wall (a) height of the lower source $0.06\,\delta$ and (b) the middle of the domain $0.5\,\delta$. For comparison, the power-law function of the wave number $k^{-\frac{2}{3}}$ is also shown.

5.3.2 Plume statistics

To illustrate the effect of the Reynolds number on plume dispersion, Fig. 5.4 shows a snapshot taken over the x–z transect at the y position of the source for all five DNS experiments and the higher resolution LES. The visual differences between the DNS experiments are immediately noticeable. With the increasing Re_τ the structures in plumes show more detail on the smaller scales.

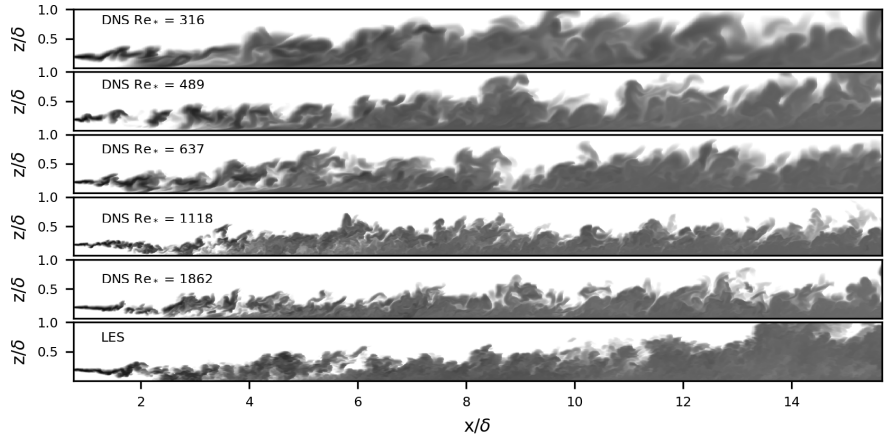

Figure 5.4: Snapshot of x-z transect through the plume emitted from 0.19δ. Figure shows all the DNS experiments and the higher resolution LES.

Concentration statistics

Similarly as in Section 5.3.1, we present here a comparison of the first four statistical moments for the plume concentration for all simulations with the observed concentration statistics from Nironi et al. (2015).

Before we present our results, we provide a short overview of the appropriate scaling we employed on the concentration fields and of the definitions of statistical moments and length-scales used here to ensure comparability of experimental data with results from DNS and LES.
Firstly, we followed scaling form Nironi et al. (2015), in which the scaled concentrations are given as $c^* = c\frac{u_\infty \delta^2}{Q}$, where c is the measured concentration, u_∞ is the free-stream velocity, or here the velocity at the top of the boundary layer, Q is the emission strength, and δ is the boundary layer height.
Secondly, the first moment, or the mean, is given as $C^*(x,y,z) = \frac{1}{N}\sum_{i=0}^{N} c_i^*(x,y,z)$, where N is the total number of time-samples, in this case 2600, and c_i^* is the concentration sampled at a certain time i. All the higher moments are defined as $m_n^* = \left[\frac{1}{N}\sum_{i=0}^{N}\left(c_i^* - C^*\right)^n\right]^{\frac{1}{n}}$, where n is the order of the statistical moment.
Lastly, as can be seen from Fig. 5.1 a, there are differences in the mean wind between the respective simulations and the experiment. To be able to compare the plumes across the simulations with the experiment, an effective distance of the plume from the source, x_*, can be found. x_* is defined as the distance from the source, x, scaled by the eddy overturn distance X:

$$x_* = \frac{x}{X} = \frac{x}{\overline{u}\,T} = \frac{u_*\,x}{\overline{u}\,\delta}, \tag{5.3}$$

where T is the characteristic eddy overturn time and all the other terms are as in the previous section. Therefore, a downwind distance from the source in a respective simulation, x_{sim}, can be found at which the plume is mixed an equal amount of time compared to the experiment at a downwind distance x_{exp}

$$x_{sim} = \frac{u_{*,exp}}{u_{*,sim}}\frac{\overline{u_{sim}}\,\delta_{sim}}{\overline{u_{exp}}\,\delta_{exp}}\,x_{exp}. \tag{5.4}$$

Vertical profiles of mean concentration fields from both the high (top row) and the low (bottom row) source are shown in Fig. 5.5. The results are given at four downwind distances from the source $x/\delta = [0.3125,\ 0.625,\ 1.25,\ 2.5]$. It is evident that, for most of the simulations, results agree very well with the data. For the higher source the only notable disagreement is visible for the low resolution LES, which overshoots the centerline concentrations. We speculate this is a consequence of the simulation being under-resolved (Fig. 5.3) as there are no small-scale structures in the simulation than can disperse the plume around its centerline. Similarly, for the lower source, the DNS with the lowest Re_τ overshoots the centerline values on all distances from the source. This is due to the lower source being emitted at the edge of the viscous layer for the DNS with $\mathrm{Re}_\tau = 313$. It is clear that mixing even at low to moderate Re_τ is sufficient to capture the mean plume growth well, if the distance of the plume from the viscous layer is sufficient.

To focus on higher order statistics, Fig. 5.6 shows horizontal profiles for all four central moments, raised to the power of $\frac{1}{n}$, $n = [1,\ 2,\ 3,\ 4]$, respectively, for both high (left

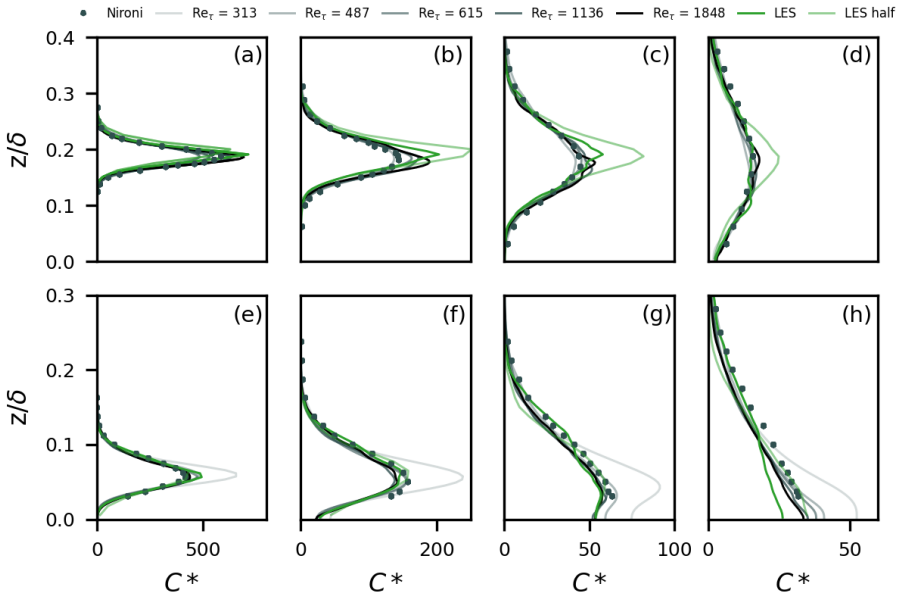

Figure 5.5: Vertical profiles of mean concentration, C^*, in all the simulations (DNS and LES) compared to Nironi data. Profiles are given for the higher (top row) and lower (bottom row) emission source at distances: (a) & (e) $x/\delta = 0.3125$, (b) & (f) $x/\delta = 0.625$, (c) & (g) $x/\delta = 1.25$, (d) & (h) $x/\delta = 2.5$.

column) and low (right column) plumes. Similarly as for the previous figure, the mean plume is well captured in the horizontal (Fig. 5.6 (a), (e)). However, the discrepancies between the results from simulations and the experiment become more obvious as the order of moments increases. Depending on the source height, the moments are either better reproduced by the LES experiments while DNS overestimates centerline values (Fig. 5.6 (f), (g), (h)) or the higher Re_τ DNS better reproduce the data while LES underestimates values on the sides of the plume (Fig. 5.6 (b), (c), (d)). Notable is the deteriorating smoothness of profiles with the increasing moment. The number of samples averaged here (2600 samples) was obviously not large enough to smooth out the influence of outliers completely since their influence increase with the order of the statistical moment. Furthermore, the role of Re_τ on the higher order statistics is clearly visible, especially for the higher source. The convergence to the most turbulent DNS profiles ($\mathrm{Re}_\tau = 1136$ and 1848) is clear in profiles for standard deviation, skewness and kurtosis. Similarly for LES, the mean scalar field is rather insensitive to grid resolution, while concentration fluctuations are more sensitive to resolution. This effect was also noted in the LES study described by Ardeshiri et al. (2020). For the higher source, the integral length scales are larger than for the lower source. Logically, as one approaches the surface the size of motions that can displace the plume reduces resulting in less intense fluctuations closer to the surface.

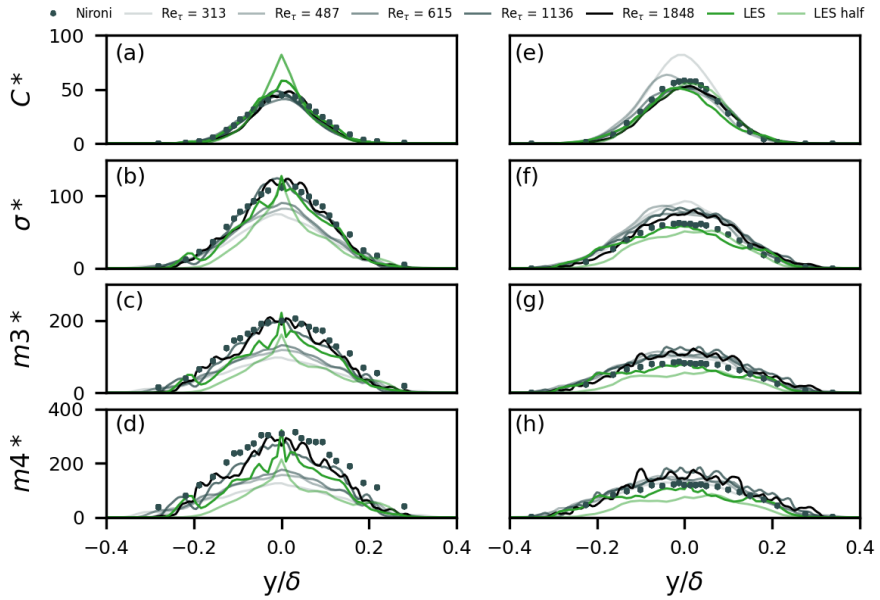

Figure 5.6: Horizontal profiles of the first four central moments, raised to the power of $\frac{1}{n}$, n = [1, 2, 3, 4], respectively, of concentration in all the simulations (DNS and LES) compared to Nironi data. Profiles are given for the higher (left column) and lower (right column) emission sources at distance $x/\delta = 1.25$. The panels show: (a) & (e) mean concentration, (b) & (f) standard deviation, (c) & (g) skewness and (d) & (h) kurtosis.

Fig. 5.7 shows centerline concentration statistics for the higher source on six downwind distances. For the mean concentration C^* (Fig. 5.7 a), all the simulations, apart from the low resolution LES, show very good or excellent agreement with the experiment. The highest Re_τ DNS is in exact agreement with the experiment throughout the domain, while the high resolution LES starts to slightly underestimate the mean concentration very far from the source. For the three higher moments (Fig. 5.7 b–d), however, the value closest to the source is underestimated in all simulations. In contrast, mid-distances are well represented in all simulations, and far from the source high resolution LES agrees with the experiment well, while the DNS experiments overestimate the values. The overestimate of DNS with the data grows as the distance from the source increases and as the order of the moment increases. Similar results were found for the lower plume (not shown). This could be the low Re number artifact: with the downwind distance from the source the range of eddies that can entrain fresh air into the plume grows as the diameter of the plume grows. For too low Re flows in DNS the mixing inside the plume itself is underestimated and there still remain areas with too high concentrations that have a notable influence, specifically on the higher-order moments.

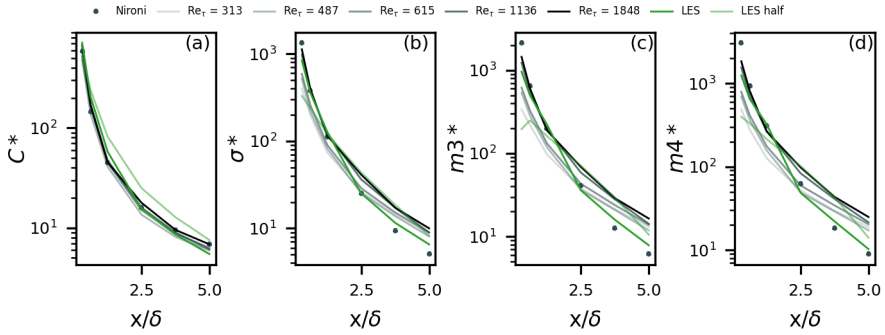

Figure 5.7: Centerline values of the first four statistical moments in the simulations (DNS and LES) and the Nironi data. The panels show: (a) mean concentration, (b) standard deviation, (c) skewness and (d) kurtosis.

5.3.3 Absolute and relative dispersion

Processes that drive plume dispersion can be separated into two mechanisms, which relate the size of the plume to the size of the dominant eddies. First, the plume is displaced around its mean centerline by eddies larger than the plume itself. This is known as meandering motion. And second, the plume is spread relative to its instantaneous center of mass position by eddies smaller than the plume. These two mechanisms contribute to the absolute plume spread $\sigma_{x_i,a}$ (also known as the dispersion coefficients) as

$$\sigma^2_{x_i,a} = \sigma^2_{x_i,m} + \sigma^2_{x_i,r}, \tag{5.5}$$

where $\sigma_{x_i,m}$ and $\sigma_{x_i,r}$ represent plume spread by meandering and relative dispersion and x_i = (y, z) is the plume spread direction. These motions can be related to the plume center of mass:

$$x_{i,m} = \frac{\int c(x,y,z,t)\, x_i \, dy\, dz}{\int c(x,y,z,t)\, dy\, dz}, \tag{5.6}$$

as

$$\sigma^2_{x_i,m}(x,t) = \frac{\int c(x,y,z,t) \cdot (x_{i,m} - \overline{x_{i,m}})^2 \, dy\, dz}{\int c(x,y,z,t)\, dy\, dz}, \tag{5.7}$$

$$\sigma^2_{x_i,r}(x,t) = \frac{\int c(x,y,z,t) \cdot (x_i - x_{i,m})^2 \, dy\, dz}{\int c(x,y,z,t)\, dy\, dz}, \tag{5.8}$$

where $\overline{x_{i,m}}$ is a time average of all instantaneous plumes centers of mass, and x_i is the in-plume position.

Figure 5.8 shows the three dispersion coefficients for the source at 0.19δ in the y (left column) and z (right column) directions. Reynolds number dependence is visible for the DNS plumes. The absolute width of the plumes in the y direction decreases as the Re_τ number

increases (Fig. 5.8 (e)), especially further away from the source. When the dispersion is decomposed into the two separate processes, it is visible that the relative plume dispersion is larger for less turbulent flows (Fig. 5.8 (e)). Ardeshiri et al. (2020) showed in their LES study that most of the production of scalar variance occurs close to the source, where meandering is dominant. Since lower resolution simulations effectively imply larger source size, as simulated source size is determined by the grid-size, this artificially increases the relative dispersion through numerical diffusion and damps meandering. Differences in the meandering plume growth are less pronounced (Fig. 5.8 (c)). Meandering is also of lower magnitude than the relative dispersion, therefore its influence is less pronounced in the absolute plume. This is especially true further downwind from the source (e.g. Gifford (1959)). For the vertical plume growth, the differences between the simulations are less pronounced and Re_τ convergence is not as clear (Fig. 5.8 (b),(d),(f)).
The LES plumes agree with the highest Re_τ DNS in the y direction very well. In the z direction, the low resolution LES underestimates the absolute plume growth by a large margin (Fig. 5.8 (b)). We attribute this to the very low resolution of this simulation in the vertical direction.

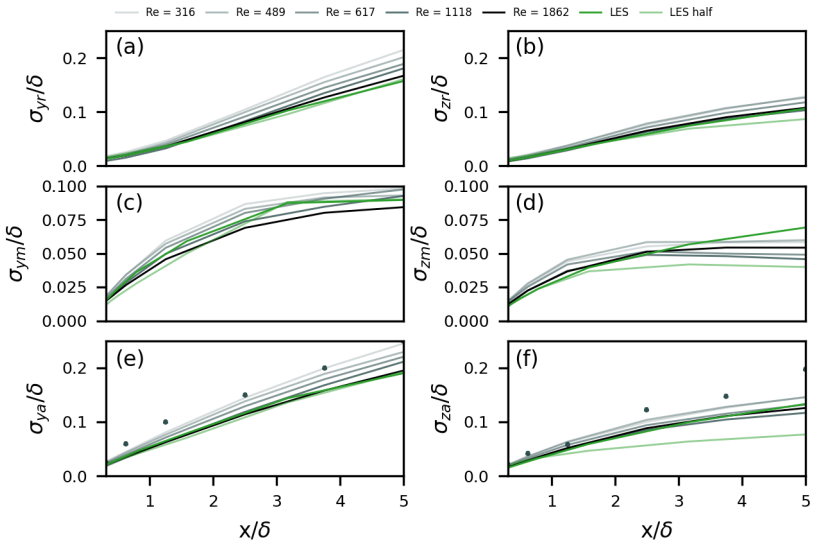

Figure 5.8: Dispersion coefficients for the plume emitted from 0.19δ. The left column gives dispersion coefficients in y direction for: (a) relative dispersion, (c) meandering, and (e) absolute dispersion. The right column shows the vertical dispersion coefficient for: (b) relative dispersion, (d) meandering, and (f) absolute dispersion.

5.4 Discussion

This paper presents point source plume dispersion in five direct numerical simulations (DNS) with different Reynolds numbers and different resolutions. Furthermore, for comparison, a high- and low- resolution large eddy simulation (LES) were also conducted.

The goal of this study was to see if the Reynolds number similarity occurred in the DNS for the first four statistical moments as this would prove the method viable for dispersion studies. In contrast to LES, DNS does not parametrize any part of the turbulence. For this reason, we added LES to compare their performance on different downwind distances from the source. The simulations have been set-up according to the wind channel experiment of Nironi et al. (2015) in which point source plumes where released from different altitudes into a neutral turbulent flow.

The analysis of the velocity fields indicates that the mean field but also the Reynolds stresses and triplet covariances show good agreement with the experimental results. The Reynolds number dependence in the mean wind speed profiles from DNS is clear and the higher Re_τ simulations converge to the expected log-law. However, there is some discrepancy with the profiles from the experiment in the upper part of the boundary layer. This discrepancy is well-described by implementing the law-of-the-wake correction (Pope, 2000) to the standard log-law. As pointed out in Pope (2000) this correction is applied on the interface of the free-stream layer and the surface layer since there is no sharp transition between the two layers. The simulations, however, represent purely the surface layer flow. Wind variances show excellent agreement with the experiment in all of the simulations for the along mean wind component. For the cross-wind components, which are most important for the dispersion, the variances are somewhat underestimated in all simulations and in both directions.

The mean concentration field is in good agreement with the wind tunnel experiment in almost all simulations. Only the lowest $\mathrm{Re}_\tau = 313$ DNS and low resolution LES show significant disagreement with the experimental data. This result indicates that the processes driving the mean plume dispersion are well represented even in low to moderate Reynolds number flows. The situation is different for the concentration variance. The simulations with low Re_τ clearly show underestimation of scalar variability. However, the two most turbulent DNS experiments ($\mathrm{Re}_\tau = [1118, 1862]$) converge to the same values. On the transect used in Fig. 5.6 ($x/\delta = 1.25$) the results convergence to the wind tunnel data. Similar behaviour is seen for the other two higher order moments (skewness and kurtosis). LES also shows very good agreement with the wind tunnel data. From the centerline values of the four moments it is visible that the mean concentration is well represented in all simulations apart from the low resolution LES. The three higher moments are better described by DNS close to the source, while in the far field LES reproduces the data better while DNS shows overestimates. We speculate that this is caused by the low Reynolds number effect. Conversely, the poorer performance of LES in the close-source range can be ascribed to LES being too dispersive. In the LES, the effects of the smallest eddies (smaller than the cut-off frequency) are modelled by the subgrid models. Our results suggest that this parametrization smooths out the concentration fluctuations that are present very close to the source, which is not the case in the DNS experiments. A possible way to circumvent this issue in LES would be to develop a subgrid

parametrization that changes with downwind distance from the source.

The mechanisms that drive concentration fluctuations can be analysed by separating the plume dispersion into meandering and relative dispersion. Generally, the DNS with the highest Re_τ number and the high resolution LES show very similar results, showing that the DNS is capable of reproducing the mean drivers of dispersion, either close to the source through meandering or further away from the source through relative dispersion, at least as well as LES. Notable is the Reynolds number dependence of relative dispersion, especially further downwind. Ardeshiri et al. (2020), in their LES study, stressed the importance of properly resolving the source in order to avoid artificial damping of meandering through enhanced relative dispersion due to numerical effects. This effect can be noticed in our DNS results since we use three different resolutions. However, for example, the DNS runs with Re_τ 1118 and 1862 use the same resolution, but there is still a difference in the plume width, indicating that the Reynolds number of the flow may also explain part of the differences in plume widths.

A notable drawback of DNS when performing the dispersion studies is the too high viscous layer that makes the study of dispersion close to the ground level impossible. The height of the viscous layer is Reynolds number dependent and for simulations with too low Re this effect can influence the plume at altitudes as high as 10 % of the boundary layer height (Fig. 5.5). It is however impossible to achieve the depth of the viscous layer present at the atmospheric conditions (height of millimeters) in DNS studies. Therefore, these effects should be taken into account when designing dispersion experiments.

We have shown Reynolds number convergence in DNS experiments for velocity and scalar fields. The most turbulent DNS results are equally good, or in some cases better than the corresponding LES. Apart from the obvious advantage of DNS of not having any parametrizations and resolving all relevant scales of motion, the computation cost and ease of set-up should also be taken into the account. The latter is relevant for LES as it is notorious difficult to correctly set up LES for neutral channel flows. LES is sensitive to the wall model used (Ardeshiri et al., 2020), the choice of the sub-grid model and its constants, and the choice of resolution. As a consequence, it is possible to either over- or under-resolve mixing in the simulation (Brasseur & Wei, 2010). Furthermore, in LES it takes long for the statistics to become stationary. In our case, stationarity was archived only after 28800 timesteps. The computation costs, including a simulation hour with the plumes active, amounted to 2592.5 CPU hours. DNS is also very computationally expensive, but that cost increases exponentially with the Reynolds number (Pope, 2000). For the most turbulent DNS, the cost amounted to 6880 CPU hours, i.e. more than double the LES costs, but not prohibitive.
In conclusion, we showed that DNS performs well for point source plume dispersion studies. With the constant increase in computing power we expect DNS to become more feasible in the atmospheric studies in general.

Chapter 6

Plume dispersion in a residential street

Abstract

This study uses direct numerical simulations in a mock urban setting to test the performance of a semi-empirical methane source strength estimation method – the Weller method. The study is based on a measurement day during a campaign in Hamburg, Germany where methane emissions from various ground sources in the city were measured. The topography in the simulation was set-up to mimic the residential street in Hamburg where the measurements were taken. Based on the street layout, 11 point sources were placed on the ground in different positions relative to the buildings that appeared to be the sources of methane. Due to the lack of meteorological measurements from the campaign, this study is performed in a neutral atmosphere with constant mean wind direction aligned with the street. Three Direct Numerical Simulation (DNS) experiments with three different Reynolds numbers were performed, two of which had the same mean wind speed and in the third the wind speed was doubled. For all three simulations the mean vertical profiles of the first three statistical moments of velocity are very similar. There is a clear influence of the buildings on the flow field as the re-circulation of air behind the buildings can be clearly distinguished in the velocity fields and in the pressure build-up on the windward side of the buildings. This has direct influence on plumes as they tend to stay trapped in the spaces between the buildings. The estimation using the Weller method was separated in two parts: 1) determining the source location and 2) estimation of the source strength. The results show the method places the source at the wrong location unless the measurements were taken directly on top of the source. The source strength is estimated correctly by the method only if measurements are taken on a distance at which the maximum concentration satisfies the equation the method is based on. We found that this distance depends on atmospheric stability and the mean wind speed. If the measurements are taken at the right distance from the source, at least 10 transects are still needed to average out the atmospheric variability and to estimate the source strength within 40% of the true emission.

6.1 Introduction

Methane (CH_4), one of the most important green-house gases (GHG), is of both anthropogenic and natural origin. In a recent study, Saunois et al. (2020) reported that 60% of total global CH_4 emissions can be attributed to anthropogenic origin. These sources can be traced to a large variety of human activities, ranging from transport and energy supply to agriculture and waste management. Cities, as hot-spots of human activity, also contribute to the total methane budget. However, their contribution is still not well quantified (Plant et al., 2022). Furthermore, it is expected that by 2030 60% of global human population will reside in cities (Plant et al., 2022) making the quantification of city emissions even more pressing.

Recently, Plant et al. (2022) used data collected by the TROPOMI instrument on the Sentinel-5 Precursor satellite to show that there is likely an under-representation of city emissions in the emission inventories. They also indicated the usefulness of satellite data for deriving more accurate global city emission estimates. However, due to their resolution, satellites are not able to identify individual sources in cities. For this purpose, a ground-based approach of measuring methane emissions, such as devices placed on mobile platforms (e.g Maazallahi et al. (2020)), are better suited since they are capable of identifying individual point sources at street level. Recently, Alvarez et al. (2018) measured fugitive emissions from the oil and gas industry supply chain in a number of US cities that account for 30% of total U.S. methane emissions. They have found 2.3% of gross annual U.S. gas production escapes to the atmosphere only through the supply chain, which is about 60% higher than the previous estimate. Therefore, identifying the highest emitters on street level is of high priority in order to achieve quick mitigation of methane emissions from cities.

The methods used to infer emission strengths from street sources, however, are often based on very simple empirical or semi-empirical models. An example is the Gaussian plume model (GPM) used to estimate emissions from larger facilities such as landfills and wastewater management facilities (Maazallahi et al., 2020). This potentially leads to large estimation errors even for plumes dispersing over a terrain with no obstacles (e.g. Yacovitch et al. (2015); Caulton et al. (2018); Ražnjević et al. (2022)). Another estimation method, and the one most relevant to the problem of fugitive street-level emissions, was developed by Weller et al. (2019). This method estimates emissions based on longitudinal street transects through methane plumes combined with an empirical model that was calibrated to a release experiment.

As previously mentioned, using simple models can potentially lead to large estimation

errors, even in the simple case of dispersion over flat terrain. This is due to the turbulent nature of the plume very close to the source (e.g. Caulton et al. (2018); Ražnjević et al. (2022)). On top of that, in case of emissions from street geometries, the presence of obstacles affects the turbulent flow, and consequently the plume itself, changing the mean flow profiles (Barlow & Coceal, 2009) and dictating the plume behavior (Mavroidis & Griffiths, 2001; Coceal et al., 2014).

The dispersion of plumes released from point sources has been a topic addressed in several previous studies. Since a city plume is heavily influenced by the configuration of the nearby buildings, a comprehensive study on dispersion is nearly impossible to conduct (Coceal et al., 2014). Therefore, the majority of studies focused on dispersion in Mock Urban Setting Tests (MUSTs) that represent a generic urban setting that is easily reproducible and the main parameters are easily controllable (street width, building height and width, main wind direction, placement of the sources with respect to the buildings etc.). Experimental approaches addressing this problem involved wind tunnel experiments with MUST set-up. For instance, Davidson et al. (1995) studied dispersion in an uniform array of buildings under neutral atmospheric conditions and found that the vertical extent of the plume was 40–50% larger than if no obstacles would be present. Similarly, Macdonald et al. (1997) compared the plume from a wind tunnel experiment with the GPM and found that the lateral dispersion is increased by the presence of an urban array. Furthermore, they showed that the narrowness of streets increases the lateral dispersion. Recently, Carpentieri & Robins (2015) studied the influence of urban morphology on the mean wind profiles. They showed that wind profiles are influenced by the building height variability, the building aspect ratio, the angle between the street canyon and the incoming wind, and the presence of much taller buildings in an array of relatively uniformly high buildings. Consequently, since the plume dispersion is primarily driven by the wind, all these morphological features influence the plume dispersion.

A number of studies conducted dispersion experiments in MUST settings with numerical models. We address here Reynolds-averaged numerical simulations (RANS), direct numerical simulations (DNS) and large-eddy simulations (LES). RANS models solve the governing equations of motion (momentum, mass and energy) only for the mean values of these variables, while they fully parameterize turbulent motions. The advantage of these models is their low computational cost relative to the models that fully or partially resolve turbulence. This allows for repeated comprehensive studies that include all three atmospheric stability conditions (neutral, stable, unstable) such as the study of Guo et al. (2020). However, for studying the fluctuating behavior of plumes, models that partially (LES) or fully (DNS) resolve turbulence are needed. Philips et al. (2013) studied the influence of building array configurations on the plume dispersion under neutral atmosphere in an LES and found that lateral dispersion is more affected by

the buildings than vertical dispersion, thus confirming the wind tunnel experiment of Macdonald et al. (1997). Urban dispersion under stable conditions has been studied by Li et al. (2016). They found that the flow generally slows down in an urban array in a stable atmosphere, effectively hindering plume mixing above the canopy and situating the plume close to the ground. Michioka et al. (2019), also in an LES, showed that fluctuations in the mean wind variance have virtually no effect on the plume deeper into the urban array and can be observed only in the first few rows of buildings. Finally, for DNS, studies mostly focused on dispersion in neutral conditions. DNS studies mostly point to a large influence of the buildings on plumes, indicating larger lateral spread, pooling of plumes on the lee side of buildings, and channeling of wind between buildings if there is an angle between the incoming wind and the street canyon (see Branford et al. (2011); Coceal et al. (2014); Castro et al. (2017); Eisma et al. (2018); Goulart et al. (2018))

Our aim for this study is to assess source strength estimation methods from street level measurements using DNS. The measurement strategy we are focusing on was first developed by Weller et al. (2019) and has recently been used to detect and estimate fugitive methane emissions (Maazallahi et al., 2020, 2022). To the best of our knowledge, this estimation method has not yet been systematically tested for the influence of the atmospheric parameters on the plume variability and consequently the source estimations. We therefore use DNS to simulate dispersion from multiple scalar sources in a MUST set-up. This study is inspired by the measurement campaign of city methane emissions conducted in Hamburg, Germany (Maazallahi et al., 2022). As a first step, we limit this study to dispersion under neutral atmospheric conditions and with the mean wind direction aligned with the street as we expect that the estimation method performs best for this geometry. However, we do vary the mean wind speed in our study to test its influence on the source-strength estimations. Note that the Weller estimation method does not account for wind speed. We also look at the flow characteristic around the buildings and its influence on the plume dispersion.

This chapter is structured as follows: In section 6.2 we shortly describe the Weller method as it is the main focus of this study. Section 6.3 describes one of the residential streets in Hamburg in which Maazallahi et al. (2022) detected methane leaks and which we used to construct an idealized MUST. The numerical model and the numerical experiment set-up are described in section 6.4. The results are presented in section 6.5, first focusing on wind and pressure fields, followed by an analysis of plume fluctuations around buildings. Finally, the last part of section 6.5 is dedicated to a critical reflection on the Weller method.

6.2 The Weller method

This section is used to shortly introduce the leak detection and source estimation method presented in Weller et al. (2019). Here, we do not analyze the technical aspects of the method, such as quality control, and instead focus on the actual algorithm for leak detection and the formula that is used to estimate source strengths.

The Weller method consists of taking methane concentration measurements while driving through city streets. This way large areas of the city can be mapped with methane concentrations in relatively short time. Unlike the sampling methods that take plume transects perpendicular to the mean wind speed and rely on the GPM to infer the emission rate (e.g. Caulton et al. (2018); Ražnjević et al. (2022)), the Weller method makes transects along the street, independent of the wind direction. Furthermore, the authors recommend to take at least 2 transects through the street and averaging them before applying the detection and quantification algorithm. The Weller method provides information on the leak location and the strength of the leak based on the maximum concentration enhancement recorded on multiple street transects.

The leak detection algorithm consists of two steps: peak detection and identification of a leak. When a methane concentration enhancement is observed, the observed peak (OP) location is found as a weighted spatial average of all the elevated readings in the OP as:

$$(X_{OP}, Y_{OP}) = \frac{\sum_{i=1}^{N} c_i \cdot (x_i, y_i)}{\sum_{i=1}^{N} c_i}, \tag{6.1}$$

where X_{OP} and Y_{OP} are spatial coordinates of the derived OP location, c_i is the methane enhancement observed at a measurement location (x_i, y_i) i where i = [1,...,N]. Here it is assumed that all the observed enhancements are caused by the same source.

After P street transects and OP identifications, a leak indication (LI) is conducted. Similarly to locating OPs, LIs are found as a weighted average of maximum concentration enhancements $c_{max,j}$ for each OP location as:

$$(X_{LI}, Y_{LI}) = \frac{\sum_{j=1}^{P} c_{max,j} \cdot (X_{OP,j}, Y_{OP,j})}{\sum_{j=1}^{P} c_{max,j}}, \tag{6.2}$$

where j = [1, P] is the individual OP, ($X_{OP,j}$, $Y_{OP,j}$) is the location of a specific OP, and X_{LI} and Y_{LI} represent the final leak indication location.

Finally, the source strength is estimated using the empirical formula:

$$\ln Q = \frac{\overline{\ln c_{max}} + 0.984}{0.817} \tag{6.3}$$

where Q is the estimated source strength in L min^{-1}, and $\overline{\ln c_{max}}$ (where c_{max} has units of ppm) is an average of maximum concentrations found for each OP i.e. $\overline{\ln c_{max}} = \frac{1}{P}\sum_{i=1}^{P} \ln c_{max}$ where $i = [1, \mathrm{P}]$ is the individual OP.

6.3 Description of the measurement site

This study is based on one measurement day during a campaign conducted in Hamburg, Germany (Maazallahi et al., 2022). The measurement site represents a typical residential street in European suburbs. For this reason, we find it a good starting point to build our MUST on. Figure 6.1 (a) shows a Google Maps view of the measured street. The street is straight with houses placed fairly uniformly along both sides. The Google street view (Fig. 6.1 (b)) provides a better look on the type of houses found in the street. Relatively small family homes can be observed with an approximate aspect ratio of 1. Based on this information, we constructed a simplified version of this street for our simulations that will be presented in the next section of this chapter (section 6.4.1). We would like to point out that, while this street was used as the basis for this study, there were no meteorological variables recorded during the campaign. Therefore, we are unable to reproduce the measurement day accurately and can only approximately compare the measured and simulated plumes.

Figure 6.1: (a) street view, and (b) top view of the measured street as provided in Google Maps. Credit: Google ©.

6.4 Numerical model

The numerical experiment was performed using the MicroHH model, developed by van Heerwaarden et al. (2017). The model solves the conservation equations of energy, mass and momentum under Boussinesq approximation. The dynamics of the system are solved with a second order finite volume scheme. The advection of scalars is advanced with a second-order scheme with a fifth-order interpolation with an imposed flux limiter to

ensure monotonicity. The time is advanced using a Runge-Kutta third order scheme.

For the (u, v, w) velocity components, periodic boundary conditions have been imposed on all lateral boundaries of the domain. On the top of the domain, a free-slip boundary condition was applied to the lateral velocity components ($\frac{\partial u}{\partial x} = \frac{\partial v}{\partial y} = 0$) and there was no penetration through the top of the boundary ($w = 0$). At the surface, a no-slip ($u = v = w = 0$) boundary condition was applied. To prevent the scalar from re-entering the domain Dirichlet boundary conditions were imposed for the in-flow of scalars into the domain, and a Neumann boundary condition was set for the out-flow.

We use square blocks to represent the houses in the simulation. To prevent the flow from entering these blocks, the immersed boundary method (Tseng & Ferziger, 2003) was used. This method consists of ghost cells representing the edges of the buildings (or any other complex boundary) into which pressure and velocity components are extrapolated from the nearby fluid grid cells. The extrapolation is done in such a way that a forcing in the ghost cell is calculated such that the desired boundary condition of no flow through the boundary is satisfied.

6.4.1 Experiment set-up

Numerical experiments were designed to reproduce the atmospheric flow through the street described in section 6.3. For this exploratory study, we assumed neutral atmospheric flow into which we released scalars as a proxy for methane emissions.

All runs we performed had an identical geometric set-up as shown in Fig. 6.2. The domain size in the runs was set to $(x, y, z) = 2\,\pi \times \pi \times 1$ [m] with a spatial resolution $768 \times 384 \times 128$. Similarly to the study in the previous chapter, we employ here Reynolds similarity, therefore the flow in the domain described here will have the same characteristics in a much larger domain (e.g. the actual street) given that the Reynolds number and geometrical ratios (e.g. width vs length of the street, spacing between the houses etc.) stay the same. From this point on, we will describe the geometry in non-dimensional space, which will be achieved by scaling everything with $\delta = 1$ [m], the boundary layer height. The houses in the simulation were represented by rectangles with a horizontal edge length $L = 0.39\delta$ and height $H = 0.35\delta$. The houses are lined uniformly to mimic the street (Fig. 6.2). The distance between each of the houses is taken as $l_x = 1.15H$ in the same row and $l_y = 3.5H$ between two rows of houses (the "street" width). Due to the periodic boundary condition imposed on the velocity components, the geometry in the simulation needs to be axis-symmetric about – and perpendicular to – the mean wind speed (here x and y respectively).

We performed three simulations with different Reynolds numbers; $\mathrm{Re}_\tau = u_*\delta/\nu = [1012, 2532, 5136]$. Here, the friction velocity was defined as $u_* = [(u'w')^2 + (v'w')^2]^{\frac{1}{4}}$ at the buildings' height (Finnigan, 2000), where the Reynolds stresses have their maximum values. The maximum Reynolds stress marks the transition area from the roughness sub-layer flow to the inertial sub-layer flow in which the flows is homogeneous in all directions (Rotach, 2001). The lowest Re_τ simulation was used as the baseline. The increase in turbulence between the first and the second simulation was achieved by lowering the kinematic viscosity ν and keeping all other characteristics of the simulation identical. The second increase in Re_τ was achieved by doubling the bulk wind speed U_B in the second run. The bulk wind speed is imposed by maintaining a constant pressure difference between the left and right boundaries of the domain. The specifics of each simulation are given in Table 6.1. All simulations were first run for 900 time-steps to achieve statistic stability of the flow, after which 11 scalar sources were released into the simulations. The locations of the sources are numbered in Fig. 6.2. The sources were placed on the ground as one grid flux boundary condition with $Q = 1.59 \cdot 10^{-5}$ [kg s^{-1}] released into the simulation in each time-step. The simulations were then run for an additional 3600 time-steps during which cross-sections at multiple locations through the plumes were taken every 5 time-steps.

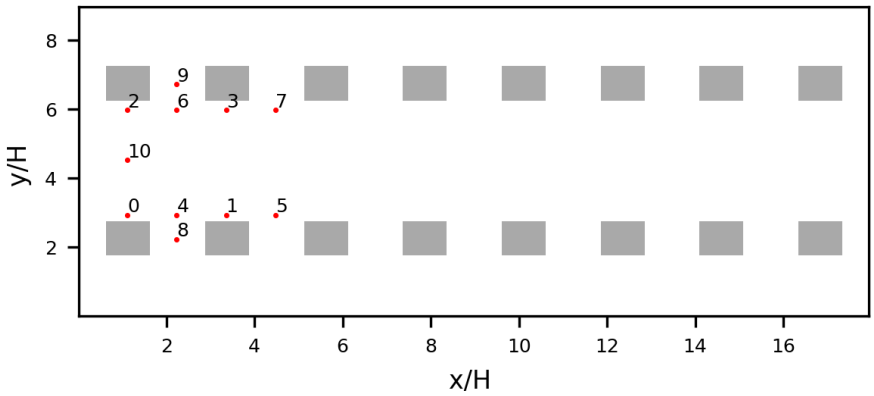

Figure 6.2: The geometric set-up of the simulations. The numbered red dots indicate the locations of the sources.

6.5 Results

6.5.1 Flow and pressure fields

Firstly, we analyse the velocity fields of the simulations. Figure 6.3 shows the vertical profiles of the first three statistical moments for the three velocity components (u, v, w). The profiles are calculated first as horizontal domain averages (averaging over x and y) and

Table 6.1: Numerical experiments characteristics: resolution, domain size, bulk mean velocity, friction velocity, Reynolds number $\mathrm{Re}_\tau = \mathrm{u}_* \delta / \nu$, viscosity.

Run	Resolution	Domain size	U_B	u_*	Re_τ	ν
LowRe	$768 \times 384 \times 128$	$2\pi \times \pi \times 1$	0.11	$1.013 \cdot 10^{-2}$	1012	$1 \cdot 10^{-5}$
HighRe1	$768 \times 384 \times 128$	$2\pi \times \pi \times 1$	0.11	$1.006 \cdot 10^{-2}$	2532	$3.97 \cdot 10^{-6}$
HighRe2	$768 \times 384 \times 128$	$2\pi \times \pi \times 1$	0.22	$2.050 \cdot 10^{-2}$	5071	$3.97 \cdot 10^{-6}$

subsequently as time averages over 60 time-steps spanning over one hour of simulation. For all moments a clear influence of the buildings on the vertical profiles is visible. The mean u velocity profiles (Fig. 6.3 (a)) show an almost linear increase in wind speed with height for the highest Re_τ simulation (green line) from approximately the top of the viscous layer (the layer closest to the surface where velocity is linearly proportional to the distance from the wall) to the top of the buildings. After a discontinuity at the buildings' top, the profile attains the logarithmic profile that is expected in a surface layer flow. It should be noted here that the surface area of the domain covered by the buildings is only $\approx 10\%$ and that the buildings have been grouped together into two rows. Different building configurations or different building densities are expected to yield different velocity statistics (Macdonald, 2000; Kastner-Klein & Rotach, 2004). All the moments, after scaling, converge to the similar profile, showing very little variation with the changing Reynolds number. Only slight differences are visible for the cross-flow and vertical velocity variance (Fig. 6.3 c,d) indicating small changes in turbulent mixing for the lowest Re_τ simulation. This result complies with the previous findings, which suggested there is very low Reynolds number dependency for the flows around sharp-edged obstacles (Castro & Robins, 1977; Snyder & Castro, 2002; Branford et al., 2011) Therefore, for simplicity, all the analysis presented in this chapter will be performed for the simulation HighRe1 (Table 6.1) with $\mathrm{Re}_\tau = 2532$ unless specified otherwise in the text.

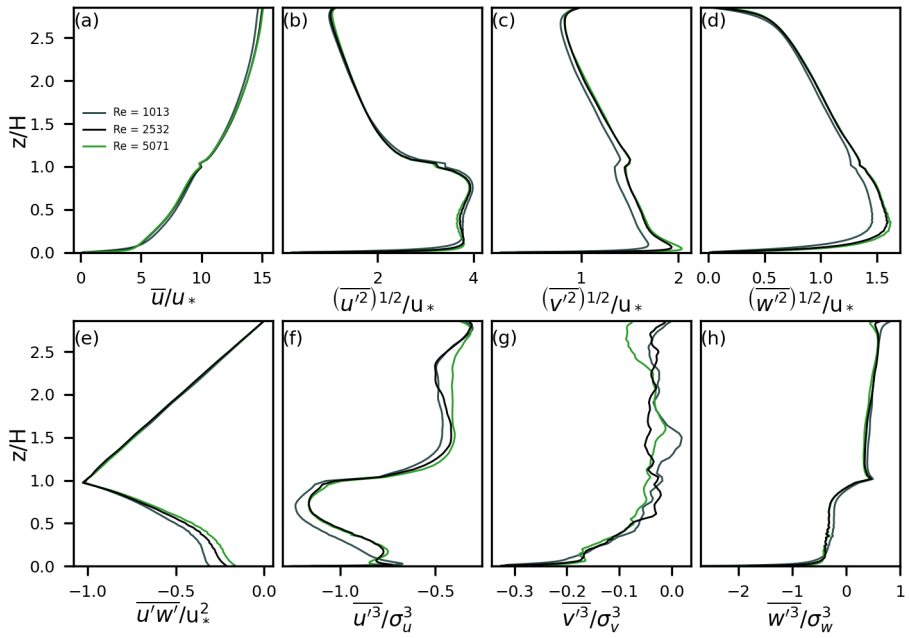

Figure 6.3: (a) Mean wind speed profile, (b) – (d) variances of three wind components, (e) Reynolds stresses and (f) – (g) triplet correlations.

Further information on drivers of dispersion around the buildings can be gained from studying the perturbation pressure field. The differences in the pressure field arise form

the movement of the air that creates dynamic pressure which adds to the hydrostatic pressure. The total pressure field, i.e. the perturbation pressure, we have scaled, as all other variables, with the Reynolds similarity in mind. This way the same pressure differences can be expected in a flow with the same characteristics but in a much larger domain if the scaling is done in the same way we have done it in this study. The modified pressure field here was obtained by scaling the perturbation pressure field with the height of the domain, the source strength and friction velocity like $p^* = p\frac{H^2}{Qu_*}$.

The time-averaged field of modified pressure is obtained by time averaging 100 2D pressure fields. Figure 6.4 (a) shows the top view of the pressure field at the ground level around the first three buildings in the lower row. Similar results are found for the flow around all houses. A first phenomenon to be noted is the pressure build up on the windward side of the houses. This is a consequence of a solid boundary placed perpendicular to the flow. The air is therefore diverted toward the sides of the buildings. On both the south (down) and north (up) sides of the buildings an area of low pressure is visible, which indicates that flow separation is occurring at these locations (Nardecchia et al., 2016). Therefore, very close to the south and north sides of the building a flow opposite from the mean wind direction can be expected. Similarly, Fig. 6.4 (b) shows side view (x-z) of the pressure field around the buildings taken at the mid point of the building width. Again the pressure build-up on the windward side is visible, which is followed by a pressure drop indicating that the leading corner of the building is the point at which the flow separation happens. As a consequence, the flow is in the opposite direction from the mean wind at the top of the buildings .

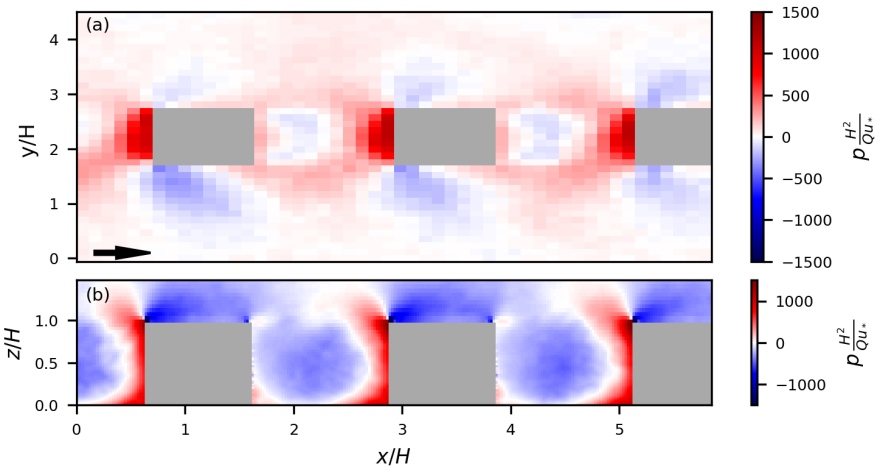

Figure 6.4: (a) Top view (x-y) on the mean non-dimensional pressure field (average over 100 time steps) at ground level, and (b) side-view (x-z) on the mean pressure field at half of the building width. The arrow indicates the mean wind direction in both panels.

The actual direction of the mean wind (average of 100 2D wind fields) can be observed in the quiver plots (Fig. 6.5). From the top view (Fig. 6.5 (a)) it can be seen that a flow in opposite direction from the mean wind developed between the buildings. The air is moving from the area of higher pressure on the windward side towards the lower pressure in-between the buildings (Fig. 6.4 (a,b)) and to the sides of the building. There is also small entertainment of air towards the space between the buildings on the lee side of the buildings. The secondary circulation in the opposite direction that develops between the buildings is clearly visible in Fig. 6.5 (b). Note here that the flow around the 3D objects is one of the best studied problems in the wind engineering field and has been well described in literature (e.g. Martinuzzi & Tropea (1993); Nardecchia et al. (2016)). The pattern observed here is specific to the building morphology and the mean wind direction of the experiment presented here. Different building distributions or wind directions will produce different flow patterns. Coceal et al. (2014) studied the influence of the building distribution and the mean wind direction on plume dispersion in more detail.

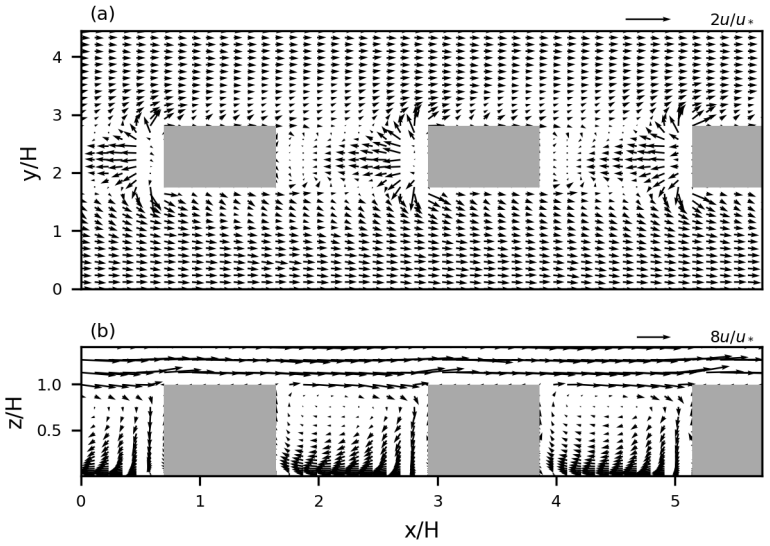

Figure 6.5: ((a) Top view (x-y) on the mean horizontal velocity field (average over 100 time steps) at ground level, and (b) side-view (x-z) on the mean horizontal velocity field at half of the building width.

6.5.2 Mixing ratio fields

From the measurement experiment that motivated this study (section 6.3) it is clear that, more often than not, multiple sources emit methane in the same street. Figure 6.6 (a) shows a snapshot of instantaneous plumes released from sources s_0, s_1, s_3, s_5, s_8 and s_{10}. The snapshot is taken at 5% of the building height ($0.05H$). From the instantaneous plumes it is clear that it would be impossible to differentiate between the individual sources by e.g. taking only one transect through the plumes. The instantaneous

plume is patchy and concentrations maxima appear at locations different from the source locations. Figure 6.6 (b) shows time averaged plumes from the same sources and at the same height. The snapshots of the plumes were recorded over the whole x-y transect every 360 s throughout the whole simulation (1 hour) before averaging, i.e. 100 plumes were averaged. The influence of the buildings on dispersion can be clearly observed in the mean plume field. This is especially true for the plume released from source s_8 which is caught in the circulation between the buildings. As a result, the concentration maximum occurs upwind from the source on the lee side of the previous building. It should be also noted that the difference in maximum concentration in the instantaneous plumes and the time-averaged plume is two orders of magnitude.

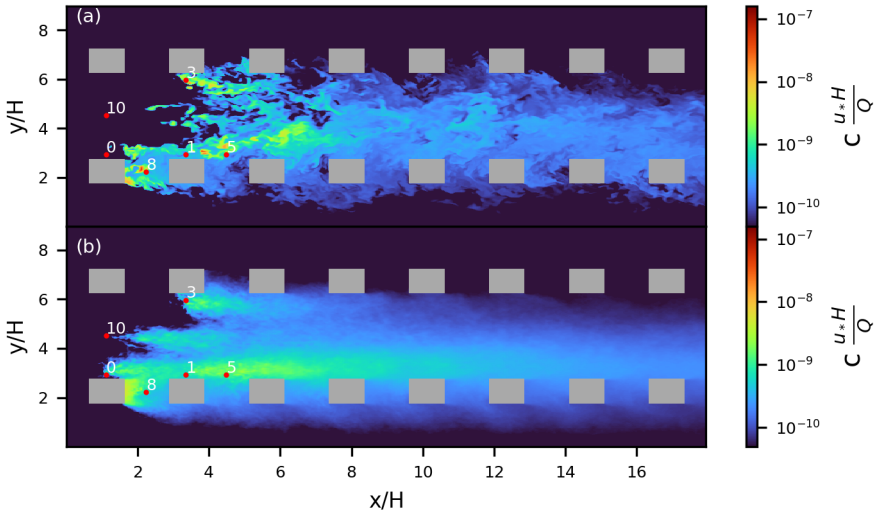

Figure 6.6: Top view (x-y) on the (a) instantaneous, and (b) time-averaged (over 100 time steps) plumes emitted from sources s_0, s_1, s_3, s_5, s_8 and s_{10} (red circles). The x-y transects were taken at the 5% of the building height ($0.05H$).

Thus, apart from the obvious spatial variability, plumes are also highly temporally variable at a certain location. To illustrate this, Fig. 6.7 shows the concentration as a function of time for the plume released from source s_0. The subplots in Fig. 6.7 show the concentrations relative to the first three houses (gray blocks) on both sides of the street. Concentrations were recorded at the mid-point of each block of empty space in-between the houses. For example, the first column of subplots shows the first house on each side of the street and the concentration time-series at a point exactly in the middle of the street. Next to the concentration, also the concentration fluctuation intensity i_c is plotted in the panels as a red dot (right axes). The concentration fluctuation i_c is defined as $\frac{\sigma_c}{\overline{c}}$, where σ_c is the standard deviation of concentration over a time period of 500 s, and $\overline{c}$ is the mean concentration). Fig. 6.7 shows that the plume, emitted from source s_0 in front of the first house in the bottom row, gets mixed in-between the houses of the first row and very rarely reaches the middle of the street and never reaches the opposite row of the houses for downwind distances relatively close to the source. The efficient mixing

in-between the houses is visible in the fast drop of i_c, which has value of 1.30 between the first two houses, and drops to 0.5 between the third and the fourth house. Moreover, the value of i_c has very high values in the middle of the street locations (Fig. 6.7, middle row) indicating that the plume reaches this location very rarely. The plume is wide enough to be actually measured in the middle of the street only further downwind, i.e. after the third house (last column). Figure 6.8 shows the same as Fig. 6.7, but the source now is located between two houses at position s_8. Again, this plume almost never reaches the middle of the street for these downwind locations. Only very rarely (high i_c) the plume gets pushed by an eddy towards the middle of the street. These two figures illustrate the impact of the source location with the respect to the houses on the likelihood of measuring the plume while driving along such a street. The structure of the flow around the houses drags the plumes to the spaces in-between the houses, making it unlikely to measure the plume on the street. This is true only for downwind locations close to the source. Further downwind, however, plumes are more diluted (Fig. 6.6 (a)) and more likely mixed with emissions from other sources. Moreover, the strong intermittency of these plumes in the middle of the street leads to high probabilities of actually missing important emissions.

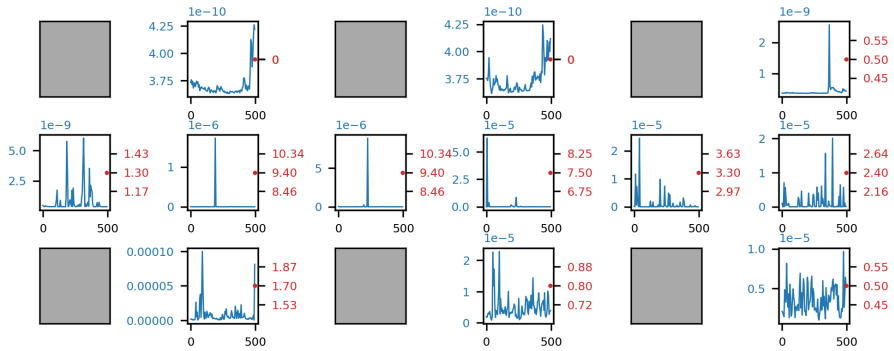

Figure 6.7: Time-series of non-dimensional concentration ($c* = c\frac{u_* H^2}{Q}$) (blue, left y-axes) at locations between the houses. The figure shows concentrations recorded in the middle of the street (middle row) and mid-point (top and bottom rows) between the first three houses (gray blocks) on both sides of the street. The concentration is recorded for 500 s with a time-step of 5 s (x-axis). The second (red) y-axis shows the corresponding concentration fluctuation intensity i_c (the red dot). The panels show concentrations emitted from source s_0, which is located in front of the first house in the bottom row (Fig. 6.2).

6.5.3 The Weller method

In this section we present the analysis of the Weller method described in section 6.2. The analysis focuses only on the plumes emitted from the locations s_0, s_1 and s_5. We have chosen these plumes because one of the goals is to investigate the sensitivity of the Weller method to the crosswind distance from the source. We converted the concentrations

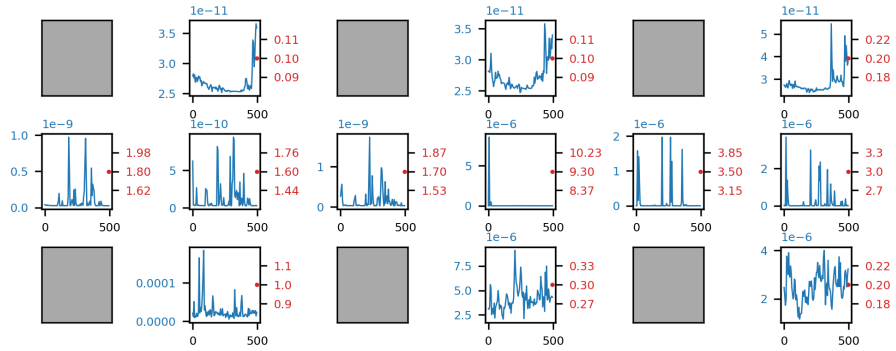

Figure 6.8: Same as for Fig. 6.7, but now the source is located at position s_8 (between the first two houses in the bottom row, Fig. 6.2).

from non-dimensional space to mixing ratios in parts per million, as used in the Weller method. Furthermore, the method gives source strength estimations in L min^{-1}, therefore our source strength ($Q = 1.59 \cdot 10^{-5}$ [kg s^{-1}]) has to be converted to those units. This is done with the assumption of standard atmospheric temperature and pressure ($T = 273$ K, $p = 10^5$ Pa) which results in the release rate of $Q = 1.35$ L min^{-1}.

First we focus on the detection of the leak location part of the algorithm, i.e. the derivation of observed peak locations x_{OP} and leak indications LI. By its definition, x_{OP} is the center of mass of the measured plume on the longitudinal road transect. Note here that we only calculated the OP in the x-direction (x_{OP}). This is due to the fact that the y position of the car is constant while taking a transect. The algorithm itself, as described in Weller et al. (2019), has protocols to filter out the measured methane peaks that are too far apart (approximately 60 m) as it is assumed they do not belong to the same source. For the sake of brevity, we skip the analysis of the validity of this filtering algorithm. Moreover, we focus on the signals from individual plumes and therefore test the Weller method under idealized conditions. Figure 6.9 (a) shows x_{OP} calculated from 50 transects along the street. The x_{OP} values have been calculated for three cross-wind driving distances from the source $y - y_s = \{0.05,\ 0.79,\ 1.59\}\ H$. For reference, the $1.59H$ transect is located at the middle of the road. The transects here are taken at an assumed inlet height of 14% of the building height (0.14H). From Figure 6.9 it is clear that for all three plumes the derived peak location never agrees with the location of the actual source. In this case, this bias can be explained by the wind that carries the plume downwind from the source. During this transport, dispersion takes place. These processes cause the peak mixing ratio on each longitudinal (along-wind) transect to appear on a different downwind location. This will be demonstrated further below, when we present the results of the LI analysis. A related observation is that the closer the transect is to the source, the higher the chance to find the peak concentration at the same location in multiple transects. This again is the consequence of turbulent motions that mix the plume. The plumes are most variable at their edges (e.g. Gailis et al.

(2007)) making it likelier that eddies will cause peak concentrations at a larger interval of downwind distances. Lastly, there is a difference in location of x_{OP} between different sources. We assign this difference to the influence of the buildings on plume dispersion and the relative location of each source with respect to the buildings. This is supported by the fact that the difference in x_{OP} from each plume diminishes as the distance from the building increases and are the smallest on the middle of the road transect. There is also a noticeable difference in the estimated x_{OP} values from sources s_0 and s_1, which have been emitted from the same positions relative to the surrounding buildings. We speculate this is partly by chance and in part due to the fact s_0 is placed closest to the left boundary of the domain. For this release location, any concentration that gets entrained behind the first building and is dragged towards the last building in the street (circular boundary condition on momentum) will be taken out of the simulation by the inflow/outflow boundary conditions that prevent the plume from reentering. This does not happen for release location s_1, which has an extra two building distance upwind for possible entrainment before it would hit the boundary. The influence of single buildings on plume dispersion has been the topic of previous studies (e.g. Fuka et al. (2018)) and it would require further research, perhaps with higher resolution simulations for this specific case.

Figure 6.9 (b) shows LI values calculated as a concentration-weighted average of the 50 derived x_{OP} values (see Eq. 6.2). Apart from the results from the HighRe1 simulation (filled geometric symbols) results from HighRe2, which has double mean wind speed, are also shown (empty line symbols) to investigate whether differences in the mean wind speed cause differences in derived LI values. The results in Fig. 6.9 (b) are given as a difference from the exact source location x_s and scaled with the building height H. The LI values have been calculated for different horizontal (y) distances from the source indicated by the symbol color saturation and for different sampling heights z = [0, 0.14, 0.5, 1.14]H. It is clear from the figure that only driving right over the source will give LI at the exact source location. All other estimations lead to LI values on different downwind distances from the source. There is no clear difference in the derived LI values between the two simulations. This was to be expected as the mean wind influences only the maximum mixing ratios, i.e. lower wind speeds lead to higher mixing ratios, but not the shape of the plumes. For the two simulations the turbulent mixing is identical as was shown in Fig. 6.3. Generally, similar conclusions can be drawn from 6.9 (b) as for 6.9 (a): when the transects are conducted further away from the source, the derived LI values will be further off. Moreover, it can be noticed that for the transects taken at ground level, the spread of the LI values is generally the largest, and for the transect taken at the highest level the spread is the smallest. We assign this again to the advection of the plume with the mean wind and simultaneous mixing with the turbulent eddies. At the ground level the measurements are either taken close to the source, when the dispersion time was short and the peak is still close to the source. Alternatively, the plumes are horizontally displaced from the center of the plume and the peak has had time to travel

downwind before it reaches the location of the transect. For the high transects, the plume has been dispersing in general longer, because it has to be moved up towards the transect location. This displaces the peak locations downwind for all transects taken.

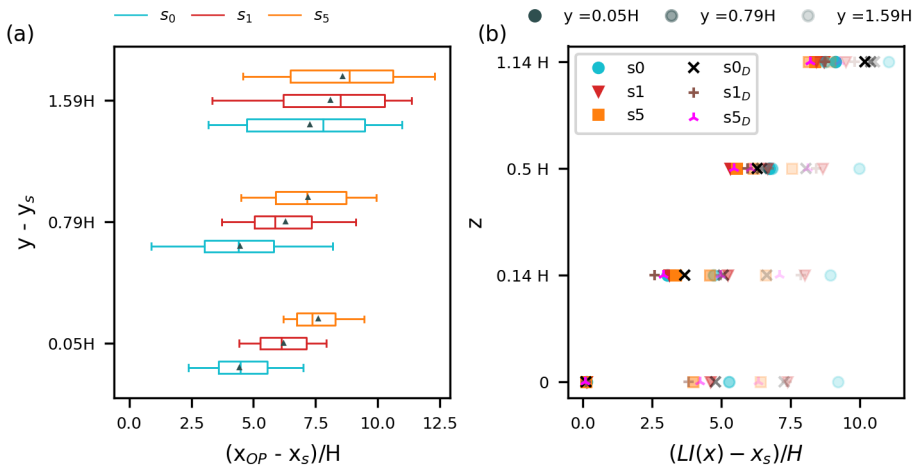

Figure 6.9: (a) Difference between the observed peak location x_{OP} and the actual source location x_s for three plumes calculated for 50 plume transects at three cross-wind distances from the actual source location ($y - y_s$, where y_s is the source location). Boxes span the interquartile range of x_{OP} estimations, while the whiskers show 5 – 95 percentile. The mean (triangle) and the median (vertical line) are also shown. (b) The difference between the leak indication (LI) and x_s calculated from 50 transects x_{OP} for the three plumes at different heights and at different crosswind distances from the source. The crosswind distance is denoted by color saturation of the symbols in the figure, the more saturated symbols being closer to the source and the faintest symbols furthest away (legend above the plot). Also shown are LI values calculated for the simulation with double wind speed (simulation HighRe2 in table 6.1) with symbols annotated with subscript D. Distances on both panels are scaled with the building height H.

Lastly, we show the results for the second part of the Weller method: the source strength estimation (eq. 6.3). Figure 6.10 shows the results of source strength estimations at different crosswind distances from the source at $z = 0.14\ H$ height. The estimations have been calculated for an increasing number of plume transects (1 – 30) averaged over time to reduce and study the influence of turbulence on the source strength estimations. The experiment has been repeated 50 times to gather statistics. It can be seen that with the increasing number of transects averaged before the Weller formula is applied (eq. 6.3) the spread of estimations decreases significantly. It can also be noted that the mean (triangle in Fig. 6.10) decreases with the increasing number of averaged transects. This is a result of averaging as the plumes attain a Gaussian shape with more transects averaged which then results in lower concentration maxima. The result is derived directly from Wellers' eq. 6.3, which is a linear equation relating peak concentration and source strength, with

only one solution. This means that there is only one value of $\overline{\ln c_{max}}$ that will produce the correct source strength estimation Q. As a consequence, a transect at $y = 0.79\ H$ converges to almost the true source strength. At closer (further) distances, the source strength is overestimated (underestimated). For $Q = 1.35$ L min^{-1} $\overline{\ln c_{max}} = -0.74$ (c_{max} = 0.478 ppm) and this requirement is satisfied at a distance approximately $0.79H$ away from the source. There are no clear differences in the estimations from different sources (s0, s1, s5), however, we need to average over at least 10 transects to obtain a $\approx$ 40% accuracy. The need to average over 10 transect has also been shown for other source estimation methods that rely on taking plume transects over flat terrain (Caulton et al., 2018; Ražnjević et al., 2022).

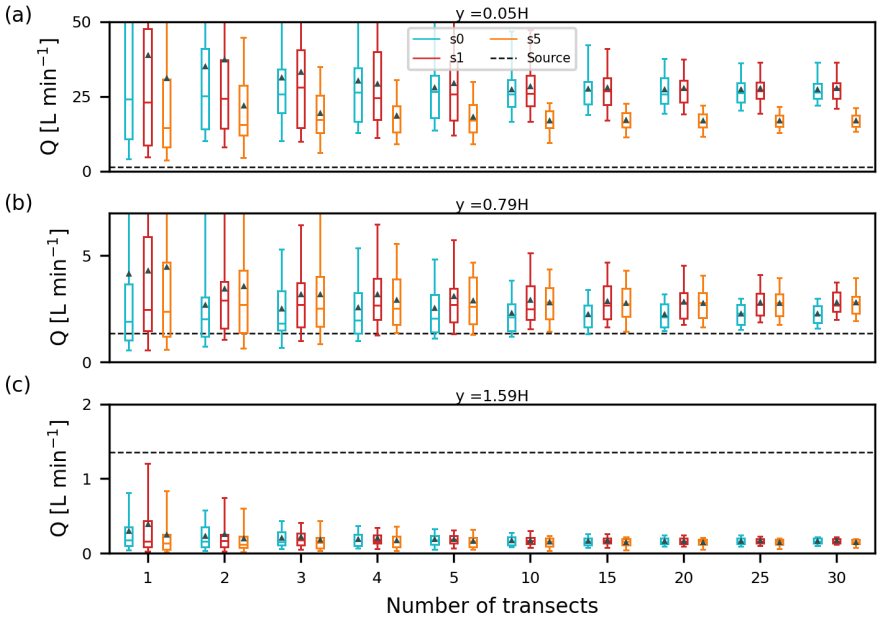

Figure 6.10: Source strength estimations using the Weller method for plumes emitted from three different point sources s_0, s_1 and s_5 (Fig. 6.2). The transects on which the plumes were recorded were at $z = 0.14\,H$ at three different cross-wind distances from the source y = [0.05, 0.79, 1.59] H. The estimations have been calculated for an increasing number of plume transects (1 – 30) and the experiment has been repeated 50 times. Boxes span the interquartile range of source strength estimations, while the whiskers show 5 – 95 percentile. The mean (triangle) and the median (vertical line) are also shown. The dashed line denotes the true emission strength.

We have shown that the wind speed has no discernible influence on the estimation of the source location (Fig 6.9 b). However, the mean wind speed affects the location of the exact mixing ratio maximum which is required to derive the correct emission rate. Figure 6.11 shows values of $\overline{\ln c_{max}}$ at the locations LI that were shown in Fig. 6.9 (b). It can be observed that for the HighRe1 simulation $\overline{\ln c_{max}}$ has values close to –0.74 at the ground level and at z = 0.14 H for y = 0.79 H. However, there are multiple other

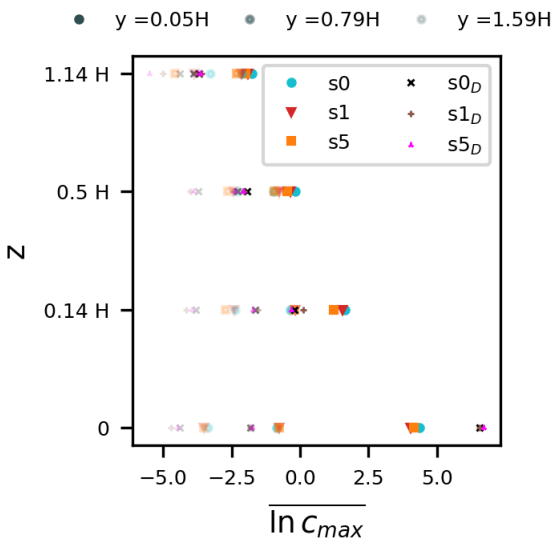

Figure 6.11: Same as for Fig. 6.9 (b), but here $\overline{\ln c_{max}}$ is shown.

instances for which $\overline{\ln c_{max}}$ has values close to this number and for these transects the Weller method will produce correct results as well. When the $\overline{\ln c_{max}}$ are close to –0.74 in the HighRe1 simulation, results from the HighRe2 simulation are lower. Indeed we find, when Fig. 6.10 is produced for the HighRe2 plumes, the source strength at z = 0.14 H and y = 0.79 H is underestimated (not shown). Thus, the Weller method will give good estimations of source strengths on transect closer to the source when the mean wind speed is higher.

6.6 Summary, discussion, and conclusions

This chapter presents an analysis of plume dispersion and an evaluation of source strength estimation methods using an idealized model simulation of an urban residential street. The numerical experiment was modeled after a measurement campaign in Hamburg, where methane was measured from ground leaks using mobile measurement techniques Maazallahi et al. (2022). Since the meteorological data was not recorded during the campaign, we have set-up an experiment with neutral atmospheric conditions and the mean wind aligned with the street direction. The goal of our research was to test the methane source strength estimation technique that was used in the Hamburg campaign (Weller et al., 2019; Maazallahi et al., 2022) in the simplest setting.

Three sets of simulations were performed with different Reynolds numbers, $\mathrm{Re}_\tau = \{1013, 2532, 5071\}$. All three simulations show very similar mean wind profiles in their first three statistical moments, with only very small differences for the smallest Re_τ. It was

discussed in Branford et al. (2011) that wind tunnel experiments (Castro & Robins, 1977; Snyder & Castro, 2002) and large-eddy simulations (LES) (Xie & Castro, 2006) show very weak dependency to the Reynolds number for flows over sharp-edged obstacles, and our results support these findings. Therefore, for our analysis we used mostly data from the $\mathrm{Re}_\tau = 2532$ simulation, and studied the influence of the wind speed on the Weller method using the data from $\mathrm{Re}_\tau = 5071$ as these two simulations differ only in the mean wind speed.
The analysis of pressure and horizontal wind vectors shown in Fig. 6.4 and 6.5 clearly shows the influence of the buildings on the flow field. The buildings cause the air on the upwind side of the building to sink towards the ground and flow upstream towards the lee side of the previous building. Furthermore, there is small lateral entrainment of air from the sides of the buildings into the inter-building space. For sources placed in close vicinity of buildings, which is where we placed the artificial sources in this study, the buildings will distort the plumes and cause material to gather in the spaces in between the buildings (Fig. 6.6). This is especially important for the source estimation methods like the Weller method analyzed in this study. This method estimates source location and source strength from mobile plume measurements taken by driving along street. In order to estimate the position of the source, the method assumes that there are no other sources interfering in the measurements, this is possible only very close to the source. However, our results show that the presence of buildings cause the plumes to remain relatively close to the buildings and reach the middle of the street only further downwind. This effect is differently pronounced for different placements of the sources with respect to the surrounding buildings (Fig. 6.7 and 6.8).

The Weller method consists of two parts: (1) locating the source and (2) estimating the source strength. Our analysis shows that the correct estimation of the location of the source heavily depends on the distance between the transect the source is on and the transect the measurements are taken on. The further away from the line on which the source is located on, either vertically or horizontally, the larger the error in the estimation of the location is (Fig. 6.9). The only time the method places the source at its exact location is when the transect is taken exactly over the source location. This is a consequence of the mean wind moving the peak in mixing ratio downwind from the source. In general, the further away from the source the farther downwind the peak in mixing ratio is located. This follows directly from the Gaussian plume model (e.g. Seinfeld (1986)). The spread in the source location estimations also grows with the distance from the source. This can be explained by high mixing ratio fluctuations at the edge of the plume (e.g. Gailis et al. (2007); Ražnjević et al. (2022)). An increase in the mean wind speed, when all the other parameters remain the same, does not influence the source location estimations and for the low wind speed ($\mathrm{Re}_\tau = 2532$) and the high wind speed ($\mathrm{Re}_\tau = 5071$) simulations the method places the source at the same location.

The differences in the mean wind speed, however, do influence the source strength estimation part of the Weller method. It is clear from eq. 6.3 that there is only one value of $\overline{\ln c_{max}}$ for which the Weller formula will give the correct value for the emission rate Q. Firstly, we find that this value is not attained at the source location, since the empirically fitted parameters in the equation in combination with large values of mixing ratios we simulate at the source location grossly overestimate the emissions. Therefore, the method will either estimate the emission rate right or get the location of the source right, or neither. Secondly, there exists a distance from the source centerline (either vertically or horizontally) on which the Weller method will produce the correct source estimations. This distance depends on the mean wind speed as it influences the height of the maximum mixing ratio along a certain transect.
We have not found a significant difference in the source estimations for the three sources we have chosen for our analysis (s0, s1, s5, see Fig. 6.10), but we have found that at least 10 transect are needed to average out the atmospheric variability and to get an estimation that is within 40% error of the true emission rate. This finding supports other studies that focused on similar mobile measurement methods in combination with simple plume models (Caulton et al., 2018; Ražnjević et al., 2022).

As mentioned in the introduction of this section, our study focused on an idealized residential street in neutral atmospheric conditions with the mean wind aligned with the street. However, there are multiple degrees of freedom for modifying this experiment for which we expect the method will produce different results. Any variable that influences plume dispersion in turn influences the source estimate following the Weller method. The first, and most intuitive, influence on dispersion we mention here comes from the meteorological conditions. This influence can be expressed through atmospheric stability (i.e. the influence of turbulence on plume mixing) and through the mean wind speed. For example, in an unstable atmosphere the plume will be wider and more intermittent than the plume studied here, due to enhanced turbulent mixing. This will in turn lower the mixing ratio maximum. Furthermore, the mean wind speed directly affects the mixing ratio maximum which in turn reflects in the source strength estimations. For example, on a given transect the mixing ratio maximum will be found at a same downwind distance from the source regardless of the wind speed. However, for a stronger mean wind, the maximum will be smaller and consequently the estimated source strength will also be smaller. In urban areas the local topography has a large influence on the wind direction (Ng et al., 2011). Therefore, in dispersion studies, it is of great importance to measure the wind simultaneously with the plumes as it can differ significantly from the data from the closest meteorological station or from reanalysis data like ERA5 (Hersbach et al., 2020). Again, specific transects will lead to a correct source estimation, but how transects need to be conducted to identify "unknown" sources under different meteorological conditions remains a question for further research. One possible modification to the Weller method has recently been explored in a Rotterdam campaign (summer, 2022) where the method

was employed to estimate the city's methane emissions (private communication). The modified version of the method uses the integral of the mixing ratio enhancements over the entire transect rather than just the maximum. With this approach it can be expected that too high estimations resulting from taking too few plume transects (i.e. the maximum mixing ratio varies strongly due to atmospheric variability) are avoided. However, this approach does not solve the problem the Weller method faces with the estimations being correct only on one transect. The integral of concentrations, as the mixing ratio maximum, also changes with the distance from the source. Therefore, there will exist only one lateral distance from the source for which the method will give correct estimations. As with the maximum mixing ratio, this distance depends on local topography as well as on the atmospheric stability. Other factors, apart from atmospheric stability, that influence plume dispersion include the angle between the mean wind and the street (Coceal et al., 2014) and the spacing and heights of different buildings (Mavroidis & Griffiths, 2001). Finally, the Weller method also consists of an algorithm that contributes measured methane peaks to different sources based on the distance between the measured peaks. We have not addressed this algorithm in this study. The goal of the study was to benchmark the method for the simplest case of one plume emitted at different source locations, for which the method performed poorly. We expect that adding even more degrees of freedom will not improve the performance.

In our study we focused only on analyzing and evaluating one measurement strategy, which we find very sensitive to external conditions. However, high resolution DNS simulations in combination with well-planned and versatile tracer release experiments may lead to a more universal approach to estimate source strength in urban settings.

Chapter 7

Synthesis

7.1 Introduction

In this chapter, I give an overview of the most relevant research findings presented in this thesis. Specifically, this will be done by discussing to which extent the research questions presented in the introduction to this thesis (Chapter 1) have been answered and how further research can build upon the findings presented here. As the work in this thesis either focuses on plume measurement techniques (Chapters 3 and 6) or high-resolution plume modelling (Chapters 4 and 5), these topics will be discussed separately here as well.

7.2 Summary of the most relevant findings

7.2.1 Evaluation of plume measurement strategies

The main focus of Chapters 3 and 6, and the first objective of this thesis, was to evaluate source estimation measurement strategies. In Chapter 3 two measurement strategies, 1D plume transect and stationary Other Test Method 33a (OTM33a), were evaluated. The idea behind this chapter was to see how well these strategies perform under the most simple turbulence conditions, i.e. neutral atmospheric flow over a flat terrain, and to determine the influence of atmospheric variability on the errors in the source strength estimation. For the measurements that are done by taking 1D transects through the plume perpendicular to the mean wind we showed that the estimation error drops down to $\approx 40\%$ when at least 15 transects are averaged in time. This supports the findings of Caulton et al. (2018); to infer the source strength eq. 3.4 performs well assuming the vertical plume dispersion is well represented in the Gaussian plume model (GPM). For the Briggs dispersion coefficients for neutral atmosphere that we used in the study, that was the case. Another source of error for the plumes emitted close to the ground comes from the mismatch in the plume centerline position. This height is assumed to be at the source height in the GPM, but the actual plume centerline position is lifted towards the center of the boundary layer. This can be corrected, however, by adjusting the emission height in the GPM to the corresponding plume centerline height.
For the OTM33a method, things are a bit more complicated. The method is based on point measurements at the source height exactly downwind from the source. Implicitly, this requirement assumes that this is the location of the plume centerline. By measuring exactly in the centerline, the GPM (eg. 3.1) is simplified to the equation 3.3 the OTM33a method is based on. We have shown that the location of the plume centerline is not always at the height of the source and depends not only on the downwind distance from the source, but also on the height of the source (Fig. 3.9). The biggest error in the estimation of the source strength, however, comes from the use of the dispersion parameters. Using our simulation results as input, we have consistently overestimated the source strength while using the method as described in the method guide (U.S. EPA, 2014). This we

could directly link to the dispersion parameters. Equation 3.3 is a linear equation and thus the source strength estimation is directly proportional to the dispersion parameters. If these parameters are wrong, this will be reflected in the estimation of source strength. In theory, the OTM33a method can correctly estimate the source strength, but only if requirements mentioned here are fulfilled.
The last measurement strategy we evaluated, the estimation of source strength from along-the-street car transects using the Weller equation (eq. 6.3), is presented in Chapter 6. This method was developed by Weller et al. (2019) and it consists of two parts: detection of the source location and source strength estimation from the measurements taken longitudinally through the plume. For the detection of the source location, we have found that the method locates the source correctly only if the measurements are taken directly by driving over the source. The further away from the source location the measurements are taken, the larger the error in the location estimation. The structure of turbulence when obstacles such as buildings, are present, heavily depends on the positioning and shape of these obstacles. There are an infinite degrees of freedom for the shape and structure of buildings and objects in a street. This makes finding a very simple universal model for source location estimation rather a complicated, if not impossible, endeavor. Similar conclusion can be drawn for the second part of the method: the source strength estimation. Equation 6.3 is a linear equation with two empirically fitted constants. As such, the equation has only one solution that links the source strength to the measured concentration enhancement. Therefore, for only one value of the maximum concentrations derived from the plume transects will the method give the correct source estimation. Due to the specific shape of time-averaged plumes (the GPM) there exists an ellipse of distances around the plume centerline on which this condition is fulfilled. For the wider plumes this ellipse will be further away from the centerline, for narrower plumes it will be closer and the shape of the plume depends on the atmospheric stability and the morphology of the area the plume is dispersing in.

7.2.2 Plume dispersion modelling

The second main topic of this thesis deals with high resolution plume modelling methods, namely direct numerical simulations (DNS) and large-eddy simulations (LES), and their ability to accurately reproduce plume dispersion under less than atmospheric Reynolds number flows (Chapter 5) and in exactly the atmosphere encountered on a measurement day (Chapter 4).
We used LES to reproduce one measurement day during the Romanian methane emissions from gas and oil industry (ROMEO) campaign conducted by the MEthane goes MObile - MEasurements and MOdelling (MEMO)^2 project in October of 2019. We did this to demonstrate the ability of LES to mimic an actual plume encountered in the field and take a step away from the standard dispersion in a channel flow studies. The first important finding from this chapter is: to reproduce the exact meteorological conditions

encountered in the field, a detailed set of meteorological measurements, such as vertical profiles of wind, humidity and temperature, should be taken simultaneously with the plume measurements. Our LES takes the mean vertical profiles of relevant meteorological variables from measurements or a different model and nudges the mean profiles in the run towards these data with a chosen relaxation time scale. This way it is ensured that the desired mean profiles are reproduced, while the turbulence is allowed to develop freely. During the ROMEO campaign only the wind data using a 3D sonic was recorded, which is a point measurement. Therefore, we used ERA5 (Hersbach et al., 2020) data to force the simulation. As expected, due to the coarse resolution of ERA5 (30×30 km) there were some discrepancies between the measured and simulated wind, which we corrected by doing a second simulation to match the measured wind. In Chapter 3, we have pointed out the drawbacks of using the GPM for source strength estimations. In this chapter we used plumes calculated by LES to estimate the emission rate from an oil-well from the plume data measured during the campaign. LES gave almost identical result (10 % lower) to the emission rate estimated using the observed plume from a co-emitted tracer gas that was emitted from the oil-well. Furthermore, the advantage of using LES in this manner is that the full and detailed 3D information of the plume is available in every time-step together with the simulated meteorological data. This allows for a greater in-depth study of plume dispersion. We were able to show good agreement between our LES experiment and previous experimental and theoretical research that targeted plumes in channel flows. We also demonstrated the use of LES for validation of parametrizations in more simple models, namely the fluctuating plume model, which is based on predicting the shape of the fluctuation intensity parameter i_c. Knowing the shape of i_c can help plan future campaigns as it predicts the likelihood of encountering the plume at a certain location.
We have proven the benefit of using LES for plume dispersion simulations again in Chapter 4. However, it should be noted that, depending on the resolution, a certain part of the turbulence in LES is cut off and parametrized (e.g. Pope (2000)). This likely affects the simulated plume dispersion, especially close to the source where small structure turbulence, in case of point sources, is more important. We tested this by performing a series of DNS experiments with increasing Reynolds numbers in Chapter 5. The goal of this chapter was twofold: 1) to investigate if there really is influence of resolution and sub-grid parametrization from LES on the plume dispersion by comparing LES to DNS and 2) to test if there is a critical Reynolds number to which the higher-order statistical plume profiles converge to. The motivation behind this chapter is that DNS is often discarded for dispersion studies as it is unable to reach the atmospheric Reynolds number flows. However, DNS comes with the advantage of having fully resolved turbulent fields. Therefore, if there was a critical Reynolds number at which mean statistical profiles of the measured plume converge to, then DNS can be used for dispersion studies at considerably lower-than-atmospheric Reynolds numbers. We compared our simulation results to data from the wind tunnel plume dispersion experiment from Nironi et al. (2015). We showed that almost all simulations, save for the least turbulent one, simulate the mean

concentration fields in agreement with the measurements (Fig. 5.5). This indicates that the mean plume spread is mainly governed by the dispersion caused by the largest eddies. The low Reynolds number effects, however, are clearly visible already in the second order moment. Only the two most turbulent DNS experiments were able to reproduce the variance profiles as they were measured in the experiment. The same is true for the skewness and kurtosis profiles. More importantly, the two most turbulent simulations have shown convergence in all four statistical moments (Fig. 5.6). Furthermore, we have shown that DNS out-performs LES for very close-source dispersion, while far away from the source LES outperforms DNS (Fig. 5.7). We speculate this is a low Reynolds number effect: There are not enough small-sized eddies in DNS to mix the plume sufficiently on large distances from the source.

7.3 Outlook

As with the summary of the most relevant findings, here the discussion will be divided in to the two main topics: measurements and modelling.

7.3.1 Improving the source strength estimation methodologies

If there was to be one leitmotif in this thesis, in regards to the measurements, it would surely have to be the need to make good measurements of meteorological data simultaneously with the plume measurements. We have shown from chapter to chapter the sensitivity of the plume dispersion and ultimately the source strength estimations, to the meteorological conditions. This point was easy for us to highlight, since our experiment was perfectly controlled and there were no unknown variables. In the field, valuable information about the plume is lost by not measuring the atmospheric conditions the plume is immersed in. For example, the source strength estimations using the GPM presented in chapter 3 rely also on the stability of the atmosphere and dependency is visible in the dispersion coefficients of the model (eq. 3.2). To be certain that the right dispersion coefficients are used, meteorological balloon soundings can be conducted to sample temperature profiles that inform about the vertical structure of the atmosphere.

Even larger emphasis we put on taking wind measurements. Not only is wind the main driver of plume dispersion, but most of the models commonly in use to estimate emission rates (i.e. the GPM) have wind data as input. The wind can be locally influenced by orography and can differ greatly from the data recorded at the nearest weather station or from a model in which the spatial resolution is too coarse to see the influence of local orography. The necessity of taking wind measurements is especially highlighted in chapter 6. The Weller method does not take the wind into account for the source strength estimations, while the experiments with varying mean wind speeds produced different source estimations.
The second point of discussion is the methods for sampling the plume itself. The methods

presented here rely on either taking a 1D transect through the plume, longitudinal or transversal, or making stationary point measurements. We have shown the sensitivity of these methods to the source height, the positioning of the measurement instruments out of the plume centerline, to the atmospheric stability, etc. All of these drawbacks come from the utilization of the simplified dispersion models for the source estimations. A way to circumvent these drawbacks would be to measure the vertical extent of the plume as well. For example, a small swarm of unmanned areal vehicles (UAVs), or drones, that take a 2D transect of the plume for 15 minutes can provide enough data for the atmospheric variability to be sufficiently averaged out. Subsequently, a mass balance approach can be used for source estimation. UVAs are currently in use for source strength estimations, however, most often a single drone is employed to take plume transects perpendicular to the mean wind on multiple heights (Vinković et al., 2022). This way, only a handful of measurements can be taken on a single day and with stationary meteorological conditions, which makes these measurements sensitive to atmospheric variability.

The situation is more complicated in cities where, as was discussed in chapter 6, the presence of obstacles greatly influences plume dispersion. We have shown that the simple Weller method depends greatly on the positioning of the source and the distance from the source on which the plume transect is taken. This is something that usually is not easy to account for in the cities as the driving is constrained to the available roads. The screening of the roads for detection the presence of plumes and then manually locating plumes and measuring the emission rate at the source represents a better approach then the mobile methods alone (Maazallahi, 2022).

7.3.2 Perspectives on the high resolution plume modelling

As mentioned before, this thesis contains studies of high-resolution modelling techniques in relation to plume dispersion. Firstly, we would like to point out that this thesis does not focus on the development of these models but rather only on their application. Therefore, this discussion will focus on how to further utilize these models for dispersion studies.

Chapter 5 focuses on the suitability of DNS for point-source plume dispersion studies and we have shown a satisfactory convergence of higher-order statistical moments of the simulated plumes. This has been performed for a neutral channel flow because of the availability of validation data. A logical next step would be to expand this study to other stability regimes and other surface morphology configurations. DNS has proven to outperform LES on downwind distances close to the source, and here DNS is more suitable than LES for dispersion studies with obstacles (chapters 5 and 6). Considering that the cities are main emitters of methane and the trend is increasing as more people are expected to live in cities in the coming decades, DNS has the potential to become a very useful tool to help in estimating city emissions.

We demonstrated the ability of LES to reproduce meteorological conditions and simulate plume dispersion in conditions encountered in the field 4. We were able to study the observed plume at a spatial and temporal resolution that cannot be achieved in the field. However, due to the lack of meteorological measurements from the campaign, we had to rely on ERA5 data for boundary conditions for the simulations. The next step would be to pair LES with a good set of measurements, both of concentrations and of meteorological variables, for a proper LES validation. Furthermore, if a measurement campaign would consist of multiple measurement days with different stability conditions, this would allow for revisiting the dispersion coefficients commonly used in GPMs. For its simplicity and ready-to-use approach, we expect the GPM to continue to be one of the main source estimation models. As was shown in chapter 3, when a certain set of conditions is fulfilled, such as ensuring that the measurements are in the centerline and that the employed dispersion coefficients are correct, GPM produces accurate source strength estimations. LES, in combination with meteorological measurements, can provide an ensemble of simulations from which correct parametrizations of mean plume dispersion coefficients can be inferred as it provides such spatial and temporal details of the plumes that can never be expected from measurements. The maturity of LES and DNS in resolving intermittent flow characteristics, also for tracer dispersion in complicated geometries, makes these tools very suitable for in depths studies, like presented in this thesis.

References

Alam, J. M., & Fitzpatrick, L. P. (2018). Large eddy simulation of flow through a periodic array of urban-like obstacles using a canopy stress method. Computers & Fluids, 171, 65-78.

Alvarez, R. A., Zavala-Araiza, D., Lyon, D. R., Allen, D. T., Barkley, Z. R., Brandt, A. R., ... & Hamburg, S. P. (2018). Assessment of methane emissions from the US oil and gas supply chain. Science, 361(6398), 186-188.

Andersen, T., Scheeren, B., Peters, W., & Chen, H. (2018). A UAV-based active AirCore system for measurements of greenhouse gases. Atmospheric Measurement Techniques, 11(5), 2683-2699.

Andersen, T., Vinkovic, K., de Vries, M., Kers, B., Necki, J., Swolkien, J., ... & Chen, H. (2021). Quantifying methane emissions from coal mining ventilation shafts using an unmanned aerial vehicle (UAV)-based active AirCore system. Atmospheric Environment: X, 12, 100135.

Anderson, W., Meneveau, C. (2010). A Large-Eddy Simulation Model for Boundary-Layer Flow Over Surfaces with Horizontally Resolved but Vertically Unresolved Roughness Elements. Boundary-Layer Meteorol 137, 397–415.

Ardeshiri, H., Cassiani, M., Park, S. Y., Stohl, A., Pisso, I., & Dinger, A. S. (2020). On the Convergence and Capability of the Large-Eddy Simulation of Concentration Fluctuations in Passive Plumes for a Neutral Boundary Layer at Infinite Reynolds Number. Boundary-Layer Meteorology, 1-37.

Atherton, E., Risk, D., Fougére, C., Lavoie, M., Marshall, A., Werring, J., ... & Minions, C. (2017). Mobile measurement of methane emissions from natural gas developments in northeastern British Columbia, Canada. Atmospheric Chemistry & Physics, 17(20).

Baillie, J., Risk, D., Atherton, E., O'Connell, E., Fougére, C., Bourlon, E., & MacKay, K. (2019). Methane emissions from conventional and unconventional oil and gas production sites in southeastern Saskatchewan, Canada. Environmental Research Communications, 1(1), 011003.

Baker, L. H., Collins, W. J., Olivié, D. J. L., Cherian, R., Hodnebrog, Ø., Myhre, G., & Quaas, J. (2015). Climate responses to anthropogenic emissions of short-lived climate pollutants. Atmospheric Chemistry and Physics, 15(14), 8201-8216.

Bakkaloglu, S., Lowry, D., Fisher, R. E., Menoud, M., Lanoisellé, M., Chen, H., ... & Nisbet, E. G. (2022). Stable isotopic signatures of methane from waste sources through atmospheric measurements. Atmospheric Environment, 276, 119021.

Barad, M. L. (1958). Project Prairie Grass, a field program in diffusion. Volume 1 (No. GRP-59-VOL-1). Air Force Cambridge research labs Hanscom AFB MA.

Barlow, J.F., Coceal, O., (2009). A Review of Urban Roughness Sublayer Turbulence, UK Met Office Technical Report no. 527, pp. 68.

Bergamaschi, P., Frankenberg, C., Meirink, J. F., Krol, M., Dentener, F., Wagner, T., ... & Dlugokencky, E. J. (2007). Satellite chartography of atmospheric methane from SCIAMACHY on board ENVISAT: 2. Evaluation based on inverse model simulations. Journal of Geophysical Research: Atmospheres, 112(D2).

Berman, E. S., Fladeland, M., Liem, J., Kolyer, R., & Gupta, M. (2012). Greenhouse gas analyzer for measurements of carbon dioxide, methane, and water vapor aboard an unmanned aerial vehicle. Sensors and Actuators B: Chemical, 169, 128-135.

Boppana, V.B.L., Xie, Z.-T., & Castro, I.P., (2010). Large-eddy simulation of dispersion from surface sources in arrays of obstacles. Boundary-Layer Meteorology 135, 433-454.

Boppana, V. B. L., Xie, Z. T., & Castro, I. P. (2012). Large-eddy simulation of dispersion from line sources in a turbulent channel flow. Flow, turbulence and combustion, 88(3), 311-342.

Bou-Zeid, E., Meneveau, C., & Parlange, M. (2005). A scale-dependent Lagrangian dynamic model for large eddy simulation of complex turbulent flows. Physics of fluids, 17(2), 025105.

Branford, S., Coceal, O., Thomas, T.G., Belcher, S.E., (2011). Dispersion of a point-source release of a passive scalar through an urban-like array for different wind directions. Boundary-Layer Meteorology 139, 367-394.

Brantley, H. L., Thoma, E. D., Squier, W. C., Guven, B. B., & Lyon, D. (2014). Assessment of methane emissions from oil and gas production pads using mobile measurements. Environmental science & technology, 48(24), 14508-14515.

Brasseur, J. G., & Wei, T. (2010). Designing large-eddy simulation of the turbulent boundary layer to capture law-of-the-wall scaling. Physics of Fluids, 22(2), 021303.

Briggs, G., (1973). Diffusion estimation of small emissions. In Atmospheric Turbulence and Diffusion Laboratory Contribution No. 79, 83-145.

Carpentieri, M., & Robins, A. G. (2015). Influence of urban morphology on air flow over building arrays. Journal of Wind Engineering and Industrial Aerodynamics, 145, 61-74.

Cassiani, M., Bertagni, M. B., Marro, M., & Salizzoni, P. (2020). Concentration Fluctuations from Localized Atmospheric Releases. Boundary-Layer Meteorology, 1-50.

Castro, I. P., & Robins, A. G. (1977). The flow around a surface-mounted cube in uniform and turbulent streams. Journal of fluid Mechanics, 79(2), 307-335.

Castro, I. P., Xie, Z. T., Fuka, V., Robins, A. G., Carpentieri, M., Hayden, P., Hertwig, D., & Coceal, O. (2017). Measurements and computations of flow in an urban street system. Boundary-Layer Meteorology, 162(2), 207-230.

Caulton, D. R., Li, Q., Bou-Zeid, E., Fitts, J. P., Golston, L. M., Pan, D., ... & McSpiritt, J. (2018). Quantifying uncertainties from mobile-laboratory-derived emissions of well pads using inverse Gaussian methods. Atmospheric Chemistry and Physics, 18(20), 15145-15168.

Cimorelli, A. J., Perry, S. G., Venkatram, A., Weil, J. C., Paine, R. J., Wilson, R. B., ... & Brode, R. W. (2005). AERMOD: A dispersion model for industrial source applications. Part I: General model formulation and boundary layer characterization. Journal of applied meteorology, 44(5), 682-693.

Christensen, T. R., Johansson, T., Åkerman, H. J., Mastepanov, M., Malmer, N., Friborg, T., ... & Svensson, B. H. (2004). Thawing sub-arctic permafrost: Effects on vegetation and methane emissions. Geophysical research letters, 31(4).

Coceal, O., Goulart, E. V., Branford, S., Thomas, T. G., & Belcher, S. E. (2014). Flow structure and near-field dispersion in arrays of building-like obstacles. Journal of Wind Engineering and Industrial Aerodynamics, 125, 52-68.

Coles, D. (1956.). The law of the wake in the turbulent boundary layer. J. Fluid Mech. 1(02), 191–226.

Conley, S., Faloona, I., Mehrotra, S., Suard, M., Lenschow, D. H., Sweeney, C., ... & Kort, E. A. (2017). Application of Gauss's theorem to quantify localized surface emissions from airborne measurements of wind and trace gases.

Csanady, G. T. (1967). Concentration fluctuations in turbulent diffusion. Journal of Atmospheric Sciences, 24(1), 21-28.

Csanady, G. T. (1973). Turbulent Diffusion in the Environment. D. Reidel Publishing Company, Dordrecht, 248 pp.

Cui, Y. Y., Henze, D. K., Brioude, J., Angevine, W. M., Liu, Z., Bousserez, N., ... & Ryerson, T. (2019). Inversion Estimates of Lognormally Distributed Methane Emission Rates From the Haynesville-Bossier Oil and Gas Production Region Using Airborne Measurements. Journal of Geophysical Research: Atmospheres, 124(6), 3520-3531.

Davidson, M. J., Mylne, K. R., Jones, C. D., Phillips, J. C., Perkins, R. J., Fung, J. C. H., & Hunt, J. C. R. (1995). Plume dispersion through large groups of obstacles—a field investigation. Atmospheric environment, 29(22), 3245-3256.

Deardorff, J. W. The use of subgrid transport equations in a three-dimensional model of atmospheric turbulence. (1973). J Fluid Eng 95: 429-438.

Dinger, A. S., Stebel, K., Cassiani, M., Ardeshiri, H., Bernardo, C., Kylling, A., ... & Stohl, A. (2018). Observation of turbulent dispersion of artificially released SO2 puffs with UV cameras. Atmospheric Measurement Techniques, 11, 6169–6188.

Dlugokencky, E., NOAA/GML gml.noaa.gov/ccgg/trends_ch4/

Dosio A, de Arellano JVG (2006). Statistics of absolute and relative dispersion in the atmospheric convective boundary layer: a large-eddy simulation study. J Atmos Sci 63:1253-1272.

Edie, R., Robertson, A. M., Field, R. A., Soltis, J., Snare, D. A., Zimmerle, D., ... & Murphy, S. M. (2020). Constraining the Accuracy of Flux Estimates Using OTM 33A.

Eisma, H. E., Tomas, J. M., Pourquie, M. J. B. M., Elsinga, G. E., Jonker, H. J. J., & Westerweel, J. (2018). Effects of a fence on pollutant dispersion in a boundary layer exposed to a rural-to-urban transition.Boundary-Layer Meteorology, 169(2), 185-208. https://doi.org/10.1007/s10546-018-0367-1

U.S. EPA. (2014). Other Test Method (OTM) 33 and 33A GeospatialMeasurement of Air Pollution-Remote Emissions Quantification-Direct Assessment (GMAP-REQ-DA). [https://www.epa.gov/emc].

Ercolani, G., Gorlé, C., Corbari, C., & Mancini, M. (2017). RAMS sensitivity to grid spacing and grid aspect ratio in large-eddy simulations of the dry neutral atmospheric boundary layer. Computers & Fluids, 146, 59-73.

Fackrell, J., Robins, A., (1982a). The effects of source size on concentration fluctuations in plumes. Boundary-Layer Meteorol 22(3):335–350.

Fackrell, J., Robins, A., (1982b). Concentration fluctuations and fluxes in plumes from point sources in a turbulent boundary layer. J Fluid Mech 117:1–26.

Finn, D., Carter, R.G., Eckman, R.M., Rich, J.D., Gao, Z., Liu, H., (2018). Plume dispersion in low-wind-speed conditions during project Sagebrush phase 2, with emphasis on concentration variability. Boundary-Layer Meteorol. 169:67–91.

Finnigan, J. (2000). Turbulence in plant canopies. Annual review of fluid mechanics, 32(1), 519-571.

Foster-Wittig, T. A., Thoma, E. D., & Albertson, J. D. (2015). Estimation of point source fugitive emission rates from a single sensor time series: A conditionally-sampled Gaussian plume reconstruction. Atmospheric Environment, 115, 101-109.

Fritz, B. K., Shaw, B. W., & Parnell, C. B. (2005). Influence of meteorological time frame and variation on horizontal dispersion coefficients in gaussian dispersion modeling. Transactions of the ASAE, 48(3), 1185-1196.

Fuka, V., Xie, Z. T., Castro, I. P., Hayden, P., Carpentieri, M., & Robins, A. G. (2018). Scalar fluxes near a tall building in an aligned array of rectangular buildings. Boundary-layer meteorology, 167(1), 53-76.

Gailis, R. M., Hill, A., Yee, E., & Hilderman, T. (2007). Extension of a fluctuating plume model of tracer dispersion to a sheared boundary layer and to a large array of obstacles. Boundary-layer meteorology, 122(3), 577-607.

Gifford, F., (1959). Statistical properties of a fluctuating plume dispersion model. Adv.Geophys. 6, 117-137. Elsevier.

Griffiths, R. F. (1994). Errors in the use of the Briggs parameterization for atmospheric dispersion coefficients. Atmospheric Environment, 28(17), 2861-2865.

Goulart, E. V., Coceal, O., & Belcher, S. E. (2018). Dispersion of a passive scalar within and above an urban street network. Boundary-layer meteorology, 166(3), 351-366.

Guo, D., Zhao, P., Wang, R., Yao, R., & Hu, J. (2020). Numerical simulations of the flow field and pollutant dispersion in an idealized urban area under different atmospheric stability conditions. Process Safety and Environmental Protection, 136, 310-323.

Hackl, J. F., Yeung, P. K., & Sawford, B. L. (2011). Multi-particle and tetrad statistics in numerical simulations of turbulent relative dispersion. Physics of Fluids, 23(6), 065103.

Henn, D. S., & Sykes, R. I. (1992). Large-eddy simulation of dispersion in the convective boundary layer. Atmospheric Environment. Part A. General Topics, 26(17), 3145-3159.

Hensen, A., & Scharff, H. (2001). Methane emission estimates from landfills obtained with dynamic plume measurements. Water, Air and Soil Pollution: Focus, 1(5-6), 455-464.

Hensen, A., Groot, T. T., Van den Bulk, W. C. M., Vermeulen, A. T., Olesen, J. E., & Schelde, K. (2006). Dairy farm CH4 and N2O emissions, from one square metre to the

full farm scale. Agriculture, ecosystems & environment, 112(2-3), 146-152.

Hensen, A., Velzeboer, I., Frumau, K. F. A., van den Bulk, W. C. M., & Dinther, D. V. (2019). Methane emission measurements of offshore oil and gas platforms.

Hersbach, H., Bell, B., Berrisford, P., Hirahara, S., Horányi, A., Muñoz-Sabater, J., ... & Simmons, A. (2020). The ERA5 global reanalysis. Quarterly Journal of the Royal Meteorological Society.

Houweling, S., Krol, M., Bergamaschi, P., Frankenberg, C., Dlugokencky, E. J., Morino, I., ... & Gerbig, C. (2014). A multi-year methane inversion using SCIAMACHY, accounting for systematic errors using TCCON measurements. Atmospheric chemistry and physics, 14(8), 3991-4012.

Hundsdorfer, W., Koren, B., & Verwer, J. G. (1995). A positive finite-difference advection scheme. Journal of computational physics, 117(1), 35-46.

IPCC, 2022: Climate Change 2022: Impacts, Adaptation, and Vulnerability. Contribution of Working Group II to the Sixth Assessment Report of the Intergovernmental Panel on Climate Change [H.-O. Pörtner, D.C. Roberts, M. Tignor, E.S. Poloczanska, K. Mintenbeck, A. Alegría, M. Craig, S. Langsdorf, S. Löschke, V. Möller, A. Okem, B. Rama (eds.)]. Cambridge University Press. In Press.

Irakulis-Loitxate, I., Guanter, L., Liu, Y. N., Varon, D. J., Maasakkers, J. D., Zhang, Y., ... & Jacob, D. J. (2021). Satellite-based survey of extreme methane emissions in the Permian basin. Science Advances, 7(27), eabf4507.

Jacob, D. J., Turner, A. J., Maasakkers, J. D., Sheng, J., Sun, K., Liu, X., ...& Frankenberg, C. (2016). Satellite observations of atmospheric methane and their value for quantifying methane emissions. Atmospheric Chemistry and Physics.

Kadivar, M., Tormey, D., & McGranaghan, G. (2021). A review on turbulent flow over rough surfaces: Fundamentals and theories. International Journal of Thermofluids, 10, 100077.

Kastner-Klein, P., & Rotach, M. W. (2004). Mean flow and turbulence characteristics in an urban roughness sublayer. Boundary-Layer Meteorology, 111(1), 55-84.

Kemenov, K., Wang, H., Pope, S. B. (2012). Turbulence resolution scale dependence in large-eddy simulations of a jet flame. Flow Turbul COmbust 88:529-561.

Korsakissok, I., & Mallet, V. (2009). Comparative study of Gaussian dispersion formulas within the Polyphemus platform: evaluation with Prairie Grass and Kincaid experiments. Journal of applied meteorology and climatology, 48(12), 2459-2473.

Krug, D., Philip, J., & Marusic, I. (2017). Revisiting the law of the wake in wall turbulence. Journal of Fluid Mechanics, 811, 421-435.

Łakomiec, P., Holst, J., Friborg, T., Crill, P., Rakos, N., Kljun, N., ... & Rinne, J. (2021). Field-scale CH 4 emission at a subarctic mire with heterogeneous permafrost thaw status. Biogeosciences, 18(20), 5811-5830.

Lan, X., Talbot, R., Laine, P., & Torres, A. (2015). Characterizing fugitive methane emissions in the Barnett Shale area using a mobile laboratory. Environmental science & technology, 49(13), 8139-8146.

Li, X. X., Britter, R., & Norford, L. K. (2016). Effect of stable stratification on dispersion within urban street canyons: A large-eddy simulation. Atmospheric environment, 144, 47-59.

Lilly, D. K. (1968). Models of cloud-topped mixed layers under a strong inversion. Quarterly Journal of the Royal Meteorological Society, 94(401), 292-309.

Maazallahi, H., Fernandez, J. M., Menoud, M., Zavala-Araiza, D., Weller, Z. D., Schwietzke, S., ... & Röckmann, T. (2020). Methane mapping, emission quantification, and attribution in two European cities: Utrecht (NL) and Hamburg (DE). Atmospheric Chemistry and Physics, 20(23), 14717-14740.

Maazallahi, H., Delre, A., Scheutz, C., Fredenslund, A. M., Schwietzke, S., Denier van der Gon, H., & Röckmann, T. (2022). Intercomparison of detection and quantification methods for methane emissions from the natural gas distribution network in Hamburg, Germany. Atmospheric Measurement Techniques Discussions, 1-29.

Maazallahi, H. (2022). Detection, attribution and quantification of methane emissions using mobile measurement techniques in European cities (Doctoral dissertation, Utrecht University).

Macdonald, R. W., Griffiths, R. F., & Cheah, S. C. (1997). Field experiments of dispersion through regular arrays of cubic structures. Atmospheric Environment, 31(6), 783-795.

Macdonald, R. W. (2000). Modelling the mean velocity profile in the urban canopy layer. Boundary-Layer Meteorology, 97(1), 25-45.

Marro, M., Nironi, C., Salizzoni, P., & Soulhac, L. (2015). Dispersion of a passive scalar fluctuating plume in a turbulent boundary layer. part II: Analytical modelling. Boundary-Layer Meteorology, 156(3), 447-469.

Martinuzzi, R., & Tropea, C. (1993). The flow around surface-mounted, prismatic obstacles placed in a fully developed channel flow (data bank contribution).

Matheou, G., & Bowman, K. W. (2016). A recycling method for the large-eddy simulation of plumes in the atmospheric boundary layer. Environmental Fluid Mechanics, 16(1), 69-85.

Mavroidis, I., & Griffiths, R. F. (2001). Local characteristics of atmospheric dispersion within building arrays. Atmospheric Environment, 35(16), 2941-2954.

Mellado, J. P., Bretherton, C. S., Stevens, B., & Wyant, M. C. (2018). DNS and LES for simulating stratocumulus: Better together. Journal of Advances in Modeling Earth Systems, 10(7), 1421-1438.

Michioka, T., Takimoto, H., Ono, H., & Sato, A. (2019). Large-eddy simulation of the effects of wind-direction fluctuations on turbulent flow and gas dispersion within a cubical canopy. Boundary-Layer Meteorology, 173(2), 243-262.

Mitchell, A. L., Tkacik, D. S., Roscioli, J. R., Herndon, S. C., Yacovitch, T. I., Martinez, D. M., ... & Omara, M. (2015). Measurements of methane emissions from natural gas gathering facilities and processing plants: Measurement results. Environmental science & technology, 49(5), 3219-3227.

Mønster, J., Samuelsson, J., Kjeldsen, P., & Scheutz, C. (2015). Quantification of methane emissions from 15 Danish landfills using the mobile tracer dispersion method. Waste Management, 35, 177-186.

Montzka, S. A., Dlugokencky, E. J., & Butler, J. H. (2011). Non-CO2 greenhouse gases and climate change. Nature, 476(7358), 43-50.

Moser, R.D., Kim, J. and Mansour, N.N. (1999). Direct numerical simulation of turbulent channel flow up to Re(τ)=590. Physics of fluids, Vol.11, No.4, 943-945.

Nardecchia, F., Gugliermetti, F., & Bisegna, F. (2016). How temperature affects the airflow around a single-block isolated building. Energy and Buildings, 118, 142-151.

Nastrom, G. D., Fritts, D. C., and Gage, K. S. (1987). An investigation of terrain effects on the mesoscale spectrum of atmospheric motions, J. Atmos. Sci., 44, 3087–3096.

Ng, E., Yuan, C., Chen, L., Ren, C., & Fung, J. C. (2011). Improving the wind environment in high-density cities by understanding urban morphology and surface roughness: A study in Hong Kong. Landscape and Urban planning, 101(1), 59-74.

Nieuwstadt, F. T. M. (1992). A large-eddy simulation of a line source in a convective atmospheric boundary layer—I. Dispersion characteristics. Atmospheric Environment. Part A. General Topics, 26(3), 485-495.

Nironi C, Salizzoni P, Marro M, Mejean P, Grosjean N, Soulhac L (2015). Dispersion of a passive scalar fluctuating plume in a turbulent boundary layer. Part I: velocity and concentration measurements. Boundary-Layer Meteorol 156(3):415–446

Oskouie, S. N., Yang, Z., Wang, B. C., & Yee, E. (2015, September). Plume dispersion characteristics in the turbulent convective regime. In THMT-15. Proceedings of the Eighth International Symposium On Turbulence Heat and Mass Transfer. Begel House Inc..

Oskouie, S. N., Wang, B. C., & Yee, E. (2017). Numerical study of dual-plume interference in a turbulent boundary layer. Boundary-Layer Meteorology, 164(3), 419-447.

Oskouie, S. N., Yang, Z., & Wang, B. C. (2018). Study of passive plume mixing due to two line source emission in isotropic turbulence. Physics of Fluids, 30(7), 075105.

Ouellette, N. T., Xu, H., Bourgoin, M., & Bodenschatz, E. (2006). An experimental

study of turbulent relative dispersion models. New Journal of Physics, 8(6), 109.

Phillips, N. G., Ackley, R., Crosson, E. R., Down, A., Hutyra, L. R., Brondfield, M., ... & Jackson, R. B. (2013). Mapping urban pipeline leaks: Methane leaks across Boston. Environmental pollution, 173, 1-4.

Philips, D. A., Rossi, R., & Iaccarino, G. (2013). Large-eddy simulation of passive scalar dispersion in an urban-like canopy. Journal of Fluid Mechanics, 723, 404-428.

Piomelli, U., & Balaras, E. (2002). Wall-layer models for large-eddy simulations. Annual review of fluid mechanics, 34(1), 349-374.

Plant, G., Kort, E. A., Murray, L. T., Maasakkers, J. D., & Aben, I. (2022). Evaluating urban methane emissions from space using TROPOMI methane and carbon monoxide observations. Remote Sensing of Environment, 268, 112756.

Pope, S. B. (2000). Turbulent flows. Cambridge University Press. Cambridge.

Pope, S. B. (2004). Ten questions concerning the large-eddy simulations of turbulent flows. New J Phys 6:35.

Ražnjević, A., van Heerwaarden, C., & Krol, M. (2022). Evaluation of two common source estimation measurement strategies using large-eddy simulation of plume dispersion under neutral atmospheric conditions, Atmos. Meas. Tech., 15, 3611–3628, https://doi.org/10.5194/amt-15-3611-2022

Ražnjević, van Heerwaarden, C., van Stratum, B., Hensen, A., Velzeboer, I., van den Bulk, P., & Krol, M.: Interpretation of field observations of point-source methane plume using observation driven large-eddy simulations, Atmospheric Chemistry and Physics, 22(10), 6489-6505, https://doi.org/10.5194/acp-22-6489-2022, 2022.

Robertson, A. M., Edie, R., Snare, D., Soltis, J., Field, R. A., Burkhart, M. D., ... & Murphy, S. M. (2017). Variation in methane emission rates from well pads in four oil and gas basins with contrasting production volumes and compositions. Environmental science & technology, 51(15), 8832-8840.

Röckmann, T., Eyer, S., Veen, C. V. D., Popa, M. E., Tuzson, B., Monteil, G., ... & Zazzeri, G. (2016). In situ observations of the isotopic composition of methane

at the Cabauw tall tower site. Atmospheric chemistry and physics, 16(16), 10469-10487.

Rotach, M. W. (2001). Simulation of urban-scale dispersion using a Lagrangian stochastic dispersion model. Boundary-Layer Meteorology, 99(3), 379-410.

Ruckstuhl, A. F., Henne, S., Reimann, S., Steinbacher, M., Vollmer, M. K., O'Doherty, S., ... & Hueglin, C. (2012). Robust extraction of baseline signal of atmospheric trace species using local regression. Atmospheric Measurement Techniques, 5(11), 2613-2624.

Rybchuk, A., Alden, C. B., Lundquist, J. K., & Rieker, G. B. (2020). A Statistical Evaluation of WRF-LES Trace Gas Dispersion Using Project Prairie Grass Measurements.

Saunois, M., Bousquet, P., Poulter, B., Peregon, A., Ciais, P., Canadell, J. G., ... & Janssens-Maenhout, G. (2016). The global methane budget 2000-2012. Earth System Science Data, 8(2), 697-751.

Saunois, M., Stavert, A. R., Poulter, B., Bousquet, P., Canadell, J. G., Jackson, R. B., ... & Zhuang, Q. (2020). The global methane budget 2000–2017. Earth system science data, 12(3), 1561-1623.

Schalkwijk, J., Jonker, H. J., Siebesma, A. P., and Bosveld, F. C.: A year-long large-eddy simulation of the weather over Cabauw: An overview, Mon. Weather Rev., 143, 828–844, 2015.

Seinfeld, J. H., (1986). Atmospheric Chemistry and Physics of Air Pollution. John Wiley and Sons, New York, 738 pp.

Shah, A., Pitt, J. R., Ricketts, H., Leen, J. B., Williams, P. I., Kabbabe, K., ... & Allen, G. (2019). Testing the near-field Gaussian plume inversion flux quantification technique using unmanned aerial vehicle sampling. Atmos. Meas. Tech. Discuss.

Schultz, M. P., & Flack, K. A. (2013). Reynolds-number scaling of turbulent channel flow. Physics of Fluids, 25(2), 025104.

Snyder, W. H., & Castro, I. P. (2002). The critical Reynolds number for rough-wall boundary layers. Journal of Wind Engineering and Industrial Aerodynamics, 90(1), 41-54.

Steinfeld, G., S. Raasch, and T. Markkanen, 2008: Footprints in Homogeneously and Heterogeneously Driven Boundary Layers Derived from a Lagrangian Stochastic Particle Model Embedded into Large-Eddy Simulation. Boundary-Layer Meteorol, 129 (2), 225–248.

Tseng, Y. H., & Ferziger, J. H. (2003). A ghost-cell immersed boundary method for flow in complex geometry. Journal of computational physics, 192(2), 593-623.

Van Heerwaarden, C., van Stratum, B. J. H., Heus, T., Gibbs, J.A., Fedorovich E., Mellado, J.P. (2017). MicroHH 1.0: A computational fluid dynamics code for direct numerical simulation and large-eddy simulation of atmospheric boundary layer flows. Geosci. Model Dev., 10(8), 3145-3165.

Villa, J. A., Smith, G. J., Ju, Y., Renteria, L., Angle, J. C., Arntzen, E., ... & Bohrer, G. (2020). Methane and nitrous oxide porewater concentrations and surface fluxes of a regulated river. Science of The Total Environment, 715, 136920.

Vinković, K., Andersen, T., de Vries, M., Kers, B., van Heuven, S., Peters, W., ... & Chen, H. (2022). Evaluating the use of an Unmanned Aerial Vehicle (UAV)-based active AirCore system to quantify methane emissions from dairy cows. Science of the Total Environment, 831, 154898.

Vrieling, A. J., & Nieuwstadt, F. T. M. (2003). Turbulent dispersion from nearby point sources—interference of the concentration statistics. Atmospheric Environment, 37(32), 4493-4506.

Weller, Z. D., Yang, D. K., & von Fischer, J. C. (2019). An open source algorithm to detect natural gas leaks from mobile methane survey data. PLoS One, 14(2), e0212287.

Weil, Jeffrey C., et al. (2002). Experiments on buoyant plume dispersion in a laboratory convection tank. Boundary-layer meteorology 102.3, 367-414.

Willis, G. E. and Deardorff, J. W. (1978). A laboratory study of dispersion from an elevated source within a modelled convective planetary boundary layer. Atmos. Environ., 12, 1305-1311.

Wunch, D., Jones, D., Toon, G. C., Deutscher, N. M., Hase, F., Notholt, J., ... & Fisher, J. A. (2019). Emissions of methane in Europe inferred by total column measurements.

Atmospheric Chemistry and Physics, 19(6), 3963-3980.

Wyngaard, J. C. (2010). Turbulence in the Atmosphere. Cambridge University Press.

Xiao, S., Peng, C., & Yang, D.: Large-eddy simulation of bubble plume in stratified crossflow. Physical Review Fluids, 6(4), 044613, https://doi.org/10.1103/PhysRevFluids.6.044613, 2021.

Xie, Z., Hayden, P., Voke, P. R., & Robins, A. G. (2004). Large-eddy simulation of dispersion: comparison between elevated and ground-level sources. Journal of Turbulence, 5(1), 031.

Xie Z., Hayden P., Robins A. G., & Voke P. R. (2007). Modelling extreme concentration from a source in a turbulent flow over rough wall. Atmos Environ 41(16):3395–3406.

Xie, Z., & Castro, I. P. (2006). LES and RANS for turbulent flow over arrays of wall-mounted obstacles. Flow, Turbulence and Combustion, 76(3), 291-312.

Yacovitch, T. I., Herndon, S. C., Pétron, G., Kofler, J., Lyon, D., Zahniser, M. S., & Kolb, C. E. (2015). Mobile laboratory observations of methane emissions in the Barnett Shale region. Environmental science & technology, 49(13), 7889-7895.

Zickfeld, K., Solomon, S., & Gilford, D. M. (2017). Centuries of thermal sea-level rise due to anthropogenic emissions of short-lived greenhouse gases. Proceedings of the National Academy of Sciences, 114(4), 657-662.

Acknowledgements

After a PhD project is done, what is left to show in the end is a book. What the book is not showing, however, are the small, everyday experiences a student has on their journey of creating said book. Of course, there is the science, that is why we all decide to do a PhD. There can be stress and angst and occasional bursts of happiness and everything in between that makes it difficult to differentiate between an average PhD student and a moody teenager (at least, this is how I see myself still). But what makes the journey really memorable are the people you meet along the way. Some of them you see every day, they become a part of your life for a while, you end up having more meals with them than with your own family. Some of them you meet very briefly but they leave a lasting impression. My PhD journey too is the sum of people I met who have helped me grow as a researcher, a person or a friend, one way or another. Therefore, I would like to use these pages to thank all the people who have made my years as a student a wonderful experience that it was.

First and foremost, Chiel, thank you for everything! You have been the best first Boss a freaked out Croatian student could ask for. I would like to thank you for all the help, not only with my project, but for making sure the two pandemic years were as painless as possible (I will be eternally grateful for the PhD sweatshop in the attic). Thank you for teaching me how to think for myself, for the guidance, for the discussions, but especially for all the cow fart jokes. And for the friendship. I suppose we could have been even better friends if only you would just admit that Bowie is a better artist than Prince.

Maarten, firstly, without you and without MEMO^2 project I would never come to the Netherlands in the first place. It might sound a tad bit dramatic, but it really was a life altering chance you gave me (well, Chiel too), so thank you. Secondly, our conversations were always very eye opening. Be it about plume models, cool simulations, music, (dry) joking about life. Be it giving me a much needed kick in the butt to focus on my project properly. I learned a lot from you, thank you for that. And lastly, yours is the best coffee in Lumen/Gaia if not in all of WUR, bar none.

As I already mentioned, the MEMO^2 project is why I came to the Netherlands. Our project meetings were always an opportunity to spend time with people who were all working towards the same goal. Every project meeting was a great experience filled with good food, exploration of a different city every time and laughter. For laughter especially I credit my fellow PhD students. Julie, Sara, Semra, Barbara, Badru, Jonas, Piotr, Hossein, Katarina, Mila, Malika, Randulph, Patrik thank you for making every project meeting great! Everyone I met through MEMO^2 was interesting and fun and wise in their own way, thank you everyone for interesting science, interesting talks and schools and all the bits of wisdom and jokes that were dispersed inbetween. I would like to thank Sylvia for being a fantastic project manager we all will remember. Special thanks also to Randulph and Dominic for hosting me at EMPA for a month. It was really great being a part of your group for a while. Also kudos to Randulph for really embracing the Dutch experience in the month he spent at MAQ and biked to work everyday in -14° degree weather (the temperature might be slightly exaggerated but the feat was still very impressive).

The most lasting impression, of course, leave the people you spend every day with. These are the people who you first complain to when your code isn't working (before you go begging a supervisor for help), who you share anecdotes from life with, have an occasional beer with, comment on current world news, have deep discussions about music or just see in hallways on regular basis. In short, your group. And I was incredibly lucky for MAQ to be mine. Since I have been an MAQ student slightly longer than expected, I was fortunate to have very many office mates. Alba's no-nonsense attitude and kindness, Imme's wild energy and positivity, Xabi's chillness, Stijn's humor and affinity for books, Gerbrand's smartness behind his computer, were my first impressions of the group. Thank you all for being so great! A big thank you to the current occupants of the big PhD office (I apologize if there are new ones I haven't met yet and therefore miss): Menno for all those sailor stories you shared, Wouter for being a friend and an infinite pool of knowledge on storms, Martin for always being kind and attentive, Mirjam for pleasant back-from-lunch talks, Robin for teaching me (unknowingly) all the machine learning lingo, Farhan for very nice snacks you always share, Auke for wanting to share all your cool art books and knowledge with me, Raquel for always having a big smile on! Wei, my friend, you were at MAQ for only a year but I will remember you for the rest of my life. Thank you for teaching me the value of rice!
Not to forget the other PhD office, Auke, Aris, Sjoerd, Mary Rose, Kim, Chris, Sytse, Felipe and Ruben my dispersion co-sufferer, thank you all for amazingly deep coffee conversations, jokes, ice cream breaks, beers, quick catch-ups, and good parties!
The rest of the staff has left just as deep impressions on me as the students did. Jordi, the care you have for your students and staff is truly astounding. The way you go out of your way to help in any way you can despite all the busyness is something to strive for.

Thank you, Jordi! Also, your ability to recognize a good sense of humor is commendable. Antonija, hvala na svemu, zbilja. Od prvog dana smo stvorile hrvatski blok, što je mislim potrebno u svim grupama. Hvala na kavama, šetnjama, što ste me primili u svoj dom kad nije bilo moguće otići mome, što si prihvatila sjediti na podiju samnom! Ingrid, thank you for always being so kind and supportive and positive, Mahrooz as well, I will forever be freaked out by microplastics. Barbara, thank you for becoming the greatest friend a person can have. Your cats are awesome! Than you Sandra for always helping, Caroline as well! Many thanks Folkert for always making me jealous of your band t-shirts, and Oscar for showing me some very cool bands I never heard of before. Thank you Laurens for the jazzy Sundays on the Zaaier terrace, you guys were great at jamming! Thank you Gert-Jan, Bert H., Reinder, Michiel, Arnold, Julie, Bart, Linda, Wouter, Chris W. for making MAQ such a great place!

While my work has been quite a big part of my life these past years, I have also met some amazing people that made my life in Wageningen so much better. Thank you Anika for adopting me on the Zaaier terrace on a sunny Sunday afternoon and become and continue to be a fantastic friend. I will forever be your Grasshopper. Maria, thank you for the friendship, talks, hanging outs, support, stumblings home from Zaaier, all the talks about literature and music and world problems. Thank you both, I will never have enough paper to write down how much it all meant. Diederik, you are awesome, and your music taste is impeccable. Thank you Juli too for all the talks about the human condition. To the rest of the people: thank you all for welcoming me into your friend group and making me feel like I knew you for much longer than I actually did.

Mama, tata, hvala na svemu. Ne samo na potpori u zadnjih šest godina nego na svim vožnjama u i iz Zagreba, na financiranju kroz studiranje, na razgovorima, na tome što sam uvijek znala da će na kraju sve biti u redu. Teško je reći u samo par riječi koliko ste zaslužni što sam ja ja. Sergej, od nas dvoje ti si uvijek smirenije i opuštenije dijete i nadam se da ću i ja postići tu razinu jednog dana. Hvala ti što si najbolji brat i najbolji paranymph na svijetu. Ujače, mislim da znam što je to ljubav! Ivana, Ivane, Ivana, Ivane, Ingrid, Andrea, bako, baba, Elisabet, Zdrava, Snježo, Ćiro, Ljiljo hvala vam svima za sve male ili malo veće interakcije kroz godine, za smijeh i kave i prigovaranja i savjete i ručkove i ljubav!
Cimi i Daniele, uvijek me zadivljuje da i nakon šest godina mog odsudstva iz Zagreba se ništa nije pretjerano promijenilo u našem prijateljstvu. Hvala što živite samnom online sve ove godine kroz sve uspone i padove. Andjela, Mare, od smokve tj. od petog razreda, pa do sad. Usprkos udaljenosti i životu i svemu što se desilo ili će se desiti, znam da ste uvijek tu i bit će te (i obrnuto naravno) sve dok čangrizave ne završimo u plićaku u Karinu. Za mnogo, mnogo godina nadam se!

Netherlands Research School for the
Socio-Economic and Natural Sciences of the Environment

D I P L O M A

for specialised PhD training

The Netherlands research school for the
Socio-Economic and Natural Sciences of the Environment
(SENSE) declares that

Anja Ražnjević

born on 16 July 1990 in Benkovac, Croatia

has successfully fulfilled all requirements of the
educational PhD programme of SENSE.

Wageningen, 1st of September 2023

Chair of the SENSE board

Prof. dr. Martin Wassen

The SENSE Director

Prof. Philipp Pattberg

The SENSE Research School has been accredited by the Royal Netherlands Academy of Arts and Sciences (KNAW)

KONINKLIJKE NEDERLANDSE
AKADEMIE VAN WETENSCHAPPEN

The SENSE Research School declares that **Anja Ražnjević** has successfully fulfilled all requirements of the educational PhD programme of SENSE with a work load of 36.4 EC, including the following activities:

SENSE PhD Courses

- Environmental research in context (2018)
- Research in context activity: 'Organising a workshop on Gaussian plume modelling in Heidelberg' (2019)

Other PhD and Advanced MSc Courses

- MEMO2 1st winter school, MEMO2 project Netherlands (2018)
- MEMO2 2nd winter school, MEMO2 project France (2019)
- Career Orientation, Wageningen Graduate Schools (2019)
- MEMO2 Gaussian plume workshop, Heidelberg University (2018)
- The Essentials of Scientific Writing & Presenting, Wageningen Graduate Schools (2020)
- Intensive writing week, Wageningen Graduate Schools (2021)

Management and Didactic Skills Training

- Teaching assistant in the BSc course 'Introduction Atmosphere' (2019-2021)

Oral Presentations

- *Using Direct Numerical Simulation to evaluate plume measurement strategies*. Buys Ballot Autumn Symposium, 23-25 October 2019, 's-Hertogenbosch, The Netherlands
- *Comparison of large eddy simulation of a point source methane plume in a slightly convective atmosphere with measurements from MEMO 2 campaign*. Integrated Carbon Observation System, 15 – 17 September 2020, Utrecht, the Netherlands

SENSE coordinator PhD education

Dr. ir. Peter Vermeulen

This research has been supported by the European Union's Horizon 2020 research and innovation program under the Marie Skłodowska-Curie grant agreement no. 722479. Maarten Krol received funding from the European Research Council (ERC) under the European Union's H2020 research and innovation program under grant agreement no. 742798.

Cover design by Ena Jurov